Time-resolved quantum nanoelectronics in electromagnetic environments

Benoît Rossignol

Université Grenoble Alpes

THÈSE

Pour obtenir le grade de

DOCTEUR DE L'UNIVERSITE GRENOBLE ALPES
Spécialité : **Physique théorique**

Arrêté ministériel : 25 mai 2016

Présentée par

Benoît Rossignol

Thèse dirigée par **Xavier Waintal**,
et codirigée par **Christoph Groth**

préparée au sein du **IRIG/PHELIQS/GT**
dans **l'École Doctorale de Physique**

Time-resolved quantum nanoelectronics in electromagnetic environments

Thèse soutenue publiquement le **13 janvier 2020**,
devant le jury composé de :

M. Christopher BAUERLE
Directeur de recherche CNRS, Institut Néel, Président
M. Pascal SIMON
Professeur, Université Paris Sud, Rapporteur
M. Christoph MORA
Professeur, Université Paris Diderot, Rapporteur
M. Philippe JOYEZ
Ingénieur-Chercheur, CEA Saclay, Examinateur
M. Dietmar Weinmann
Directeur de recherche CNRS, IPCMS, Examinateur
M. Xavier WAINTAL
Ingénieur-Chercheur, CEA Grenoble, Directeur de thèse
M. Christoph GROTH
Ingénieur-Chercheur, CEA Grenoble, Co-directeur de thèse

Abstract

Quantum nanoelectronics is in a phase of great expansion, supported mainly by the development of quantum computing. Quantum properties only appear in a perfectly controlled environment, however, the experiments are also more complex than ever. Numerical tools seem necessary to achieve the required understanding while dealing with such complexity. The time scales involved are getting shorter and are getting closer to the intrinsic quantum time scales of the device. Our group's previous work has simulated time-dependent electron transport on a quantum scale. This thesis aims at improving previous algorithms to obtain greater accuracy and a better description of systems by including electronic environments. This work is divided into three main areas. Firstly, we are improving numerical simulation tools as a function of time in order to take into account an electronic environment in a self-consistent way. Particular emphasis was placed on improving the accuracy and speed of the previous algorithm in order to increase the range of the simulable system. In a second part, the new algorithm is used to simulate real systems in order to demonstrate the existence of new physical phenomena. We are studying a Mach-Zehnder electronic interferometer and its ability to manipulate flying qbits. We study Josephson junctions in different environments in order to highlight the role of quasi-particles, the effect of a very short impulse, and to study topological junction characterization techniques. In the last part, various developments are studied to integrate the effects of quantum correlations between the system and its environment.

Acknowledgments

I would like to thank my supervisors, Xavier Waintal and Christoph Groth, for their support over the past three years. I would like to thank Pascal Simon, Christophe Mora, Philippe Joyez, Philippe Joyez, Philippe Joyez, Christopher Bauerle, and Dietmar Weinmann for reviewing this thesis and serving on my defense committee.

I would like to thank Thomas Kloss, who helped me a lot at the beginning of my thesis. He was also a pleasant office companion for the two years he shared my office. I thank Manuel Houzet and Julia Meyer for interesting working discussions. I would also like to thank Pacôme Armagnat, who made me discover Grenoble and the joys of hiking in the mountains. I will remember Vincent Tablo and Pierre Nataf for sharing my humor. And I will have a pleasant memory of all the other students Corentin Bertrand, Stefan Illics, Mathieu Islas, Baptiste Lamic and all the others who have been pleasant during the 3 years we have shared in the lab. Finally, I would like to thank my parents for their financial and moral support over the years.

Contents

Chapter 1

Introduction

In matter, the electric current is produced by the movement of fundamental particles, electrons. Electrons behave according to the laws of quantum mechanics, where they are described by wave packets. The behavior of the wave is disturbed by all the defects of the surrounding matter. The distance at which the electron maintains a wave packet behavior is called *coherence length*. At room temperature, the coherence length is a few nanometers. In this condition, the wave properties cannot be probed. At cryogenic temperatures, below $< 1K$, the coherence length can be increased up to a few micrometers and be accessible to experiments. On the other hand, modern manufacturing technology makes it possible to design electronic circuits with characteristics of a few tenths of a nanometre. It is possible to build experiments where electrons maintain their wave packet behavior throughout a complete electronic circuit. We will call them quantum circuits and the study of this type of circuit is called quantum transport.

The quantum circuits are connected to the macroscopic world by classical electronics. This classic electronics is necessary to probe and manipulate the behavior in the circuits by applying different bias voltages. Recent experiments have made it possible to apply a bias voltage that varies rapidly by comparison to the time scale of the electron's propagation in quantum circuits. This allows us to probe more deeply the characteristics of the quantum circuit, this domain is called time-dependent quantum transport. All connected conventional electronics also change the behavior of quantum circuits. In general, we define by *electronic environment* everything that is not in the quantum circuit but influences it. Another type of environment is given by Coulomb's interaction with the electrons of the surrounding environment. The Coulomb interaction between electrons is part of the quantum picture. Given the high electron density present in matter, the effect of interaction can often be aggregated by a mean-field theory and considered as a classical interaction, falling into the electronic environment.

The objective of this thesis is to develop theoretical and numerical tools to manage time-dependent quantum transport in quantum circuits by taking into account interaction with the environment. Recent numerical tools have already been developed to simulate different types of time-dependent quantum circuits [1; 2], but the environment was absent from these analyses. This work focuses both on improving these methods and adapting them to take account of the environment. The first part of the introduction provides a general introduction to the field of quantum transport. In the second part, we study the emerging field of time-dependent quantum transport. In the last part, we show the importance of taking into account the electronic environment.

1.1 Mesoscopic quantum electronics

In the absence of external constraint, electrons move in the 3 directions of space. It is difficult to design experiments under these conditions. An important step in building quantum transport experiments has been to reduce the dimensionality of the problem by reducing the movement of electrons in one or two directions. An electron behaves like a wave packet, the characteristic length of variation of the wave packet is given by the Fermi wavelength [3]. The problem can be considered constrained in one direction when the length of freedom along that direction is less than the Fermi wavelength. In a metal, the wavelength of Fermi is in the order of a few angstroms, which is tiny and makes constriction very difficult.

An important step was taken in the 1990s with the use of semiconductors instead of metal. An emblematic example is the two-dimensional electronic gas at the interface of a GaAs/AlGaAs heterostructure. The balance between the Fermi level of the two materials leads to the creation of a small electric field at the interface. This electric field opens a conduction channel in the semiconductor but located at the interface. The electrons are forced to move in the 2D plane of the interface, called 2D electron gas (2DEG). Dimensionality can be further reduced by using voltage gates, metal conductors placed near the 2DEG. The potential of the gates are detected by the electron in the 2DEG, if the potential induced by the conductor is stronger than that one created by the small electric field at the interface, the conduction channel disappears near the conductor. A complete quantum circuit can be created by designing the voltage grid on top of a 2DEG. An example of a Mach-Zehnder interferometer on a 2DEG is shown in Fig. 1.1. The electron gas is situated in a plane parallel to the view, it is constrained by the geometry of the gates shown in the photo.

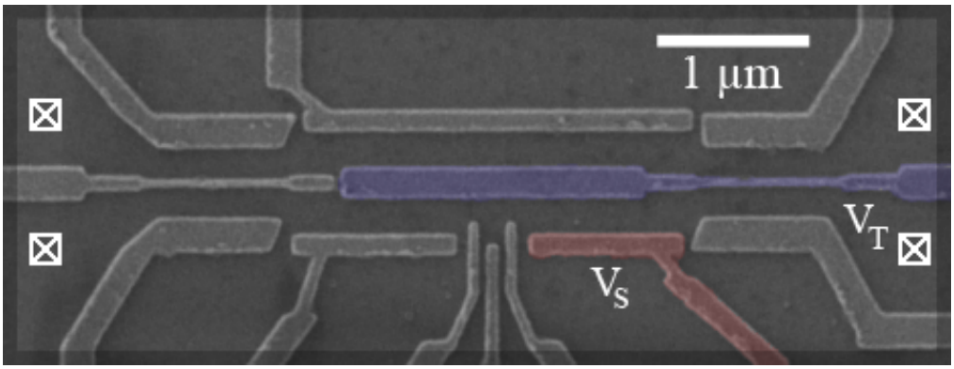

Figure 1.1: Scanning electron microscope image of the Mach-Zehnder interferometer on a 2DEG, the figure is from Ref. [4]. In grey, blue, and red are metal grids used to constrain the 2DEG situated 140 nm below the surfaces. The white squares represent the ohmic contacts connecting the circuit to the macroscopic world.

1.2 Time-dependent experiments

In a 2DEG, electrons at the Fermi level move at a typical speed of 10^4 to 10^5 m/s [5]. For a circuit a few micrometers long, the associated propagation frequency in the circuit is about a few GHz. All voltage variations imposed on the circuit with a frequency greater than the Ghz put the system in a time-dependent state.

The first experiments in the field began with the works of Tien and Gordon [6] in the 1960s. They show that an alternating bias voltage changes the direct current flowing in a circuit, only possible for a circuit in a time-dependent regime. Since then, the field has evolved in many directions, one of the main sources of interest is the construction of a single-electron source. One of the objectives is to reproduce quantum optics experiments with electrons. This field is sometimes called *electronic quantum optics*. The application of a short bias voltage pulse induces a pulse of current propagating in a 2DEG. The pulse carries a total charge. For a very short pulse, this charge can be reduced to correspond to the charge of a single electron e^- [7]. This method is difficult to realize experimentally, but there are other experimental methods to produce single electron sources. In [8], the authors use a quantum dot connected to a conductor via a tunnel barrier in a 2DEG. The electron emission is triggered by the application of a potential step that compensates for the charging energy of the quantum dot. This type of source was used for an electronic experiments of Hanbury-Brown and Twiss [9] or to perform an electronic experiments of Hong-Ou-Mandel [9; 10]. Another method uses surface acoustic waves to generate a confinement potential that

propagates and transports individual electrons from a quantum dot to the rest of the circuit. [11; 12].

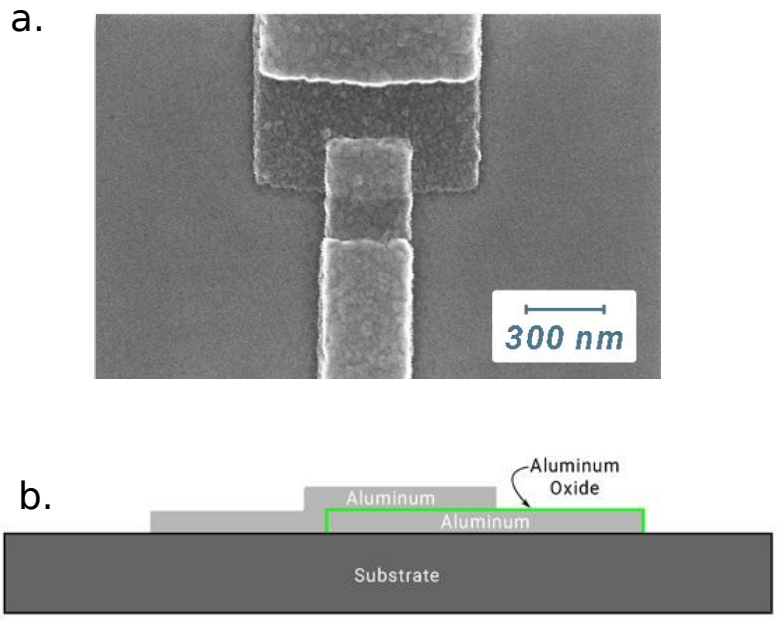

Figure 1.2: In panel (a.) is a scanning electron microscope image of a $Al/Al_2O_x/Al$ Josephson junction from Ref. [13]. In panel (b.) a transverse diagram of the junction. Aluminum is superconducting at $T < 1.2K$ while the oxide remains metallic at this temperature.

In addition to 2DEG, another very important phenomenon of the time-dependent domain is the Josephson ac effect [14]. 2DGEs and Josephson junctions are based on two different physics. Nevertheless, both can be described by the quantum transport theory. A junction consists of two superconductors connected together by a non-superconductive material, Fig. 1.2 shows a standard Aluminum/Oxyde/Aluminum junction. Under the application of a constant bias voltage between the two superconductors, an alternating current with a frequency of $2eV/h$ appears. This oscillation called the ac Josephson effect makes a Josephson junction a highly non-linear electronic component. The most spectacular applications are those that involve inserting a Josephson junction into a conventional electronic circuit to break the linearity of conventional electronics.

1.3 Electronic environments

Many different properties can be obtained by modifying the arrangement of the Josephson junctions in an electronic circuit. By coupling two junctions in parallel, we create a loop called Superconducting Quantum Interference Device (SQUID) [15]. A magnetic flux passing through the loop modifies the phase of the electrons in the circuit, the current in the circuit is very sensitive to this phase. On the one hand, a SQUID will act as a sensitive magnetic detector, up to 10^{-18}T, its small scale of a few μm makes it an appropriate tool to probe the magnetic fluxes generated by another electronic circuit. By imposing the magnetic flux inside the loop, we change the behavior of the SQUID as an electronic component. On the other hand, when the two junctions have different energies, the SQUID acts as a tunable Josephson junction.

The construction of superconducting qubits is another application that has been the subject of many recent developments. A qubit is a two-levels quantum system, building an efficient qubit is the basis of quantum computing [16]. With a classical capacitor and inductance, we can create a harmonic oscillator with infinitly many discrete quantum levels. By replacing one of the components with a non-linear Josephson junction, the harmonic oscillator is distorted and the first two levels can be almost isolated from the other levels, creating a qubit. There are multiple possible architectures for a superconducting qubit, fluxonium [17], xmon [18], quantronium [19]. The most famous type is probably the transmon [20], it has attracted the interest of large private companies [21], and it is at the root of recent breakthroughs in the manipulation of the qubit network [22].

1.4 Summary of the thesis

This thesis focuses on the simulation and understanding of quantum transport at the nanoscale, the study of the properties of electrons at low temperatures $< 1K$ and at small scale $\sim \mu$m. This field has existed for decades, but it continues to grow rapidly. Many analytical developments are possible to understand quantum transport [23]. The theory of quantum mechanics is complex, and to obtain analytical results, many hypotheses are needed to simplify the problem. On the contrary, quantum transport experiments are becoming more and more complex, and numerical tools seem very useful for understanding. Recently, effective simulation tools have been developed as the open software library for the computation of equilibrium quantum transport called Kwant [24]. More recently, our group has also developed algorithms to calculate time-dependent quantum transport [1; 25].

The aim of this thesis is to improve their work both with greater efficiency and with

the inclusion of environmental effects in the simulations for a more realistic description of experiments. The effect of the electronic environments surrounding quantum circuits can be broken down into three main factors. First, there is the Coulomb interaction between conduction electrons, the grids and the surrounding material. This physics is already developed by Pacome Armagnat [26] in the context of equilibrium transport. We use this tool to simulate time-dependent quantum transport. Secondly, there is the classical electronic consisting of resistances, capacitors and classical impedances electrically connected to the quantum circuit. The whole forms a single electrical circuit where the elements are interdependent, as the quantum part cannot be treated separately from the rest of the circuit. Finally, we study the effect of a circuit coupled at the quantum level with its environment, also called decoherence. The objective is to model the stochastic phenomena related to quantum noise as well as those caused by the effect of measurement.

Chapter 3, Simulating time-dependent quantum transport

This chapter begins with the theoretical basis of the simulation of time-dependent quantum transport. It shows how to obtain the formalism of wave functions from Green's famous function formalism. Wave function formalism allows numerical simulations much faster than the standard Non-Equilibrium Green (NEGF) function formalism. This part also completes the demonstration already developed in Ref. [1]. The second part of this chapter is devoted to the numerical tools needed for simulations. Even after the simplification of wave function formalism, a time-based simulation can require hundreds of CPUs for days. In order to simplify calculation costs while maintaining controllable accuracy, many numerical problems must be solved. We give a general description of the solutions used to obtain an efficient parallel simulation algorithm. Finally, we show how to easily include a classical environment in the simulations.

Chapter 4, Spectroscopy of flying qubit

Chapter 4 studies a Mach-Zehnder electronic interferometer and proposes a spectroscopic technique to probe the internal properties of the interferometer. A 2D electronic gas can be confined with grids to create two parallel conduction channels isolated from each other. An electron can be in a state of superposition on both channels. This superposition propagates along with the pair of channels, creating a *flying qubit*. Qubit manipulation is done by lowering the barrier between the channels. This allows electrons to tunnel between the two channels. Such geometry creates a Mach-Zehnder electronic interferometer. The first part of the chapter is devoted to understanding a simple in-

terferometer model subjected to a sinusoidal polarization voltage. We compare three models. One uses the time-dependent simulation technique of chapter 3, another uses a time-based Floquet formalism, and the latter is a result based on analytical calculations. Combining these results, we propose a method to probe the intrinsic property of the Mach-Zehnder by performing dc measurements accessible to current experiments. The shape of the potential seen by electrons is crucial to understanding interferometers. In the second part, we solve the electrostatic problem of the self-consistent Poisson equation to obtain a realistic potential for the quantum circuit. We prove the resilience of our spectroscopy method in the case of a realistic potential at finite temperatures.

Chapter 5, Josephson junctions in electronic circuits

The chapter 5 is devoted to understanding the Josephson junction placed in a conventional electronic circuit.

The first part of the chapter reviews superconductivity and existing methods for simulating superconductivity. We apply these methods to the simulation of an environment-free Josephson junction in the time-dependent regime. We quantitatively recover the analytical predictions of the Josephson AC effect and direct current under a constant bias voltage. In the second part, we insert the Josephson junction into different types of conventional circuits, and we use our new self-consistent algorithm, presented in chapter 3, to perform self-consistent simulations over time. The first application is a junction inside an RC circuit where we retrieve the well-known experimental results. The second application is a junction inside an RLC resonator circuit. We show a qualitative effect resulting from the self-consistent simulation that is not provided by conventional models for such a circuit. Third, we show that an environment-free Josephson junction biased by a short voltage pulse produces an infinite flow of current pulses. We show how the infinite train of pulses degrades in the presence of a dissipative environment. In the last part, we study a model of a topological Josephson junction that presents a Majorana bound state. We study the time-dependent properties of the topological junction. One of the key characteristics of topological junction is the 4π-periodicity of the current-phase relationship. We show how to probe the periodicity with an RLC circuit experimentally, and how the application of a voltage can destroy the 4π-periodicity limiting its observation.

Chapter 6, On the simulation of decoherence

The last chapter examines different methods for integrating decoherence into a time-dependent simulation. This chapter is part of an ongoing effort to treat the decoherence.

We do not claim to solve the problem in this thesis, but we do open up interesting possibilities for future developments. In the first part, we examine the possibility to recover the statistical properties of the shot noise by using the wave function formalism.

In the second part, we study a general decoherence model, the Lindblad equation. The initial model requires exponential computing power, depending on the size of the system. The purpose of this part was to reduce the complexity of the problem to a polynomial problem, accessible to numerical simulation. We demonstrate several possible leads. We develop one possibility into a algorithm. The result is still too slow for an efficient calculation but opens the door to future developments.

Chapter 2

Introduction en français

Dans la matière, le courant électrique est produit par le mouvement de particules fondamentales, les électrons. Les électrons se comportent selon les lois de la mécanique quantique, où ils sont décrits par des paquets d'ondes. Le comportement de l'onde est perturbé par tous les défauts de la matière environnante. La distance à laquelle l'électron maintient un comportement de paquet d'ondes est appelée *longueur de cohérence*. À température ambiante, la longueur de cohérence est de quelques nanomètres. Dans cette condition, les propriétés de l'onde ne peuvent pas être sondés. À des températures cryogéniques, inférieures à $< 1K$, la longueur de cohérence peut être augmentée jusqu'à quelques micromètres et être accessible aux expériences. D'autre part, la technologie de fabrication moderne permet de concevoir des circuits électroniques ayant des caractéristiques de quelques dixièmes de nanomètre. Il est possible de construire des expériences où les électrons maintiennent leur comportement de paquet d'ondes dans tout un circuit électronique. Nous les appellerons des circuits quantiques et l'étude de ce type de circuit est appelée transport quantique.

Les circuits quantiques sont reliés au monde macroscopique par l'électronique classique. Cette électronique classique est nécessaire pour sonder et manipuler le comportement dans les circuits en appliquant différentes tensions de polarisation. Des expériences récentes ont permis d'appliquer une tension de polarisation qui varie rapidement par rapport à l'échelle de temps de la propagation de l'électron dans les circuits quantiques. Cela nous permet de sonder plus profondément les caractéristiques du circuit quantique, ce domaine est appelé transport quantique dépendant du temps. Tous les appareils électroniques conventionnels connectés modifient également le comportement des circuits quantiques. En général, nous définissons par *environnement électronique* tout ce qui n'est pas dans le circuit quantique mais qui l'influence. Un autre type d'environnement est donné par l'interaction de Coulomb avec les électrons du milieu

environnant. L'interaction de Coulomb entre les électrons fait partie de l'image quantique. Étant donné la forte densité d'électrons présente dans la matière, l'effet de l'interaction peut souvent être agrégé par une théorie du champ moyen et considéré comme une interaction classique, tombant dans l'environnement électronique.

L'objectif de cette thèse est de développer des outils théoriques et numériques pour gérer le transport quantique dépendant du temps dans les circuits quantiques en prenant en compte l'interaction avec l'environnement. Des outils numériques récents ont déjà été développés pour simuler différents types de circuits quantiques dépendant du temps [1; 2], mais l'environnement était absent de ces analyses. Ce travail se concentre à la fois sur l'amélioration de ces méthodes et sur leur adaptation pour tenir compte de l'environnement. La première partie de l'introduction fournit une introduction générale au domaine du transport quantique. Dans la deuxième partie, nous étudions le domaine émergent du transport quantique dépendant du temps. Dans la dernière partie, nous montrons l'importance de la prise en compte de l'environnement électronique.

2.1 L'électronique quantique mésocopique

En l'absence de contrainte extérieure, les électrons se déplacent dans les 3 directions de l'espace. Il est difficile de concevoir des expériences dans ces conditions. Une étape importante dans la construction d'expériences de transport quantique a été de réduire la dimensionnalité du problème en réduisant le mouvement des électrons dans une ou deux directions. Un électron se comporte comme un paquet d'ondes, la longueur de variation caractéristique du paquet d'ondes est donnée par la longueur d'onde de Fermi [3]. Le problème peut être considéré comme limité à une direction lorsque la longueur de liberté dans cette direction est inférieure à la longueur d'onde de Fermi. Dans un métal, la longueur d'onde de Fermi est de l'ordre de quelques angströms, ce qui est minuscule et rend la constriction très difficile.

Un pas important a été franchi dans les années 1990 avec l'utilisation de semi-conducteurs à la place du métal. Un exemple emblématique est le gaz électronique bidimensionnel à l'interface d'une hétérostructure GaAs/AlGaAs. L'équilibre entre le niveau de Fermi des deux matériaux conduit à la création d'un petit champ électrique à l'interface. Ce champ électrique ouvre un canal de conduction dans le semi-conducteur mais situé à l'interface. Les électrons sont forcés de se déplacer dans le plan 2D de l'interface, appelé gaz d'électrons 2D (2DEG). La dimensionnalité peut être encore réduite en utilisant des grilles de tension, des conducteurs métalliques placés près du 2DEG. Le potentiel des grilles est détecté par l'électron dans le 2DEG, si le potentiel induit par les grilles est plus fort que celui créé par le petit champ électrique à l'interface, le canal de conduction disparaît près du conducteur. Un circuit quantique complet

peut être créé en concevant la grille de tension au-dessus d'un 2DEG. Un exemple d'interféromètre Mach-Zehnder sur un 2DEG est présenté sur la figure 1.1. Le gaz d'électrons est situé dans un plan parallèle à la vue, il est contraint par la géométrie des grilles montrées sur la photo.

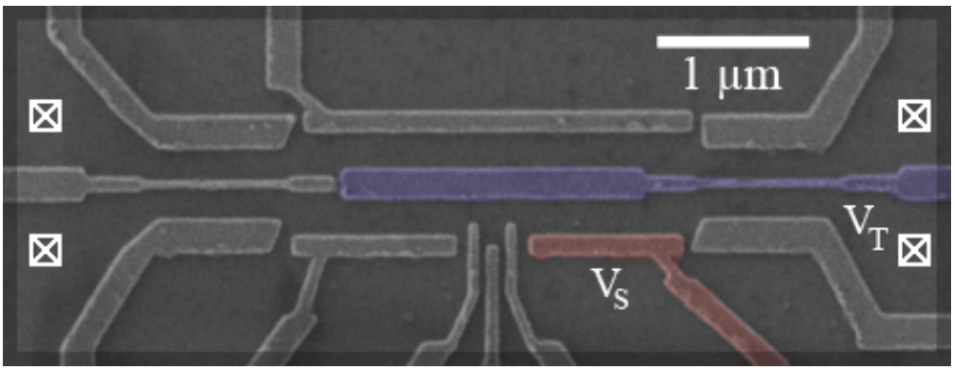

Figure 2.1: Image au microscope électronique à balayage de l'interféromètre Mach-Zehnder sur un 2DEG, la figure est de [4]. En gris, bleu et rouge sont des grilles métalliques utilisées pour contraindre le 2DEG sutué à 140 nm sous les surfaces. Les carrés blancs représentent les contacts ohmiques se connectant au monde macroscopique.

2.2 Les expériences dépendentes du temps

Dans un 2DEG, les électrons au niveau de Fermi se déplacent à une vitesse typique de 10^4 à 10^5 m/s [5]. Pour un circuit de quelques micromètres de long, la fréquence de propagation associée dans le circuit est d'environ quelques GHz. Toutes les variations de tension imposées au circuit avec une fréquence supérieure au Ghz mettent le système dans un état dépendant du temps.

Les premières expériences dans ce domaine ont commencé avec les travaux de Tien et Gordon [6] dans les années 1960. Ils montrent qu'une tension de polarisation alternative modifie le courant continu circulant dans un circuit, ce qui n'est possible que pour un circuit en régime dépendant du temps. Depuis lors, le domaine a évolué dans de nombreuses directions, l'une des principales sources d'intérêt étant la construction d'une source d'électrons unique. L'un des objectifs est de reproduire des expériences d'optique quantique avec des électrons. Ce domaine est parfois appelé *optique quantique électronique*. L'application d'une courte impulsion de tension de polarisation

induit une impulsion de courant se propageant dans un 2DEG. L'impulsion porte une charge totale. Pour une impulsion très courte, cette charge peut être réduite pour correspondre à la charge d'un seul électron e^- [7]. Cette méthode est difficile à réaliser expérimentalement, mais il existe d'autres méthodes expérimentales pour produire des sources d'électrons uniques. Dans [8], les auteurs utilisent un point quantique connecté à un conducteur par une barrière tunnel dans un 2DEG. L'émission d'électrons est déclenchée par l'application d'un saut de potentiel qui compense l'énergie de charge du point quantique. Ce type de source a été utilisé pour des expériences électroniques de Hanbury-Brown et Twiss [9] ou pour réaliser des expériences électroniques de Hong-Ou-Mandel [9; 10]. Une autre méthode utilise les ondes acoustiques de surface pour générer un potentiel confinement qui se propage et qui transporte les électrons individuels d'un point quantique au reste du circuit [11; 12].

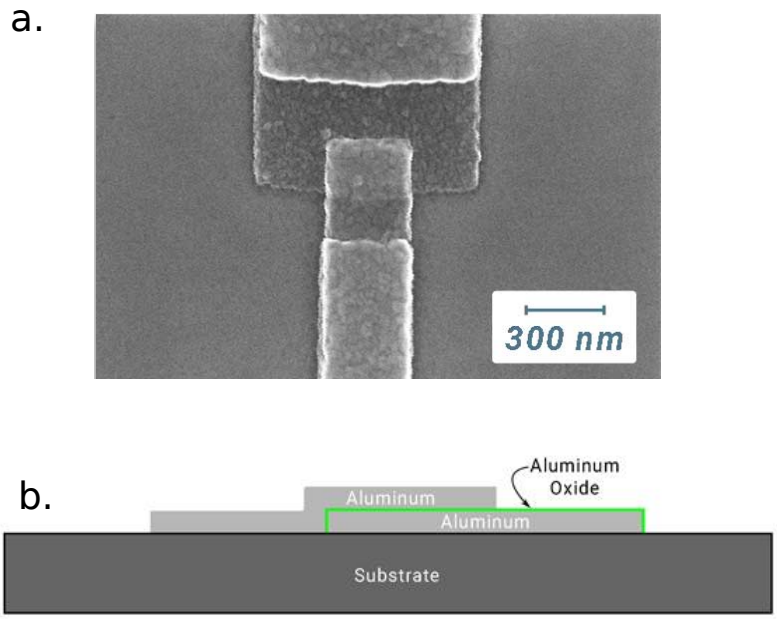

Figure 2.2: Dans le panneau (a.) se trouve une image au microscope électronique à balayage d'une junction Josephson $Al/Al_2O_x/Al$ prise de Ref. [13]. Dans le panneau (b.) un diagramme transversal de la jonction. L'aluminium est supraconducteur à $T < 1.2K$ alors que l'oxyde reste métallique à cette température.

Outre le 2DEG, un autre phénomène très important du domaine temporel est l'effet Josephson ac [14]. Les 2DGE et les jonctions de Josephson sont basées sur deux physiques différentes. Néanmoins, les deux peuvent être décrites par la théorie du

transport quantique. Une jonction est constituée de deux supraconducteurs reliés entre eux par un matériau non supraconducteur. La figure 1.2 montre une jonction standard Aluminium/Oxyde/Aluminium. Sous l'application d'une tension de polarisation constante entre les deux supraconducteurs, un courant alternatif d'une fréquence de $2eV/h$ apparaît. Cette oscillation, appelée effet Josephson alternatif, fait de la jonction Josephson un composant électronique hautement non linéaire. Les applications les plus spectaculaires sont celles qui consistent à insérer une jonction Josephson dans un circuit électronique conventionnel pour rompre la linéarité de l'électronique conventionnelle.

2.3 Les environnements électroniques

De nombreuses propriétés différentes peuvent être obtenues en modifiant la disposition des jonctions Josephson dans un circuit électronique. En couplant deux jonctions en parallèle, on crée une boucle appelée dispositif d'interférence quantique supraconducteur (SQUID) [15]. Un flux magnétique traversant la boucle modifie la phase des électrons dans le circuit, le courant dans le circuit est très sensible à cette phase. D'une part, un SQUID agira comme un détecteur magnétique sensible, jusqu'à 10^{-18}T, sa petite échelle de quelques μm en fait un outil approprié pour sonder les flux magnétiques générés par un autre circuit électronique. En imposant le flux magnétique à l'intérieur de la boucle, nous modifions le comportement du SQUID en tant que composant électronique. D'autre part, lorsque les deux jonctions ont des énergies différentes, le SQUID agit comme une jonction Josephson accordable.

La construction de qubits supraconducteurs est une autre application qui a fait l'objet de nombreux développements récents. Un qubit est un système quantique à deux niveaux, la construction d'un qubit efficace est la base de l'informatique quantique [16]. Avec un condensateur et une inductance classiques, nous pouvons créer un oscillateur harmonique avec une infinité de niveaux quantiques discrets. En remplaçant l'un des composants par une jonction Josephson non linéaire, l'oscillateur harmonique est déformé et les deux premiers niveaux peuvent être presque isolés des autres niveaux, créant ainsi un qubit. Il existe de multiples architectures possibles pour un qubit supraconducteur, fluxonium [17], xmon [18], quantronium [19]. Le type le plus connu est probablement le transmon [20], il a suscité l'intérêt de grandes entreprises privées [21], et il est à l'origine de récentes percées dans la manipulation du réseau de qubit [22].

2.4 Résumé de la thèse

Cette thèse porte sur la simulation et la compréhension du transport quantique à l'échelle nanométrique, l'étude des propriétés des électrons à basse température $< 1K$ et à petite échelle $\sim \mu$m. Ce domaine existe depuis des décennies, mais il continue à se développer rapidement. De nombreux développements analytiques sont possibles pour comprendre le transport quantique [23]. La théorie de la mécanique quantique est complexe, et pour obtenir des résultats analytiques, de nombreuses hypothèses sont nécessaires pour simplifier le problème. Au contraire, les expériences de transport quantique deviennent de plus en plus complexes, et les outils numériques semblent très utiles pour la compréhension. Récemment, des outils de simulation efficaces ont été développés comme la bibliothèque logicielle ouverte pour le calcul du transport quantique à l'équilibre appelée Kwant [24]. Plus récemment, notre groupe a également développé des algorithmes pour calculer le transport quantique en fonction du temps [1; 25].

Le but de cette thèse est d'améliorer leur travail à la fois avec une plus grande efficacité et avec l'inclusion des effets de l'environment dans les simulations pour une description plus réaliste des expériences. L'effet des environnements électroniques entourant les circuits quantiques peut être décomposé en trois facteurs principaux. Premièrement, il y a l'interaction de Coulomb entre les électrons de conduction, les grilles et le matériau environnant. Cette physique est déjà développée par Pacome Armagnat [26] dans le contexte du transport à l'équilibre. Nous utilisons cet outil pour simuler le transport quantique dépendant du temps. Ensuite, il y a l'électronique classique composée de résistance, de condensateur et d'impédance classique connectés électriquement au circuit quantique. L'ensemble forme un circuit électrique unique où les éléments sont interdépendants, car la partie quantique ne peut être traitée séparément du reste du circuit. Enfin, nous étudions l'effet d'un circuit couplé au niveau quantique avec son environnement, également appelé décohérence. L'objectif est de modéliser les phénomènes stochastiques liés au bruit quantique ainsi que ceux causés par l'effet de mesure.

Chapitre 3, Simulation du transport quantique dépendant du temps

Ce chapitre commence par les bases théoriques de la simulation du transport quantique dépendant du temps. Il montre comment obtenir le formalisme des fonctions d'onde à partir du fameux formalisme de fonction de Green. Le formalisme des fonctions d'onde permet des simulations numériques beaucoup plus rapides que le formalisme standard

des fonctions de Green hors-équilibre (NEGF). Cette partie complète également la démonstration déjà développée dans Ref. [1]. La deuxième partie de ce chapitre est consacrée aux outils numériques nécessaires aux simulations. Même après la simplification du formalisme des fonctions d'onde, une simulation basée sur le temps peut nécessiter des centaines de CPU pendant plusieurs jours. Afin de simplifier les coûts de calcul tout en maintenant une précision contrôlable, de nombreux problèmes numériques doivent être résolus. Nous donnons une description générale des solutions utilisées pour obtenir un algorithme de simulation parallèle efficace. Enfin, nous montrons comment inclure facilement un environnement classique dans les simulations.

Chapitre 4, Spectroscopie du qubit volant

Le chapitre 4 étudie un interféromètre électronique Mach-Zehnder et propose une technique spectroscopique pour sonder les propriétés internes de l'interféromètre. Un gaz électronique 2D peut être confiné avec des grilles pour créer deux canaux de conduction parallèles isolés l'un de l'autre. Un électron peut être dans un état de superposition entre les deux canaux. Cette superposition se propage en même temps que la paire de canaux, créant un *qubit volant*. La manipulation du qubit se fait en abaissant la barrière entre les canaux. Cela permet aux électrons de creuser un tunnel entre les deux canaux. Une telle géométrie crée un interféromètre électronique Mach-Zehnder. La première partie du chapitre est consacrée à la compréhension d'un modèle d'interféromètre simple soumis à une tension de polarisation sinusoïdale. Nous comparons trois modèles. L'un utilise la technique de simulation dépendant du temps du chapitre 3, un autre utilise un formalisme de Floquet basé sur le temps, et le dernier est un résultat basé sur des calculs analytiques. En combinant ces résultats, nous proposons une méthode pour sonder la propriété intrinsèque du Mach-Zehnder en effectuant des mesures en courant continu accessibles aux expériences actuelles. La forme du potentiel vu par les électrons est cruciale pour comprendre les interféromètres. Dans la deuxième partie, nous résolvons le problème électrostatique de l'équation de Poisson autoconsistante afin d'obtenir un potentiel réaliste pour le circuit quantique. Nous prouvons la résilience de notre méthode de spectroscopie dans le cas d'un potentiel réaliste à des températures finies.

Chapitre 5, Jonctions Josephson dans des circuits électroniques

Le chapitre 5 est consacré à la compréhension de la jonction Josephson placée dans un circuit électronique classique. La première partie du chapitre passe en revue la supraconductivité et les méthodes existantes de simulation de la supraconductivité. Nous

appliquons ces méthodes à la simulation d'une jonction Josephson sans environnement dans le régime dépendant du temps. Nous récupérons quantitativement les prédictions analytiques de l'effet Josephson AC et du courant continu sous une tension de polarisation constante. Dans la deuxième partie, nous insérons la jonction Josephson dans différents types de circuits classiques et nous utilisons notre nouvel algorithme autoconsistant, présenté au chapitre 3, pour effectuer des simulations autoconsistantes dans le temps. La première application est une jonction à l'intérieur d'un circuit RC où nous récupérons les résultats expérimentaux bien connus. La deuxième application est une jonction à l'intérieur d'un circuit résonateur RLC. Nous montrons un effet qualitatif résultant de la simulation auto-cohérente qui n'est pas fourni par les modèles conventionnels pour un tel circuit. Troisièmement, nous montrons qu'une jonction Josephson sans environnement, polarisée par une courte impulsion de tension, produit un flux infini d'impulsions de courant. Nous montrons comment le train infini d'impulsions se dégrade en présence d'un environnement dissipatif. Dans la dernière partie, nous étudions un modèle de jonction Josephson topologique qui présente un état lié de Majorana. Nous étudions les propriétés de la jonction topologique qui dépendent du temps. L'une des caractéristiques clés de la jonction topologique est la périodicité de la relation entre le courant et la phase. Nous montrons comment sonder expérimentalement la 4π-périodicité avec un circuit RLC, et comment l'application d'une tension peut détruire la périodicité de 4π limitant son observation.

Chapitre 6, De la simulation de la décohérence

Le dernier chapitre examine les différentes méthodes d'intégration de la décohérence dans une simulation en fonction du temps. Ce chapitre s'inscrit dans le cadre d'un effort continu pour traiter la décohérence. Nous ne prétendons pas résoudre le problème dans cette thèse, mais nous ouvrons des possibilités intéressantes pour des développements futurs. Dans la première partie, nous examinons la possibilité de récupérer les propriétés statistiques du bruit de grenaille en utilisant le formalisme de la fonction d'onde.

Dans la deuxième partie, nous étudions un modèle général de décohérence, l'équation de Lindblad. Le modèle initial nécessite une puissance de calcul exponentielle, en fonction de la taille du système. L'objectif de cette partie était de réduire la complexité du problème à un problème polynomial, accessible à la simulation numérique. Nous démontrons plusieurs pistes possibles. Nous développons une possibilité en un algorithme. Le résultat est encore trop lent pour un calcul efficace mais ouvre la porte à des développements futurs.

Chapter 3

Simulating time-dependent quantum transport

3.1 Green's function formalism of time-dependent problem

The objective of this chapter is to simulate quantum nanoelectronics, the motion of the electron in a condensed matter medium. The starting point is a general description of a quantum system in nanoelectronics. We aim to simulate non-interactive problems defined by a quadratic Hamiltonian, in the tight-binding formalism

$$\hat{H} = \sum H_{ij}(t)\hat{c}_i^\dagger \hat{c}_j, \tag{3.1}$$

where $\hat{c}_i^\dagger$ and $\hat{c}_i$ are the creation and annihilation of an electron on the i site. The H_{ij} matrix is a representation of the Hamiltonian in this operator base. The state of a quantum system is described by a vector ψ from Hilbert's space, the Shrödinger" equation gives the equation of the system's motion

$$i\hbar\partial_t\psi = \hat{H}\psi. \tag{3.2}$$

The general objective is to simulate a quantum system that can be inserted into a conventional electrical circuit as a multiterminal component. From the point of view of the conventional circuit, a conductor is entirely defined by its statistical properties: voltage, current, temperature and chemical potential. Within the quantum circuit, there are also quantum properties arising from correlations between electrons. To make the transition between the two, we model lead by a semi-infinite system. One end is attached to the quantum system and the other end is at infinity, towards the classical

system. Any quantum correlation disappears during propagation along the infinite lead and only the statistical properties remain. The central region where all the wires are connected is of finite volume, and can have any shape or dimension: 1D, 2D or 3D.

Because of the semi-infinite leads, the global system is infinite in size. This makes direct numerical simulation impossible. The purpose of this section is to simplify the equations into an equivalent finite size system.

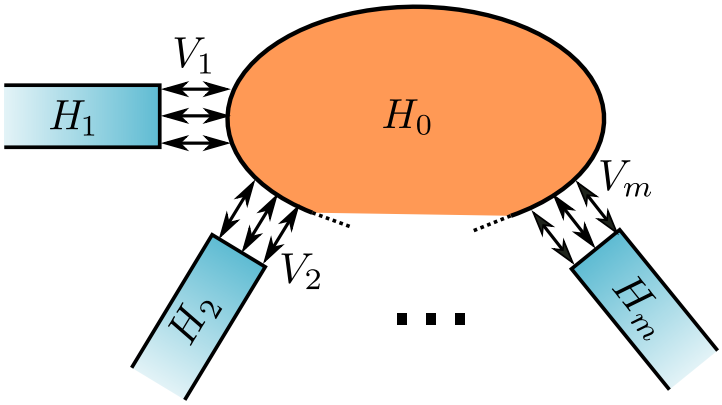

Figure 3.1: System constituted of a scattering region labeled 0 connected to semi-infinite leads $1, \ldots, m$ through couplings elements noted V_i.

3.1.1 Problem modeling

The objective is to reduce the infinite problem to a finite size problem. First, the Hamiltonian in our system is separated in its subsections. There is the dispersion region with a Hamiltonian H_0 and there are semi-infinite leads with Hamiltonians $H_{i\in[1,m]}$. Leads are connected to the diffusion region by coupling elements $V_{i\in[1,m]}$ cf Figure 3.1. The Hamiltonian takes the form of

$$\hat{H} = \begin{pmatrix} H_0 & V_1 & \cdots & V_m \\ V_1^\dagger & H_1 & & 0 \\ \vdots & & \ddots & \\ V_m^\dagger & 0 & & H_m \end{pmatrix}. \tag{3.3}$$

The formalism of Green's function applies to our problem where the strength of the coupling elements $V_{i\in[1,m]}$ between the central region and the lead is treated as the perturbation of the theory. We recall here that this does not limit our problem to

a perturbative regime. The greater, lesser, time-ordered, anti-ordered, advanced and retarded fermionic Green's functions are introduced as usual, using the notation of [27] they read

$$\begin{aligned}
G^{>}(\mathbf{x},t,\mathbf{x}',t') &= -i\left\langle \hat{c}(\mathbf{x},t)\hat{c}^{\dagger}(\mathbf{x}',t')\right\rangle, \\
G^{<}(\mathbf{x},t,\mathbf{x}',t') &= i\left\langle \hat{c}^{\dagger}(\mathbf{x}',t')\hat{c}(\mathbf{x},t)\right\rangle, \\
G^{T}(\mathbf{x},t,\mathbf{x}',t') &= -i\left\langle T(\hat{c}(\mathbf{x},t)\hat{c}^{\dagger}(\mathbf{x}',t'))\right\rangle, \\
G^{\tilde{T}}(\mathbf{x},t,\mathbf{x}',t') &= -i\left\langle \tilde{T}(\hat{c}(\mathbf{x},t)\hat{c}^{\dagger}(\mathbf{x}',t'))\right\rangle, \\
G^{A}(\mathbf{x},t,\mathbf{x}',t') &= -i\theta(t'-t)\left\langle \hat{c}(\mathbf{x},t)\hat{c}^{\dagger}(\mathbf{x}',t')\right\rangle, \\
G^{R}(\mathbf{x},t,\mathbf{x}',t') &= i\theta(t-t')\left\langle \hat{c}(\mathbf{x},t)\hat{c}^{\dagger}(\mathbf{x}',t')\right\rangle,
\end{aligned} \tag{3.4}$$

where $\hat{c}(\mathbf{x},t)$ and $\hat{c}^{\dagger}(\mathbf{x},t)$ are the annihilation and creation operators at position $\mathbf{x}$ at time t. T and $\tilde{T}$ are the time and anti-time ordering operators. The Dyson relationship of [27] is used to link the different types of Green's functions together

$$\begin{pmatrix} G^{T} & G^{<} \\ G^{>} & G^{\tilde{T}} \end{pmatrix} = \begin{pmatrix} g^{T} & g^{<} \\ g^{>} & g^{\tilde{T}} \end{pmatrix} + \begin{pmatrix} g^{T} & g^{<} \\ g^{>} & g^{\tilde{T}} \end{pmatrix} \begin{pmatrix} V & 0 \\ 0 & -V \end{pmatrix} \begin{pmatrix} G^{T} & G^{<} \\ G^{>} & G^{\tilde{T}} \end{pmatrix}. \tag{3.5}$$

where $\hat{g}$ notes the Green's function of the system without V coupling elements. The equation 3.5 contains all the information necessary to solve the problem. The following sections are devoted to simplifying the equation to obtain a form suitable for numerical computation. Green's functions are related to the physical observables thanks to Wick's theorem. The lesser Green's function $G^{<}(t,t')$ is the most suitable to use Wick's theorem, so we concentrate our effort on obtaining it.

The time-ordered Green's functions are expressed as a combination of the other Green's functions $g^{T} = g^{R} + g^{<}$ and $G^{\tilde{T}} = G^{<} - G^{A}$ by manipulating the operators in the equations that define the Green's functions. These relationships are used with the Dyson equation Eq. 3.5 to obtain a closed system of equations for the lower, advanced and retarded Green's functions

$$\begin{aligned}
G^{<} &= g^{<} + g^{R}VG^{<} + g^{<}VG^{A}, \\
G^{R} &= g^{R} + g^{R}VG^{R}, \\
G^{A} &= g^{A} + g^{A}VG^{A}.
\end{aligned} \tag{3.6}$$

3.1.2 Separating regions

G^{A}, G^{R}, and $G^{<}$ contain information about the complete infinite system. Only the values of the G Green's function within the scattering region are interesting in our

calculations. The idea is to separate the equation for the different regions, the central part and the tracks, in order to isolate a closed formula for Green's function from the central part. The following demonstration is based on the work of [28] and [29]. We remember the 0 index tags the central region and indexes $i \geq 1$ tags the leads. G_{ij} notes the Green's function (advanced, delayed or lower) from the region i ($\mathbf{x} \in i$) to the region j ($\mathbf{x'} \in j$). Using this notation, the Green's functions G^A, G^R, and $G^<$ take the following forms

$$G^* = \begin{pmatrix} G^*_{00} & G^*_{01} & \dots & G^*_{0m} \\ G^*_{10} & G^*_{11} & \dots & G^*_{1m} \\ \vdots & \vdots & \ddots & \vdots \\ G^*_{m0} & G^*_{m1} & \dots & G^*_{mm} \end{pmatrix}. \tag{3.7}$$

where G^* is either G^A, G^R, or $G^<$. Green's functions of the system without coupling ($V = 0$) are by definition block diagonal

$$g^* = \begin{pmatrix} g^*_{00} & & & 0 \\ & g^*_{11} & & \\ & & \ddots & \\ 0 & & & g^*_{mm} \end{pmatrix}. \tag{3.8}$$

where g^* is either g^A, g^R, or $g^<$. The coupling in this base is by definition

$$V = \begin{pmatrix} 0 & V_1 & \dots & V_m \\ V_1 & & & \\ \vdots & & 0 & \\ V_m & & & \end{pmatrix}. \tag{3.9}$$

Inserting notations Eq. 3.7, Eq. 3.8, Eq. 3.8 into the Dyson equation Eq. 3.6 gives the relations between the Green's functions of the different regions. For all regions i, j

$$G^<_{ij} = g^<_{ij} + \sum_{kl} g^R_{ik} V_{kl} G^<_{lj} + \sum_{kl} g^<_{ik} V_{kl} G^A_{lj}, \tag{3.10a}$$

$$G^R_{ij} = g^R_{ij} + \sum_{kl} g^R_{ik} V_{kl} G^R_{lj}, \tag{3.10b}$$

$$G^A_{ij} = g^A_{ij} + \sum_{kl} g^A_{ik} V_{kl} G^A_{lj}. \tag{3.10c}$$

Here we did nothing but rewrite Eq. 3.6 using different notations. Now that the indexes of the different regions are explicitly visible, it is easier to separate the regions.

3.1.3 Retarded and advanced Green's functions

The Eq. 3.10b is a closed formula with only retarded Green's functions, it is used to obtain an equation of motion for $\mathcal{G}^R_{00}$. The region 0 is separated from the others

$$\begin{aligned} G^R_{00} &= g^R_{00} + \sum_l g^R_{00} V_l G^R_{l0}, \\ \forall i \geq 1,\ G^R_{i0} &= g^R_{ii} V_i G^R_{00}. \end{aligned} \tag{3.11}$$

The combination of the two equations gives the Dyson equation for the central region only

$$G^R_{00} = g^R_{00} + g^R_{00} \Sigma^R G^R_{00}, \tag{3.12}$$

where the retarded self-energy of the leads without interactions is defined as

$$\Sigma^R = \sum_l V_l g^R_{ll} V_l. \tag{3.13}$$

The self-energy is defined on the system without interaction, it will be treated in the next section. The equation of motion for the retarded Green's function is obtained by applying the derivative $(i\partial_t - H_0)$ to the previous equation

$$(i\hbar\partial_t - H_0(t) - \Sigma^R) G^R_{00} = \delta(t - t'), \tag{3.14}$$

where we used the property of the Green's function $(i\hbar\partial_t - H_0) g^R_{00} = \delta(t - t')$. Equation 3.14 provides a differential equation involving G^R_{00} with a finite spatial extension and Σ^R calculated from the non-interacting system. This equation can be numerically integrated to obtain $G^R_{00}(t, t')$ at any time. With a similar demonstration, the problem for the advanced Green's function is solved by using Eq. 3.10c to obtain

$$G^A_{00} = g^A_{00} + g^A_{00} \Sigma^A G^A_{00}, \tag{3.15}$$

and the differential equation

$$(i\hbar\partial_t - H_0(t) - \Sigma^A) G^A_{00} = \delta(t - t'), \tag{3.16}$$

where $\Sigma^A = \sum_l V_l g^A_{ll} V_l$ is the advanced self-energy.

3.1.4 Lesser Green's functions

Eq. 3.10a is solved to obtain an equation for the lesser Green's function within the scattering region $G^<_{00}$. The demonstration is similar to the one used for the retarded Green's function. The central region is separated from the other region, from Eq. 3.10a

$$G^<_{00} = g^<_{00} + g^R_{00} \sum_{l>0} V_l G^<_{l0} + g^<_{00} \sum_{l>0} V_l G^A_{l0}. \tag{3.17}$$

and $\forall i \geq 1$,

$$G^{<}_{i0} = \sum_{kl} g^{R}_{ik} V_{kl} G^{<}_{l0} + \sum_{kl} g^{<}_{ik} V_{kl} G^{A}_{l0},$$
$$G^{A}_{i0} = \sum_{i} g^{A}_{ii} V_i G^{A}_{00}. \tag{3.18}$$

By replacing Eq. 3.18 in Eq. 3.17 we get

$$G^{<}_{00} = g^{<}_{00} + g^{R}_{00}\Sigma^{R}G^{<}_{00} + g^{R}_{00}\Sigma^{<}G^{A}_{00} + g^{<}_{00}\Sigma^{A}G^{A}_{00}, \tag{3.19}$$

where the lesser self-energy of the leads without interactions is defined by $\Sigma^{<} = V g^{<} V$. The previous equality is rewritten as follows

$$(1 - g^{R}_{00}\Sigma^{R})G^{<}_{00} = g^{R}_{00}\Sigma^{<}G^{A}_{00} + g^{<}_{00}(1 + \Sigma^{A}G^{A}_{00}). \tag{3.20}$$

Finally the equation is multiplied to the left by $(1 + G^{R}_{00}\Sigma^{R})$ and results on the retarded Green's function of the previous part (Eq. 3.12) are used to obtain a simplify form, commonly referred as the Keldysh equation [30],

$$G^{<}_{00} = G^{R}_{00}\Sigma^{<}G^{A}_{00} + (1 + G^{R}_{00}\Sigma^{R})g^{<}_{00}(1 + \Sigma_{A}G^{A}_{00}). \tag{3.21}$$

The left side is $G^{<}_{00}$ the Green's function in the central region, it is the quantity we are trying to explicit. The right side decompose into two terms.

The first term is composed with the self-energy $\Sigma^{<}$ and the Green's function G^{R}_{00} and G^{A}_{00}. The lesser self-energy of the leads is defined by using g^{R}_{00}, the retarded Green's function of the central region in the absence of coupling to the lead, and without coupling the central region is a closed system that can be solved by many methods. The retarded and advanced Green's functions can be obtain by solving the equation of motion Eq. 3.14 and Eq. 3.16. The numerical calculation of $G^{R}_{00}\Sigma^{<}G^{A}_{00}$ is the main subject of the article Ref. [1]. All the methods studied in the article Ref. [1] are based on a tight-binding model and gives the same results. The differences lie in the computational costs in both time and memory. The most effective method is the wave function approach, described in the next section. It has a better scaling than the other non-equilibrium Green's function method, providing the massive acceleration needed to simulate a complex system. Simulations were performed up to $\propto 10^5$ sites and 10^6 times the smallest time scale of the system.

The second term $(1+G^{R}_{00}\Sigma^{R})g^{<}(1+\Sigma_{A}G^{A}_{00})$ corresponds to the contribution of bound states. In the non-interacting case, bound states do not participate in the conduction measured far inside the leads. The term is often neglected for analytical purposes [30], [31]. In numerical simulations, the conduction properties are measured at a finite distance from the scattering region where bound states have not decayed and must be taken into account. For consistency with the first term, the wave function formalism is used to calculate this term.

3.2 The wave function approach

The lesser self-energy is defined by $\Sigma^<(t,t') = V g^<(t,t') V$. Hamiltonians of lead are not time-dependent, and $g^<$ corresponds to the Green's function of lead without coupling to the scattering region. Thus, the lesser self-energy is invariant by translation in time $\Sigma^<(t,t') = \Sigma^<(t-t')$. The Fourier decomposition is used to obtain the decomposition into energies

$$\Sigma^<(t-t') = \sum_l \int \frac{dE}{2\pi} i f_l e^{-\frac{i}{\hbar}E(t-t')} \Gamma_l(E), \tag{3.22}$$

where l labels the leads. The Kernel Γ_l is diagonalized, in the "dual transverse wave function" bases, see Ref. [31],

$$\Gamma_m(E) = \sum_\alpha v_{m\alpha} \xi_{\alpha E} \xi^\dagger_{\alpha E}. \tag{3.23}$$

By inserting this decomposition into the Eq. 3.21 we obtain the lesser Green's function as an integral over the wave functions

$$G^R_{00} \Sigma^< G^A_{00} = \sum_\alpha \int \frac{dE}{2\pi} i f_\alpha(E) \psi_{\alpha E}(t) \psi_{\alpha E}(t')^\dagger, \tag{3.24}$$

with wave functions defined as $\psi_{\alpha E}(t) = \sqrt{v_{\alpha E}} G^R_{00} \xi_{\alpha E}$. The equation of motion for the wave functions is obtained from the equation of motion of the retarded Green's function Eq. 3.14,

$$i\hbar \partial_t \psi_{\alpha E} = \hat{H}(t) \psi_{\alpha E} + \sqrt{v_\alpha} e^{-i\frac{E}{\hbar}t} \xi_{\alpha E}. \tag{3.25}$$

The second term of the equation 3.21 is rewritten be using equation Eq. 3.12 and 3.15 to obtain

$$(1 + G^R_{00}\Sigma^R) g^< (1 + \Sigma_A G^A_{00}) = G^R_{00} \left[(g^R)^{-1} g^< (g^A)^{-1} \right] G^A_{00}. \tag{3.26}$$

The central part of this equation is defined by non-interacting Green's function of the central region only, we can use the Fourier transform. For a central region with a finite size, the kernel of the Fourier transform is diagonalized into bound state labeled by the index γ,

$$(g^R)^{-1} g^< (g^A)^{-1} (t-t') = \int \frac{dE}{2\pi} f_0(E) e^{-\frac{i}{\hbar}E(t-t')} \sum_\gamma \xi_{\gamma E} \xi^\dagger_{\gamma E}. \tag{3.27}$$

The occupation function f_0 is the occupation of the scattering region at the initial time $t = -\infty$. We suppose the occupation in the central region and the occupation in the leads are equal and correspond to a Fermi occupation. This is the case if interaction

processes have occurred far in the past and have coupled bound states to the continuum. The wave functions are recovered with the action of the Green's function

$$(1 + G^R_{00}\Sigma^R)g^<(1 + \Sigma_A G^A_{00}) = \sum_\gamma f_0(E)\psi_{\gamma E}(t)\psi_{\gamma E}(t')^\dagger, \tag{3.28}$$

where wave functions obey the equation of motion 3.25 by replacing $\sqrt{v_\alpha}e^{-\frac{i}{\hbar}Et}\xi_{\alpha E}$ by the its equivalent for bound states $e^{-\frac{i}{\hbar}Et}\xi_{\gamma E}$,

$$i\hbar\partial_t\psi_{\gamma E} = \hat{H}(t)\psi_{\alpha E} + e^{-i\frac{E}{\hbar}t}\xi_{\gamma E}. \tag{3.29}$$

3.3 An algorithm for time-dependent simulation

Results of the previous section are gathered into the equation

$$G^<(t,t') = \sum_\alpha \int \frac{dE}{2\pi} i f_\alpha(E)\psi_{\alpha E}(t)\psi_{\alpha E}(t')^\dagger + \sum_\gamma f_0(E)\psi_{\gamma E}(t)\psi_{\gamma E}(t')^\dagger, \tag{3.30}$$

where γ sum on all propagating modes and γ sum over all bound states. The wave functions of propagating modes follow the equation

$$i\partial_t\psi_{\alpha E} = \hat{H}(t)\psi_{\alpha E} + \sqrt{v_\alpha}e^{-\frac{i}{\hbar}Et}\xi_{\alpha E}, \tag{3.31}$$

where $\sqrt{v_\alpha} = 1$ for wave functions corresponding to bound states. The combination of Eq. 3.30 and Eq. 3.31 is the basis for numerical calculations.

Numerical methods of resolution of this set of equation where already know from Ref. [25]. Unfortunately, the numerical algorithms used were not very accurate and quite costly in terms of computing time. A large part of the thesis consisted in refining the different numerical methods to improve both accuracy and computation time, thus opening the doors to more expensive simulations such as those including the environment. This rather technical section describes the numerical methods used to efficiently solve the equations Eq. 3.30 and Eq. 3.31.

3.3.1 Search for initial wave functions

The first step is to obtain the initial conditions for the equations of motion, wave functions $\psi_{\alpha E}(t = 0)$ for all energies and modes.

The propagative case

The time-dependent perturbation is activated at $t \geq 0$. Before the time-dependent perturbation, the wave functions are solutions of the stationary equation derived from Eq. 3.31,

$$[\hbar E - \hat{H}_0 - \Sigma^R(E)]\psi_s t = \sqrt{v_\alpha}\xi_{\alpha E}, \tag{3.32}$$

where $\hat{H}_0 = \hat{H}(t \leq 0)$ is the Hamiltonian without time-dependent perturbation. There are many standard techniques available to obtain the solution of this equation. The Kwant package [24] is an open-source quantum transport software whose performance is among the best for this type of problem. The resolution is obtained using a tight-binding model. The quasi-periodicity of the lead allows the semi-infinite equation 3.32 to be reduced to a linear system of finite size equations. The result of the algorithm are the numerical values of the wave function at each site. We refer the reader to the website of Kwant [32] for more details.

The bound state case

Bound states are eigenstates of the Hamiltonian that do not propagate in the lead, where they decay exponentially. For a finite size system with a quadratic Hamiltonian

$$\hat{H}_0 = \sum_{ij} h_{ij}\hat{c}_i^\dagger \hat{c}_j, \tag{3.33}$$

where h is a $N \times N$ matrix with N the number of sites in the central region. The energies of bound states is given by the eigenvalues of the h matrix and the associated eigenvectors give the values of wave functions.

In the case of a system with semi-infinite lead, direct diagonalization is not possible. The standard method of resolution use the exponential decay of the wave function of bound state in all leads. The semi-infinite lead can be truncated after a sufficient length for the wave function to disappear. The semi-infinite lead is truncated after sufficient time for the wave function to disappear. The resulting finite Hamiltonian can be diagonalized by standard techniques to give an approximation of the wave function, up to the vanishing part. However this poses two problems, one is to estimate the length of decay required. A too short length gives a bad approximation, a too long length gives a too long calculation time. Another problem is that the length of decay can be arbitrarily long, which is usually the case for related states that are close in energy to a propagation mode.

Fortunately a method that doesn't require truncation is developed in Ref. [33]. They use a technique similar to that used in transportation software to reduce the problem

of an infinite Hamiltonian to the resolution of an equivalent finite size linear system. The algorithm has proven to be robust and as an advantage to be compatible with the Kwant package.

3.3.2 Time evolution of wave functions

The second step is too evolve the initial wave function by using the equations of motion Eq. 3.31.

$$i\partial_t \psi_{\alpha E} = \hat{H}(t)\psi_{\alpha E} + \sqrt{v_\alpha} e^{-\frac{i}{\hbar}Et}\xi_{\alpha E}.$$

For $t \leq 0$ there is no time-dependent perturbation, by definition of the stationary initial conditions the solution are trivial

$$\psi_{\alpha E}(t) = e^{-iEt}\psi_{\alpha E}(0), \ \forall t \leq 0. \tag{3.34}$$

For $t > 0$ the time-dependent perturbation is turned on, a standard linear differential is obtained which is effectively integrated by the Runge-Kutta methods [34]. However wave-functions are define on an infinite system, inaccessible to numerical resolution. Two properties are used to reduce the size of the simulation to a finite size.

First all the time-dependent perturbation are gathered $\hat{H}_t(t)$ into the central region. If the time-dependent disturbance is present at a finite number of sites, the central region is defined as encompassing all time-dependent sites. If a time-dependent perturbation $V(t)$ applies to a semi-infinite lead, the wave function ψ and the Hamiltonian function $\hat{H}$ are decomposed into the lead part (label l), the diffusion region (label s) and the interface (label sl). In this cases the equation of motion reads as follows

$$i\hbar\partial_t \psi = \hat{H}_s\psi_s + (\hat{H}_l + V(t))\psi_l + \hat{H}_{sl}\psi + \sqrt{v_\alpha} e^{-\frac{i}{\hbar}Et}\xi_{\alpha E}. \tag{3.35}$$

The gauge transformation is applied in the part of the wave function in the lead with $\tilde{\psi}_l = e^{-i\int V(t)}\psi_l$ and $\tilde{\psi}_s = \psi_s$

$$i\hbar\partial_t \tilde{\psi} = \hat{\tilde{H}}(t)\tilde{\psi} + \sqrt{v_\alpha} e^{-\frac{i}{\hbar}Et}\xi_{\alpha E}, \tag{3.36}$$

where $\hat{\tilde{H}} = \hat{H}_s + \hat{H}_l + \hat{H}_{sl}e^{i\int V(t)}$. Now the lead is time-independent and only the interface with the central region is time-dependent.

For $t \leq$ the stationary solution and the real solution are the same. For $t > 0$ the time-dependent perturbation is located only in the central region, and physical signals always have a maximal propagation speed, noted v_{max}. So at time t the difference between the stationary wave function and the time-dependent wave function are limited in a region $L < t \times v_{max}$ around the central region. Thus only a finite region around

the central region is useful for numerical simulation. It is done by considering only the difference $\psi^d_{\alpha E}$ between the extended stationary solution and the time-dependent solution

$$\psi^d_{\alpha E}(t) = \tilde{\psi}_{\alpha E}(t) - \psi_{\alpha E}(0) e^{\frac{i}{\hbar} E t}. \tag{3.37}$$

The equation of motion for the difference is obtained by combining the equation of motion of each part,

$$i\partial_t \psi^d_{\alpha E} = \hat{\tilde{H}} \psi^d_{\alpha E} + \hat{H}_t e^{-\frac{i}{\hbar} E t} \psi_{\alpha E}(0), \tag{3.38}$$

where the Hamiltonian breaks down into time-dependent part and the stationary part $\hat{\tilde{H}} = \hat{\tilde{H}}_0 + \hat{\tilde{H}}_t$.

3.3.3 Absorbing boundary conditions

The size of the system can be further reduced by noting that in most systems, there is no backscatter from the leads to the central region, which means that all the information sent to the leads never returns to the central region. This can be used to truncate the system before the length $v_{max} t_{\max}$. An imaginary potential in leads is a way to absorb outgoing signals. The basis of the method is developed in Ref. [25] and has been completed by Thomas Kloss. The difficulty is to create an imaginary potential strong enough to absorb the outgoing signals but smooth enough not to create backscatter.

In a semi-infinite periodic lead, any physical signal can be decomposed into a sum of standing wave function

$$\psi(t) = \sum_\alpha \int dE \, \langle \psi_{\alpha E} | \psi(t) \rangle \, \psi_{\alpha E} e^{-\frac{i}{\hbar} E t}. \tag{3.39}$$

To ensure that the signal is correctly absorbed at all times, it is sufficient to verify that the standing wave function of all modes and energies, $\psi_{\alpha E}$, are absorbed by the imaginary potential. To simplify the calculation of the absorption, we limit ourselves to the case of a 1D lead, with the dimension noted x. The amplitude of the imaginary potential is noted $\Sigma(x)$, the stationary solution in an imaginary potential is given by the Shrödinger equation, in natural units it is read

$$-i\hbar\partial_t \psi_{\alpha E} - i\Sigma \psi_{\alpha E} = E \psi_{\alpha E}. \tag{3.40}$$

The wave function is decomposed into a superposition of incoming and outgoing plane waves

$$\psi_{\alpha E} = e^{ikx} + r_\Sigma e^{-ikx}, \tag{3.41}$$

where r_Σ is the reflection coefficient that must be minimized, k is the momenta from mode α at energy E. The following calculation is placed in the case of a parabolic band $E = \gamma^2 k^2$. Following [25] the result for the absorption coefficient is

$$r_\Sigma = e^{2i\gamma kL} e^{-A\gamma k/E} + \frac{1}{4iEL} \int_0^\infty \Sigma'(u) \exp\left[2i\gamma kLu - \frac{\gamma k}{E} \int_0^u \Sigma(v)dv\right] du. \tag{3.42}$$

where L is the length over which the imaginary potential is applied, and $A = \int_0^\infty \Sigma$ is the area below the potential. The first term takes into account absorption by the imaginary potential and is proportional to $e^{-A\gamma k/E}$. The second term takes into account the reflection of the wave function by the variation of the imaginary potential, characterized by the derivative of the potential Σ'. From a numerical point of view, the objective is to minimize the truncation length L to reduce the number of sites in the tight binding model.

No general solution have been found, so to proceed further the shape of the potential is chosen to have a polynomial shape

$$\Sigma(u) = (n+1)Au^n, \tag{3.43}$$

where the degree n and the amplitude A are two parameters to be determined. The reflection amplitude is simplified by

$$r_\Sigma = e^{-A\gamma k/E} + \frac{An(n+1)(n-1)!}{2^{n+2}E(\gamma k)^n L^{n+1}}, \tag{3.44}$$

valid for $n > 0$ and the phase factor $e^{2i\gamma kL}$ has been neglected.

Unfortunately for modes with a momentum close to zero $k \to 0$, the equation 3.44 implies that the minimum length can be arbitrarily large $L \to \infty$. Modes with low momentum k also have slow speeds $v = dE/dk = 2\gamma^2 k$. But if a buffer zone of length L_{buff} is placed between the central part and the imaginary potential, slow modes ($v < L_{\text{buff}}/2t_{max}$) does not have time to propagate to the imaginary potential, backscatter and come back into the central region during the time of the simulation. Thus fast mode are absorbed by the imaginary potential while slow mode are stuck in the buffer zone.

The objective is to reduce the total number of sites given by the length of the buffer zone plus the length of the imaginary potential. For each lead, the band structures are calculated, the slowest modes are identified by the curvature of the band structures and minimization techniques based on Eq. 3.44 are applied to find the minimum length for the buffer zone and the imaginary potential. Empirically the total length obtained scales as $\sqrt{v_{max}t_{max}}$ which is an improvement over the classical truncation method scaling has $v_{max}t_{max}$.

3.3.4 Band structure integration

The Green's function is calculated by an integral over energy with the evolved wave functions of the previous sections. Unfortunately, there are discrepancies in integration. The dual transverse wave functions are renormalized by their speed by $\epsilon_{\alpha E} \propto 1/v_{\alpha E}$. The wave function is related to the dual transverse wave function by Eq. 3.32, it follow that $\psi_{\alpha E} \propto 1/\sqrt{v_{\alpha E}}$. For a parabolic band $E = \gamma^2 k^2$, $v = dE_\alpha(k)/dk = 2\gamma\sqrt{E}$, the integral over energy presents a square root divergence. This type of divergence is numerically integrable $\int \psi\psi^* = \int E^{-1/2} = 2\sqrt{E}$, however they are difficult to integrate numerically.

A given mode can have several solutions at the same energy E. The accumulation of solutions near the same energy is the source of the divergencies. For each mode there is a unique solution for each momentum k, which avoids the divergences of the integrator. To eliminate the divergence, the change of the variable $k = E(k)$ is used in the integral to integrate along the momentum axis. For each band α there is a unique function $E_\alpha(k)$, the change of variable is valid and the integral is written

$$\int \frac{dE}{2\pi} i f_\alpha(E)\psi_{\alpha E}(t)\psi_{\alpha E}(t')^\dagger = \int \frac{dk}{2\pi} v_{\alpha k} i f_\alpha(E(k))\psi_{\alpha k}(t)\psi_{\alpha k}(t')^\dagger. \tag{3.45}$$

The new $v_{\alpha k}$ factor cancels exactly the divergence of the wave function. The integral along momentum doesn't have divergence and the wave functions are the same, computed at the right point $\psi_{\alpha k} = \psi_{\alpha E_\alpha(k)}$.

3.3.5 Numerical Integration

There are many standard techniques to numerically integrate the continuous integral over momentum. The main difficulty here comes from the number of integrations to be performed, which are linearly scaled with the number of modes, the number of bands and the number of time steps in the simulation. If each integral is treated independently, the total cost of the simulation becomes prohibitive. Fortunately, there are multiple crossovers in the calculation of our integrals. Intelligent manipulation of these properties can greatly speed up simulations. This section describes the methods we have developed for our problem, in order to minimize the cost of computation. An example of the integrand in momenta is shown in Fig. 3.2 to give an idea of the functions we are trying to integrate.

Polynomial integration

The most efficient integration methods are based on polynomial interpolation. The integral is approached by a piecewise polynomial of finite degree, then polynomials can

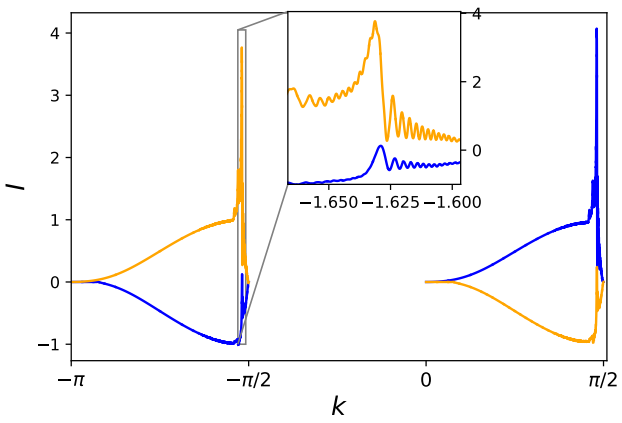

Figure 3.2: Example of mode contributions to the integral. From a Josephson Junction simulation under a voltage ramp. The integrand has many clear characteristics and compensation between all parties. The inset panel is a zoom of the main panel, it enlightens the sharp features of the integrand. An adaptive algorithm is required to effectively integrate this function. The colors indicate to which lead the modes belong.

be integrated exactly. The following method is based on the thesis of Pedro Gonnet [35] and was developed in collaboration with Christoph Groth.

The goal is to approximate a function $f(x)$ on the interval $x \in [a, b]$ by a polynomial $P(x) = \sum_{i=0}^{N} c_i P_i(x)$ where $P_i(x)_i$ form a base of the polynomials of degree $\leq N$. To fully evaluate a polynomial of degree N, $N+1$ values of the function are required. A set of $N+1$ nodes $(x_0, \ldots, x_N)$ is selected, the coefficients of P are determined such that $\forall n, P(x_n) = f(x_n)$. The coefficients verify the following equation

$$\forall n, \sum_{i=0}^{N} c_i P_i(x_n) = f(x_n). \tag{3.46}$$

This can be rewritten in a linear equation of matrices using the vector $\hat{C} = (c_0, \ldots, c_n)$, the vector $\hat{F} = (f(x_0), \ldots, f(x_n))$ and the matrix $V_{ij} = P_i(x_j)$ also called Vandermonde matrix of the polynomial set P_{ii}. The linear system is written

$$V\vec{C} = \vec{F}. \tag{3.47}$$

The system admits a single solution if P is invertible, the solution is given by $\hat{C} = V^{-1}\hat{F}$. The matrix is invertible when the nodes set consisting of unique points $\forall i \neq j, x_i \neq x_j$, and for polynomial sets forming a base of the space vector of polynomials of degree

$\leq N$. The interpolation of f on $[a,b]$ by a polynomial is given by

$$f(x) \simeq \sum_{i=0}^{N} c_i P_i(x). \tag{3.48}$$

It follows the approximation of the integral of f by

$$\int_a^b f(x)dx \simeq \sum_{i=0}^{N} c_i \int_a^b P_i(x)dx. \tag{3.49}$$

The Legendre polynomials L_i are used has a basis. They have the property $\int_{-1}^{1} L_i(x)dx = \delta_i$. Only the polynomial L_0 has a non-zero integral over the interval $[-1,1]$. A linear mapping of the interval $[a,b]$ to the interval $[-1,1]$ is defined as follows

$$m = \begin{cases} [a,b] \to [-1,1] \\ x \to (2x-b-a)/(b-a) \end{cases} . \tag{3.50}$$

The polynomial base used for interpolation is obtained from Legendre polynomials and the linear mapping, $P_i(x) = L_i(m(x))$. The integral takes the form of

$$\int_a^b f(x)dx \simeq (b-a)\sum_{i=0}^{N} c_i \int_{-1}^{1} L_i(x)dx = (b-a)c_0. \tag{3.51}$$

The coefficient of the first Legendre polynomial c_0 is obtained by the scalar product

$$c_0 = (V^{-1})_{0i}.\vec{F}, \tag{3.52}$$

where $(V^{-1})_{0i}$ is the first line of the inverse Vandermonde matrix. Due to mapping, the inverse Vandermonde matrix depends only on the choice of nodes over the $[-1,1]$ interval and not on $[a,b]$. It is effective to pre-calculate the inverse Vandermonde matrix if the same nodes are used for all intervals of the piecewise approximation.

Polynomial interpolations have a problem with the Runge phenomenon, where the interpolated polynomial oscillates a lot at the limits of the interval. This effect is maximized by uniform sampling of x_i nodes. There are many nodes that limit the Runge phenomenon. We will use the Chebyshev nodes defined in the interval $[-1,1]$ per

$$x_k = \cos\left(\frac{k}{n}\pi\right). \tag{3.53}$$

Evaluation of the interpolation error

It is necessary to quantify the error induced by the polynomial approximation to obtain accurate integrals. The standard method for estimating the error is to use two different polynomial interpolations of the same function. The integral is interpolated with a polynomial of degree N and another polynomial of degree M, the difference between the two integrals gives an estimate of the error between the interpolated integral and the true integral.

A simple way to calculate the error is to make the difference in the value of the integral obtained by the two polynomials

$$\epsilon = \left| \int_a^b (P_N - P_M) \right|. \tag{3.54}$$

Unfortunately, this method is not reliable because the probability that the two estimated integrals are close to each other is quite high. Let take a function f approximated by $|\int f - \int P_N| = \mu_N$ and $|\int f - \int P_M| = \mu_M$. The estimated error has two possibilities $|\int P_M - \int P_N| = |\mu_N \pm \mu_M|$. For values of μ_N and μ_M close to each other the estimated error can be far below the real error $|\mu_N - \mu_M| \ll \mu_N$. A more accurate error estimator uses the L^2 norm, in terms of coefficients it reads

$$\epsilon = \int_a^b \left(P_N(x) - P_N(x) - P_N(x) - P_M\right)^2 dx = \sum_{i=0}^{N} (c_{N,i} - c_{M,i})^2 + \sum_{i=N}^{M} c_{N,i}^2, \tag{3.55}$$

where $N \leq M$. In this case, the error is only underestimated if all the coefficients $c_{N,i}$ and $c_{M,i}$ are close to each other, which is much less likely.

Using the same nodes for both interpolations limits the number of calls to the function. The idea is to use two different degrees $N < M$ to obtain different interpolations. We used Chebyshev nodes of order $N + 1$ and $2N + 1$ to evaluate the error.

Refine integration

There are many ways to refine a quadrature when the required accuracy is not achieved. Following the advice of [35] we combine polynomial degree enhancement methods with piecewize methods. We combine both approaches in an adaptive scheme. From a set of intervals to integrate i, the interpolation error is estimated for each interval ϵ_i. If the total error is greater than the requested accuracy $\sum_i \epsilon_i > \mu$, the interval with the largest estimated error is chosen for refinement. The interval is refined by increasing the degree or dividing the interval into two sub-intervals. The process is repeated until the required accuracy is achieved. An integrator prototype implementing all the details

described, as well as others such as parallel integration and discrepancy detection is available online at Ref. [36].

3.3.6 Reducing computational costs

The previous sections describe a method for performing an integral at a fixed time $G^<(t,t')$. In the following we consider only the case of equal time $G^<(t,t)$. We have summarized the steps necessary to calculate the integral at the moment t with the precision μ,

1. For each mode α, select nodes in momenta $k_{\alpha 0}, \ldots, \ldots k_{\alpha N}$.
2. For each point $k_{\alpha i}$ calculate the stationary wave function $\psi_{\alpha k}(t_0)$.
3. Evolve each waves functions up to time t, to get $\psi_{\alpha k}(t)$.
4. Sum the contribution and estimate interpolation errors.
5. - If the precision is not satisfied, go back to step 1 with new nodes.
   - If the precision is satisfied, calculate the final values of the integral.

The above method is optimized to calculate a single Green's function at a given time. In most simulations, it is necessary to calculate the Green's function at several different times. Performing each calculation independently becomes quickly prohibitively expensive as the number of time steps increases.

Momenta sampling The calculation of a wave function at a specific time requires the calculation of the values at all other times. Thus each wave function (with its value at each step) is a common object in the calculation of all Green's functions, regardless of the time. On other hand, integrals of Green's function at different times have different shapes and require different sampling points to be numerically integrated with precision. Thus, the set of wave functions required will be different for different times. To optimize the simulations, each wave function should be used to calculate integrals by the largest number of time steps. In cases where the Hamiltonian of the system depends on the measured value history of some operators it is required to calculate the Green's function in ascending time order. To minimize the total number of wave function, each time time use the same nodes as the previous time step, plus some extra points if the accuracy is not reached.

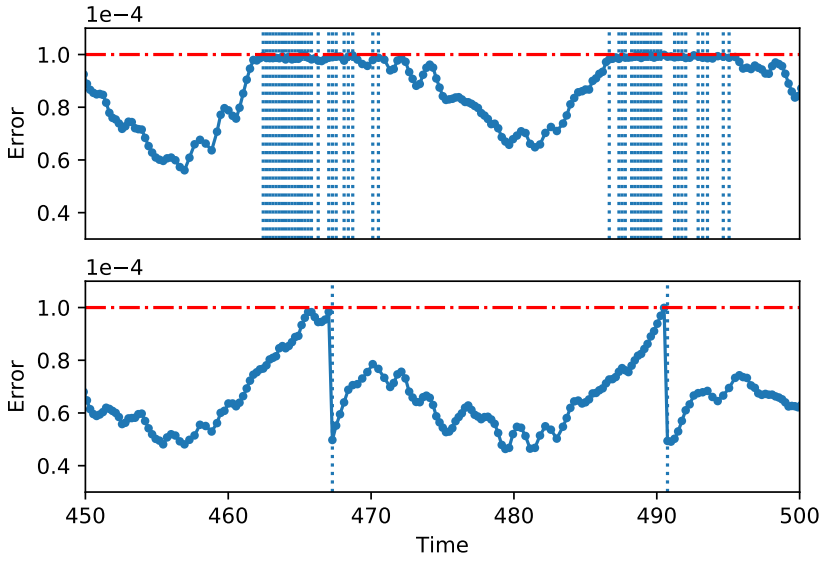

Figure 3.3: Errors estimated as a function of time, the red dashed line is the requested accuracy, and the vertical dotted lines correspond to the moments with a refinement made. In the top panel, a minimal algorithm is applied, with each refinement using only a tiny fraction of the total CPUs. In the lower panel, almost all CPUs are occupied during the refinement and the additional wave functions are built into the result. This reduces the number of future refinements because the wave functions are pre-calculated. The number of refinements is significantly reduced and the simulation time is reduced accordingly. Data from a simulation of a Josephson junction under constant voltage.

Parallel computing Each wave function is an independent object from the other wave functions, the evolution of a set of wave functions is adapted to parallel computation. The difficulty is to distribute the task correctly between the CPUs. When additional nodes are added to the quadrature to achieve accuracy, the associated wave functions have to be evolved from the initial time to the integral time, which takes a lot of time to compute. If the number of new wave functions is less than the number of CPUs used, the CPUs without new wave functions are without work. Due to the sequential calculation of integrals, their free time cannot be used to evolve wave functions further in time. Instead, their time can be used to calculate additional wave functions assuming that they will be useful in the future. To predict the usefulness of a wave function, we assume that the shape of the integral will change slowly with respect to the time step, so the shape of the current integral is used to predict the future usefulness of

wave functions. This method saves a lot of simulation time, as shown in the example of the figure 3.3 where the simulation is 10 times faster with intelligent CPU management.

3.4 Environment

The algorithm of the previous section can be summarized in a simple way: given a quadratic Hamiltonian depending on time and initial conditions, we are able to compute expectation values of observable at any time. In this formalism, the Hamiltonian models the structure of the quantum system with its shape and the various parameters characterizing the materials, and also takes into account the time-dependent perturbations imposed by the environment outside the quantum system, such as voltage and magnetic field. On the other hand, the expectation values of observables measured on the system correspond to the outputs of the system, such as current and electron densities, which are perceived by the environment outside the quantum system.

Let's take the example of a josephson junction. It is an element consisting of two superconductors connected by a small piece of normal metal. This system will be discussed in more detail in chapter 5. When a voltage $V(t)$ is applied to the boundary of a Josephson junction, a current $I(t)$ flows through the junction. The algorithm in the previous section can be applied to calculate the current produced for different types of voltages, see Ref. [25]. The voltage is modeled by time dependence of the Hamiltonian while the current is obtained by calculating the expected value of the observable current. On a macroscopic scale, a junction behaves like an electronic component, with a non-linear current-voltage relationship. It can be inserted into an electronic circuit. The voltage is given by the state of the circuit at each moment, but the current produced by the junction changes the state of the circuit. Thus the voltage across the junction is related to the current of the junction via the dynamics of the circuit. We have coupled the Hamiltonian to the expectation value of observables. In a more general way, we consider as environment each element of the model that couples the Hamiltonian to the expectation values of the observable.

Solving the equations coupling the environment and the quantum system is quite simple when we already have an algorithm for the quantum part only. Assuming we know the Hamiltonian $\hat{H}$ and the expectation value of observable $\langle \hat{O} \rangle$ at time t. First the expectation value are extrapolated to the next time step, then a new Hamiltonian is computed using the dynamics of the circuit and the extrapolated expectation values, then the expectation value is re-evaluated by evolving the system with the new Hamiltonian, finally the the extrapolated values are compared to its re-evaluated value to update the simulation time step. This methode have been develloped in collabaration with Thomas Kloss and is used in [37] to simulate Luttinger Liquids where the potential

inside the system (Hamiltonian) is directly dependent on the density of the electron in the system (density operator).

Extrapolation and adaptive time steps are very simple methods. The difficulty will come on the one hand from the calculation of the expectation values from the Hamiltonian, this is the goal of the algorithm developed in the first part of the chapter. The other difficult part may come from the calculation of the Hamiltonian from the expectation value, which is given by the dynamics of the environment. In some cases, the expectation value gives directly the hamiltonian as in Ref. [37]. In the cases presented in the chapter 5 the dynamics of the environment is given by a differential equation that require using Runge-Kutta methods. An example of a complex environment could be a simulation where the entire self-consistent electrostatic potential of the system is dynamically updated, which would require solving the Poisson's equations many times.

To sum up, adding the environment is simple when a high-performance quantum transport algorithm is available.

3.5 Summary

Using the formalism of the Green's function, the problem of a time-dependent scattering region related to semi-infinite lead is simplified into a problem of evolution of a set of finite size wave functions. This problem can be numerically integrated and is suitable for parallel computing. An algorithm is obtained by combining the existing software [24], [33] and [34]. The emphasis is on the accuracy and parallelism of the algorithm. With this element, the inclusion of the environment is straightforward.

Chapter 4

Spectroscopy of flying qubit

4.1 Introduction

While the coherent control of two level quantum systems —qubits— is now standard, their continuum electronic equivalents —flying qubits— are much less developed. A first step in this direction has been achieved in DC interferometry experiments. In this chapter, we propose a simple setup to perform the second step, the spectroscopy of these flying qubits, by measuring the DC response to a high frequency ac voltage drive. Using two different concurring approaches — Floquet theory and time-dependent simulations — and three different models — an analytical model, a simple microscopic model and a realistic microscopic model — we predict the power-frequency map of the multi-terminal device. We argue that this spectroscopy provides a direct measurement of the flying qubit characteristic frequencies and a key validation for more advanced quantum manipulations.

The development of a new type of quantum bit happens in stages. Let us consider the singlet-triplet double quantum dot qubit [38] as a typical example. In this case, the first stage consists of DC measurements of the so-called stability diagram. Once a suitable physical regime has been found, stage II consists of performing the spectroscopy of the qubit to assert its suitability and determine its dynamical characteristics. This can be done through, e.g. electronic dipolar spin resonance (EDSR) [39]. It is crucial to pass these two stages before one can consider sending more elaborated pulse sequences like Rabi, Ramsey and echo experiments. In the last stage (before considering coupling several of these qubits), one implements single shot measurements.

Quantum mechanics, however, is not limited to bound states and propagating quantum states instead of bound states could also be used to form qubits. The so-called flying qubits have been successfully realized with photons in linear quantum optics

[40; 41] but here we focus on proposals based on electrons [42]. The first stage of the electronic flying qubit [43; 44] implementation has been demonstrated in several experiments that show controlled two paths interferometry in two-dimensional electron gas in the presence [45; 46] or absence [4; 47] of magnetic field as well as in graphene [48]. Other features, specific to propagating quantum systems, have also been demonstrated (including single electron sources [49; 50; 51; 52] and their Hong-ou-Mandel characterization) or proposed theoretically [53; 54; 55]. However stage II, the spectroscopy of a flying qubit, has not yet been realized experimentally.

The electronic flying qubits that we consider in this chapter are "two paths" interferometers, the electronic analog of the Mach-Zehnder interferometer studied in optics. The two states of the qubits are coded in the two paths $\uparrow$ or $\downarrow$ that a single electronic excitations use for propagation. Here the role of the qubit frequency is replaced by $\hbar/\tau$ where τ is a characteristic time, a difference between two times of flight (to be defined below), of the device. Similarly to localized system that may have multiple energy levels, there may be several propagating channels giving rise to several characteristic times τ. Measuring these times and assessing that electronic interferometry experiments can be performed at high frequency is the next key milestone of the field.

In this chapter, we propose to use quantum rectification (measurement of a DC current in the presence of a high frequency sinusoidal drive) [56; 57; 58; 59; 60; 58; 61] as a tool to perform the spectroscopy of flying qubits. We argue that quantum rectification provides a clear spectroscopy of the device while being much more accessible experimentally than other techniques, in particular in the challenging $\sim 10\,\mathrm{GHz} - 1\,\mathrm{THz}$ frequency range, which is required for this type of physics.

4.2 A two paths electronic interferometer using a split wire geometry

We focus this study on the tunneling wire "flying qubit" geometry presented in Fig. 4.1 and sketched in Fig. 4.2a and studied experimentally in [47; 4; 62; 63]. The device consists of two quasi one-dimensional wires labeled $\uparrow$ (upper) and $\downarrow$ (lower) connected to four electrodes: two on the left L$\uparrow$, L$\downarrow$, and two on the right R$\uparrow$, R$\downarrow$. Close to the electrodes, the wires are disconnected. However, in a central region of length $\mathcal{L}$, the two wires are in contact so that an electron can tunnel back and forth from the upper to the lower part. A capacitive top gate V_g controls the intensity of the tunneling coupling between the wires. The coherent oscillation that takes place in the tunneling region between the upper and lower wire can be interpreted as a quantum gate operated on the flying qubit. Equivalently, an electron entering the upper wire decomposes into

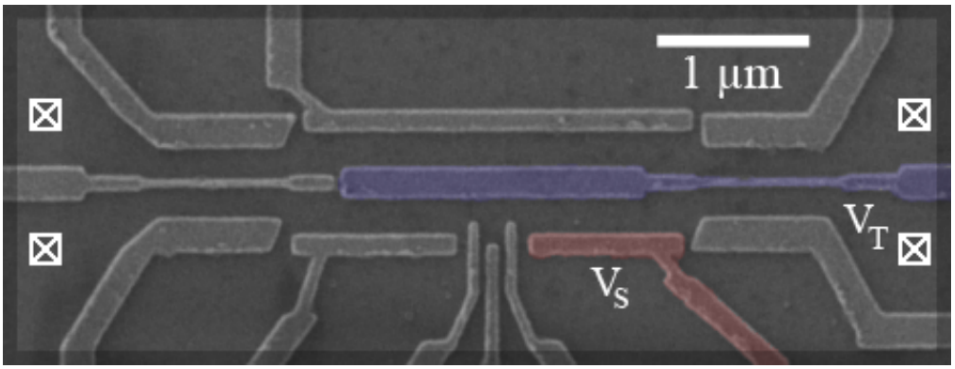

Figure 4.1: Scanning electron microscope image of the aircraft in flight qubit sample, image from [4]. The white square represents the ohmic contact of the upper left, lower and upper right, upper and lower probes. The blue door is used to adjust the splitting in the central region.

a superposition of symmetric and antisymmetric propagating states, which forms a two-path interferometer.

The dc characteristics of this device have been analyzed previously [4; 64] both theoretically and experimentally. For completeness, we recall here its salient features. Let us determine the scattering matrix of this device in the limit where (i) there is only one propagating channel in each of the wires and (ii) the spatial variation of the tunneling coupling is very smooth with respect to the Fermi wave length. This implies that there is no reflection in the device as backscattering involves the $2k_F$ Fourier component of the potential (k_F is the Fermi momentum): an electron injected on the left, say in L$\uparrow$ is transmitted either toward R$\uparrow$ or R$\downarrow$. To determine the transmission amplitude $d_{ba}(E)$ from channel a on the left to channel b on the right ($a, b \in \{\uparrow, \downarrow\}$), let us consider the transverse part of the propagating modes. A schematic representation of these wavefunctions is shown in Fig. 4.2b for the decoupled wires (close to the electrodes) and in Fig. 4.2c for the tunneling region. In the latter, the $\uparrow$ and $\downarrow$ channels hybridize into a symmetric S and an antisymmetric A channels of respective longitudinal momentum k_S and k_A along the x direction. The key point is to recognize that the S (A) channel is continuously connected to the symmetric (anti-symmetric) combination of the $\uparrow$ and $\downarrow$ channels, $|S/A\rangle \leftrightarrow (|\uparrow\rangle \pm |\downarrow\rangle)/\sqrt{2}$. Hence an electron injected in $|\uparrow\rangle$,

$$|\uparrow\rangle = \frac{1}{2}(|\uparrow\rangle + |\downarrow\rangle) + \frac{1}{2}(|\uparrow\rangle - |\downarrow\rangle) \rightarrow \frac{1}{\sqrt{2}}(|S\rangle + |A\rangle), \tag{4.1}$$

is transmitted into S and A with amplitude $1/\sqrt{2}$. Inside the tunneling wire, the

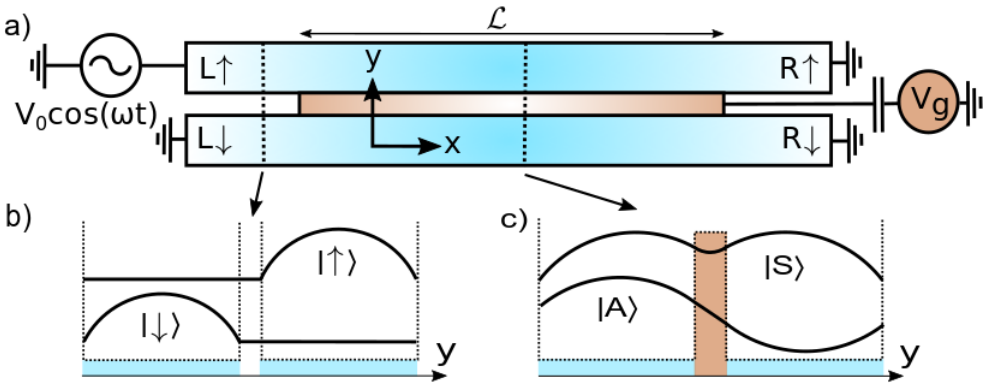

Figure 4.2: Upper panel: schematic of the flying qubit geometry. Two wires labeled ↑, ↓ are connected to two electrodes on the left (L↑, L↓) and two electrodes on the right (R↑, R↓). Lower panel: schematic of the transverse part of the propagating modes close to the electrodes (left) and in the central tunneling region (right).

wavefunction picks up a phase $e^{i\phi_{S/A}}$ which in the WKB approximation reads $\phi_{S/A} = \int_0^{\mathcal{L}} dx\ k_{S/A}(x) \approx k_{S/A}\mathcal{L}$. After the tunneling region, the S and A recombine into the ↑ and ↓ channels. The process is summarized in Fig. 4.3 and the result is

$$d_{\uparrow\uparrow}(E) = \frac{1}{2}(e^{i\phi_S} + e^{i\phi_A}),\ d_{\downarrow\uparrow}(E) = \frac{1}{2}(e^{i\phi_S} - e^{i\phi_A}). \tag{4.2}$$

The differential conductance g_{ba} that relates the current flowing on the right in lead b from an increase of voltage in the left on lead a is given by the Landauer formula, $g_{ba} = (e^2/h)D_{ba}(E_F)$ with $D_{ba}(E_F) = |d_{ba}(E_F)|^2$ and E_F the Fermi energy (we ignore spin everywhere; it can be restored by simply multiplying the currents by a factor 2). The above analytic expressions have been shown to grasp the important features of the corresponding experimental devices in dc [4]. In particular, upon decreasing the gate voltage V_g toward large negative values, $k_S - k_A$ decreases towards zero (the two channels become increasingly alike) and the differential conductance $g_{\uparrow\uparrow} \propto \cos^2((\phi_S - \phi_A)/2) \approx \cos^2((k_S - k_A)\mathcal{L}/2)$ first oscillates, then saturates to perfect transmission.

For the AC response discussed in this article, we need the energy dependence of the transmission amplitude. Linearizing the dispersion relation of the S and A channels, we introduce the corresponding velocity $v_{S,A} = (1/\hbar)dE_{S,A}/dk$ and the time of flight $\tau_{S/A} = \mathcal{L}/v_{S,A}$ through the channel. The phase difference $\phi_S(E) - \phi_A(E)$ is controlled by the difference $\tau \equiv \tau_S - \tau_A$ of time of flight, and we arrive at

$$\phi_S(E) - \phi_A(E) \approx \delta_F + (E - E_F)\tau/\hbar, \tag{4.3}$$

with $\delta_F \equiv \phi_S(E_F) - \phi_A(E_F)$.

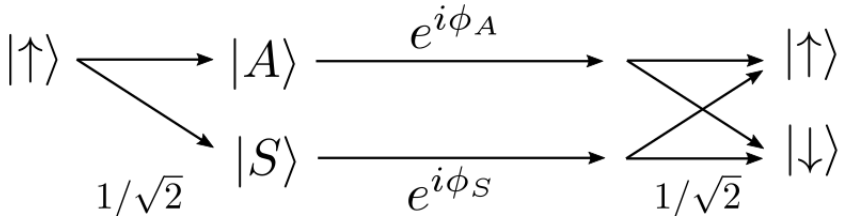

Figure 4.3: Mach-Zehnder interference analysis scheme. A signal sent in the upper left input mode $|\uparrow\rangle$ is spit in half between the corresponding symmetric and anti-symmetric center modes. The modes are spreading in the central region and gaining different phases. In the left interface, the symmetric and anti-symmetric modes recombine to create $|\uparrow\rangle$ at the top right and $|\downarrow\rangle$ at the bottom right.

4.3 A general formula for calculating rectification currents

We now develop the scattering theory of the rectified direct current generated by an ac voltage drive. We consider a multiterminal mesoscopic system and apply a periodic time-dependent voltage $V(t)$ to one electrode (for definiteness, we focus below on L$\uparrow$) with frequency ω. We seek to obtain the average (over time) dc current flowing in the different electrodes. Such a calculation can be performed in different but fully equivalent "Floquet" formalisms including the scattering [65], Non-equilibrium Green's function [66] or wave function approach [1]. Here, we follow the latter after Ref. [1; 55].

In what follows, we neglect the spatial dependence of the electric potential drop, i.e. we suppose that the drop of electric potential takes place very abruptly at the Ohmic contact - two-dimensional gas interface. Such an approximation is well justified in the present case due to the presence of the electrostatic gates that define the conducting region. These gates are metallic, hence equipotential; they ensure that the potential drop takes place on a distance which is essentially set by the distance between the gate and the two-dimensional electron gas. This distance is typically of the order of 100 nm which is much shorter than the size of the device (typically 10 μm) so that the approximation of perfectly sharp drop is reasonably accurate. In the opposite situation (absence of electrostatic gates) the potential drop would be linear between the two contacts. A discussion of this problem can be found in section 8.4 of [1]. The abrupt drop of potential is an important ingredient for the physics of propagating pulses such as the minimum excitations "Levitons". The recent experiments that measured the time of flight of such pulses [67] provide a clear experimental evidence that the drop is indeed sharp and take place at the Ohmic contact - electronic gas interface, since well

defined velocities could be measured.

The effect of the time-dependent voltage is to dress an incoming wave function of the form $e^{ikx-iEt/\hbar}$ with an extra phase factor $e^{-i\Phi(t)}$ [with $\Phi(t) \equiv \int_0^t dt'\ eV(t')/\hbar$] that accounts for the variation of electric potential. Decomposing this phase into its Fourier component P_n,

$$e^{-i\Phi(t)} = \sum_n P_n e^{-i\omega nt}, \tag{4.4}$$

the net effect of $V(t)$ is that the incoming wave function is now a coherent superposition $\sum_n P_n e^{ikx-iEt/\hbar-i\omega nt}$ of plane waves at different energy. As different energies get transmitted into different channels, we arrive at the following time-dependent transmission amplitude for an incoming energy E,

$$d_{ba}(t,E) = \sum_n P_n d_{ba}(E+n\hbar\omega) e^{-iEt/\hbar-i\omega nt}, \tag{4.5}$$

where $d_{ba}(t,E)$ is the Fourier transform with respect to E' of $d_{ba}(E',E)$ which is itself the inelastic amplitude to be transmitted from energy E, lead a toward energy E', lead b. The generalization of the Landauer formula to time-dependent currents provides the time-dependent current $I_b(t)$ as

$$I_b(t) = \frac{e}{\hbar}\int \frac{dE}{2\pi}\left[|d_{ba}(t,E)|^2 - |d_{ba}(E)|^2\right] f_a(E), \tag{4.6}$$

where $f_a(E)$ is the Fermi function of the lead a subject to the time-dependent voltage. The second term in the previous equation subtracts the current sent from lead a in the absence of time-dependent voltage which is a convenient way to ensure the overall current conservation [1; 53]. Focusing on the dc (rectification) current $\bar{I}_b = \omega/(2\pi)\int_0^{2\pi/\omega} dt I_b(t)$ we arrive at,

$$\bar{I}_b = \frac{e}{h}\sum_n |P_n|^2 \int dE |d_{ba}(E)|^2 \left[f_a(E+n\hbar\omega) - f_a(E)\right]. \tag{4.7}$$

Equation (4.7) is very general and relates the rectification properties of an arbitrary mesoscopic system to its scattering matrix $d_{ba}(E)$, a well known dc object. In particular, it can be easily evaluated numerically for a large class of microscopic models using readily available numerical packages (in our case the Kwant [24] package) for arbitrary periodic pulses. We note that following the same arguments as Ref. [1], we find that the rectification current is "conserved" and "gauge invariant" in the sens defined by Büttiker [68], i.e. the DC current in electrode a is exactly compensated by the dc currents in the other leads and applying an ac potential on all the leads simultaneously does not generate any dc current.

4.4 Application to the flying qubit

4.4.1 Simple scattering model

We now make a specific calculation using our analytical model Eq. (4.2) for the flying qubit geometry. We also specialize in a drive $V(t) = V_0 \cos \omega t$ with a unique frequency which implies $P_n = J_n(eV_0/\hbar\omega)$ where $J_n(x)$ is the Bessel function of the first kind. Up to an irrelevant phase factor, and by using the linear dispersion relation Eq.4.3, the time-dependent transmission reads,

$$d_{\uparrow\uparrow}(t, E) = \frac{1}{2}\left[1 + e^{i\delta_F + i\tau(E-E_F)/\hbar} e^{i\Phi(t)} e^{-i\Phi(t-\tau)}\right]. \tag{4.8}$$

Following the same route as in the general case, and assuming zero temperature for simplicity, we get,

$$\bar{I}_\uparrow = \frac{e}{4\pi\tau}\sin(\delta_F)\left[J_0\left(\frac{2eV_0}{\hbar\omega}\sin\left(\frac{\omega\tau}{2}\right)\right) - 1\right], \tag{4.9a}$$

$$\bar{I}_\downarrow = -\bar{I}_\uparrow. \tag{4.9b}$$

Eqs. (4.9a, 4.9b) call for a few comments. (i) Even though we apply the oscillatory voltage on the upper left electrode, no dc current actually flows there as implied by Eq. (4.9b) and current conservation. Instead, the dc rectified current is pumped from the upper right to the lower right electrode. (ii) Eq. (4.9a) is non-perturbative both with respect to frequency and drive amplitude. An illustrative color plot is shown in Fig. 4.4. It shows rich oscillatory features both as a function of ω and V_0. Fig. 4.4 is the flying qubit analogue of the usual spectroscopy maps. (iii) The adiabatic limit $\omega \to 0$ can be understood without using the time-dependent Floquet formalism. First, we compute the dc current-voltage characteristics

$$\begin{aligned} I(V) =& (e/h)\int_{E_F}^{E_F+eV} dE\ |d_{\uparrow\uparrow}(E)|^2 \\ =& \frac{e^2}{2h}V + \frac{e}{2\pi\tau}\sin\left(\frac{eV\tau}{2\hbar}\right)\cos\left(\delta_F + \frac{eV\tau}{2\hbar}\right). \end{aligned} \tag{4.10}$$

Then the adiabatic rectified dc current is found by computing the time average of $I(V = V_0 \cos \omega t)$ and we arrive at

$$\bar{I}_\uparrow = \frac{e}{4\pi\tau}\sin(\delta_F)\left[J_0\left(\frac{eV_0\tau}{\hbar}\right) - 1\right], \tag{4.11}$$

which corresponds to the $\omega \to 0$ limit of Eq. (4.9a). The rectified current is directly linked to the presence of the non-linear term in the $I(V)$ characteristics. (iv) At large

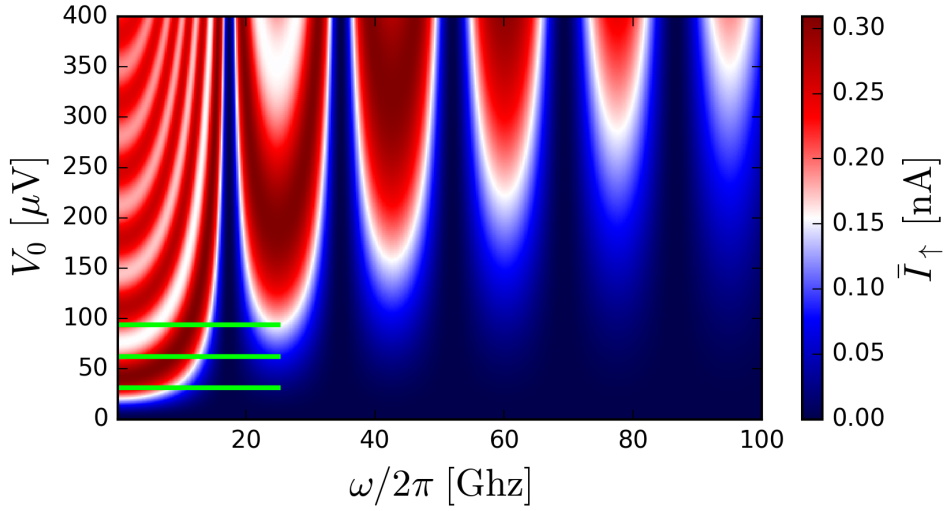

Figure 4.4: Rectified dc current from Eq. (4.9a) for $\delta_F = 0.32\pi$ and $\tau = 58\,\text{ps}$. Results of Fig. 4.7 correspond to cuts along the green lines.

x, the Bessel function decreases as $J_0(x) \sim \sin(x+\pi/4)\sqrt{2/\pi x}$ so that the rectified current reaches its maximum value $\bar{I}_\uparrow = -\frac{e}{4\pi\tau_F}\sin(\delta_F)$ at large voltage and $\omega\tau = \pi$.

4.4.2 Simple microscopic model

We now introduce a microscopic model for the Mach-Zehnder interferometer of Fig. 4.2 and discuss our direct method to perform time-dependent simulations of the device. We shall find a perfect match between our time-dependent simulations and a semi-analytical approach that uses the microscopic model to calculate the dc scattering matrix (using the Kwant package [24]) and Eq. (4.7) to relate the latter to the rectified current in the presence of an ac drive. We model the Mach-Zehnder interferometer through the following Hamiltonian,

$$\begin{aligned}\hat{H}(t) = &\sum_{a\in\{\uparrow,\downarrow\}}\sum_{i=-\infty}^{+\infty}\left[-c^\dagger_{i+1,a}c_{i,a} + U_i c^\dagger_{i,a}c_{i,a}\right] \\ &+ \sum_{i=-L/2}^{+L/2}\gamma_i c^\dagger_{i,\uparrow}c_{i,\downarrow} + h.c.,\end{aligned} \tag{4.12}$$

where $c_{i,a}$ ($c^\dagger_{i,a}$) is the usual fermionic destruction (creation) operator on site i and wire $a \in \{\uparrow,\downarrow\}$. U_i is an electric potential present in the central region, γ_i characterizes the

tunneling between the upper and lower wire and is controlled by the voltage V_g and L is the total length of the tunneling part of the wire. The nearest neighbor hopping amplitude is set to unity which defines our energy and time units ($\hbar = 1$).

For our simulations, we choose $L = 500$ sites, $E_F = 1.3$, γ_i interpolates smoothly (over 50 sites) between 0 in the electrodes and -0.7 in the tunneling region. The potential U_i interpolates smoothly between 0.8 in the electrode, 1 in a small region just before and after the tunneling region (this region is present for numerical convenience, see section 10 of Ref. [1]) and vanishes inside the tunneling region. Figure 4.5 resumes the parameters and the resulting variation of velocity across the interferometer. U_i also includes a uniform contribution $V_0 \cos(\omega t)$ for all sites in the upper left electrode and $t > 0$. For these parameters, we find a characteristic time $\tau \approx 58$ and $\delta_F \approx 0.32\pi$.

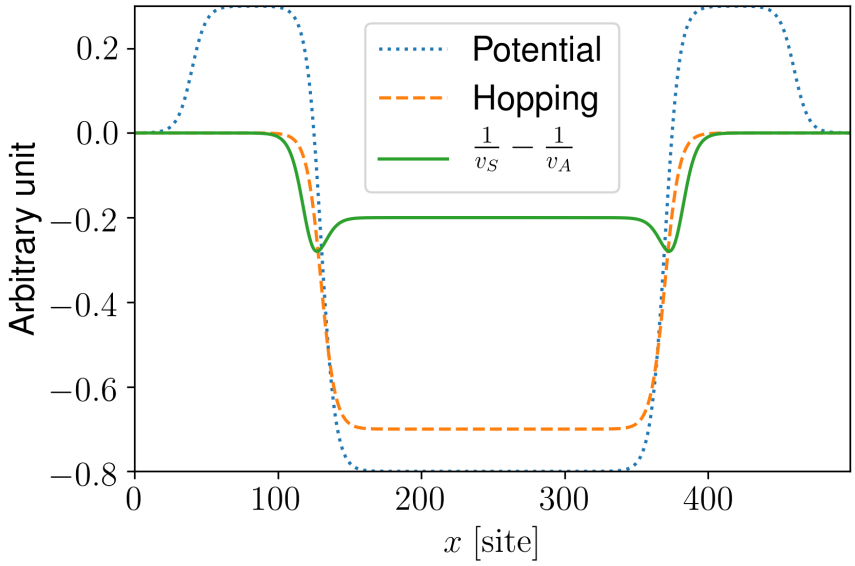

Figure 4.5: In straight blue, the potential on site through the interferometer. In the dotted orange, the jump between the sites at the top and the sites at the bottom. In straight green, is the speed difference between the two modes. The interaction region is located between sites 100 and 400, it is smoothly connected to the rest of the circuit.

These two values can be determined consistently from three different calculations: from the propagation of a voltage pulse in the time-dependent simulation, from the energy dependence of the dc conductance or from the WKB approximation.

The time-dependent simulations are performed using the method described in chap-

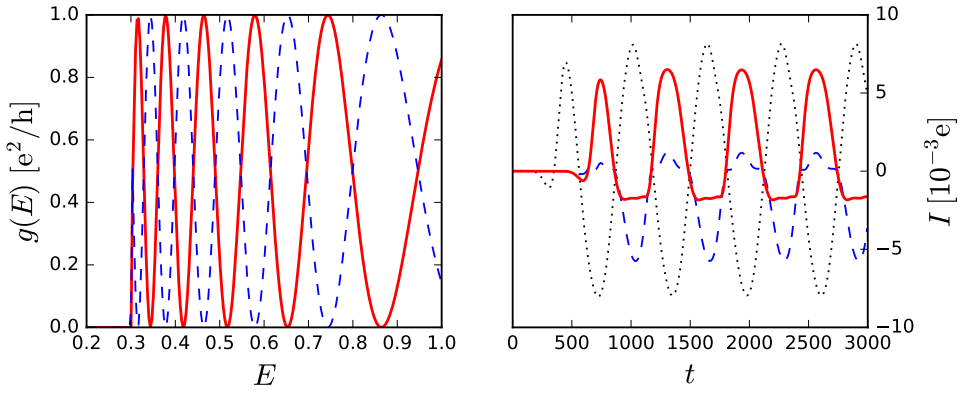

Figure 4.6: Simple microscopic model. Left panel: dc differential conductances $g_{\uparrow\uparrow}(E)$ (dashed blue line) and $g_{\downarrow\uparrow}(E)$ (straight red line) as obtained from a direct numerical calculation of the tight-binding model. The numerical calculations were performed with the Kwant [24] package. The reflection probability from L↑ to L↑ or L↓ vanishes in the region of interest. Right panel: currents in R↓ (straight red line, $I_\downarrow(t)$) and R↑ (dashed blue line, $I_\uparrow(t)$) after a microwave excitation in L↑ (dotted black line) computed using time-dependent simulations of the microscopic model.

ter 3. In this method, we directly integrate the Schrödinger equation

$$i\hbar\partial_t|\Psi(t)\rangle = \hat{H}(t)|\Psi(t)\rangle, \tag{4.13}$$

without further approximations. The main difference with Eq.(4.7) lies in the treatment of the oscillatory AC potential: in the scattering matrix approach, it is assumed that the ac potential drop does not create any backscattering. This approximation is usually very good, up to small deviations $\sim V_0/E_F$ that have been calculated in Ref. [1]. The left panel of Fig. 4.6 shows an example of the dc differential conductances $g_{\uparrow\uparrow}(E)$ and $g_{\downarrow\uparrow}(E)$ as obtained from a direct numerical calculation of the tight-binding "simple microscopic model". We indeed observe the oscillations with energy discussed after Eq. (4.2). We checked that the period of these oscillations matches the WKB result that can be calculated independently. The right panel of Fig. 4.6 shows the result (current $I(t)$ versus time t) of a typical time-dependent simulation of the model in the presence of the ac drive (smoothly switched on at $t = 0$). These curves are averaged over time to calculate the dc rectification current $\bar{I}$.

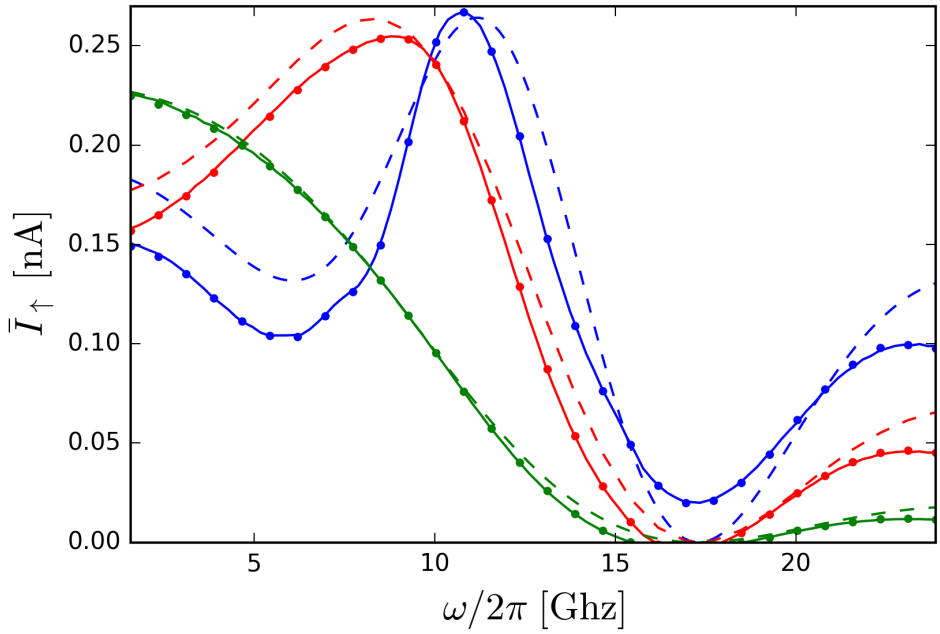

Figure 4.7: Simple microscopic model. dc current $\bar{I}_{\uparrow}$ for three different voltage amplitudes $V(t) = V_0 \cos(\omega t)$ with $V_0 = 31,\ 62,\ 93\,\mu$V (green, red, blue). The symbols correspond to the time-dependent simulation of Eq. (4.12), the straight lines to semi-analytic theory Eq. (4.7) and the dash lines to the analytic approach Eq. (4.9a).

4.4.3 Comparison between the different approaches

The first remarkable feature of the rectified current is the fact that it is pumped between the two right electrodes. The dc current in electrode L↑ vanishes even though the ac voltage is applied there. Figure 4.4 shows the rectified current Eq. (4.9a) as a function of the drive frequency and amplitude.

The dc current follows damped oscillations with both V_0 and ω with frequency h/τ in the $\sim 10\,$GHz range. In particular, the characteristic time τ can be extracted directly from the minima of the dc current as a function of ω. Fig. 4.7 shows the plot of current $\bar{I}_{\uparrow}$ versus frequency ω for three different values of V_0, corresponding to cuts in Fig. 4.4 (green lines). Fig. 4.7 contains the results of three different calculations: the ideal analytical calculation Eq. (4.9a), the time-dependent simulations of the microscopic model Eq. (4.12) and a semi-analytical calculation that uses the time-independent part of the microscopic model and computes the rectification properties using Eq. (4.7). We find that a close agreement between the three approaches with a very accurate

agreement between the latter two. Departure from the ideal analytic formula (4.9a) arises due to the presence of a small backscattering in the device (which is not perfectly adiabatic) and the fact that the linear relation Eq. (4.3) is not strictly valid in the microscopic model (presence of the other characteristic scales).

We conclude that the ideal analytical model Eq. (4.9a) describes the physics qualitatively but cannot be used for quantitative predictions. On the other hand, Eq. (4.7) is computationally affordable and in precise agreement with the direct integration of the Schrödinger equation. It may be used for other - more realistic - models, which we shall do in the next section.

4.5 Realistic microscopic model

The two models studied above are of course idealized. Below, we develop a much more refined model which builds upon our previous work [4]. The model of Ref. [4] was shown to be in remarkable agreement with the dc experimental data even though the electrostatic potential was modeled rather crudely. Here, we extend the modelization and perform a self-consistent treatment of the electrostatic-quantum problem. We also include finite temperature thermal smearing ($\sim 20\,\mathrm{mK}$).

Before describing the specifics of the "realistic model", let us briefly discuss some orders of magnitude. The typical value of the difference of the time of flight τ that can be reached experimentally depends on the product of three factors, $\tau = \mathcal{L}\,(1/v_S - 1/v_A) \approx \mathcal{L}/v_S \times (k_S - k_A)/k_S \approx (\mathcal{L}/v_S)(k_S - k_A)/k_S \approx \mathcal{L}/v_S((k_S - k_A)/k_S) \approx ((k_S - k_A)/k_S)\mathcal{L}/v_S \approx \frac{k_S - k_A}{k_S}\mathcal{L}/v_S$. The longitudinal velocity v_S can be estimated from the experimental results of Ref. [67] to be $v_S \approx 2$ - $5\,(10^5 \mathrm{m\,s^{-1}})$. Typical values of $k_S - k_A$ found in Ref. [4] lie between 1% and up to 10% of the Fermi momentum k_S. The length $\mathcal{L}$ of the tunneling region in Ref. [4] was $\mathcal{L} = 1\,\mu\mathrm{m}$ but coherent oscillations have since been observed in much longer samples [69] $\mathcal{L} \approx 40\,\mu\mathrm{m}$ indicating that the low temperature ($\approx 20\,\mathrm{mK}$) phase coherence length in these samples is of a few tens of μm, comparable to what has been observed in the quantum Hall regime [46]. Altogether, we estimate $\tau \sim 100\,\mathrm{ps}$ for the slowest mode of a $20\,\mu\mathrm{m}$ long sample, which is consistent with what is found below in the simulations of the realistic model.

4.5.1 Geometry

The model is defined solely by the position of the top gates that are deposited on the surface of the GaAs heterostructure. It consists of a central region (defined by two lateral gates and a central tunneling gate) which smoothly evolves into two disconnected wires on the left and on the right of the central region. A top view of the layout of the

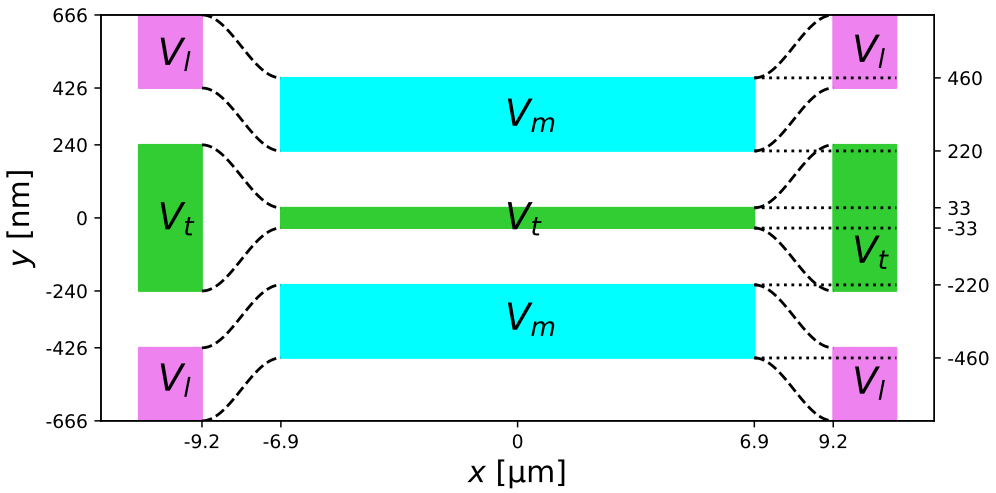

Figure 4.8: Top view of the layout of the gates that define the "realistic microscopic model".

gates is shown in Fig. 4.8. A cut at $x = 0$ (left panel) and $x > 10\,\mu$m (right panel) is shown in the upper panel of Fig. 4.9.

The dimensions of the device (with a central region 13.8 μm long and 0.92 μm large) are fully compatible with standard e-beam lithography techniques. The different gates are grouped into three categories: the three interior gates (green) are set to the same potential V_t, the two outer gates of the central region are set to V_m and the four outer gates of the electrodes are set to V_l. The transition region between the central region and the lead ($x \in [-9.2, -6.9]$ and $x \in [6.9, 9.2]$ μm) is defined by an interpolation described later in this section.

4.5.2 Self-consistent electrostatic potential

In order to calculate the electrostatic potential seen by the two-dimensional electron gas, we work in the effective mass ($m^* = 0.067\,m_e$, m_e: bare electron mass) approximation for the Schrödinger equation which is solved self-consistently with Poisson equation. The Hamiltonian of the two-dimensional electron gas,

$$H = \frac{P_x^2 + P_y^2}{2m^*} - eV(x, y, z = 0), \tag{4.14}$$

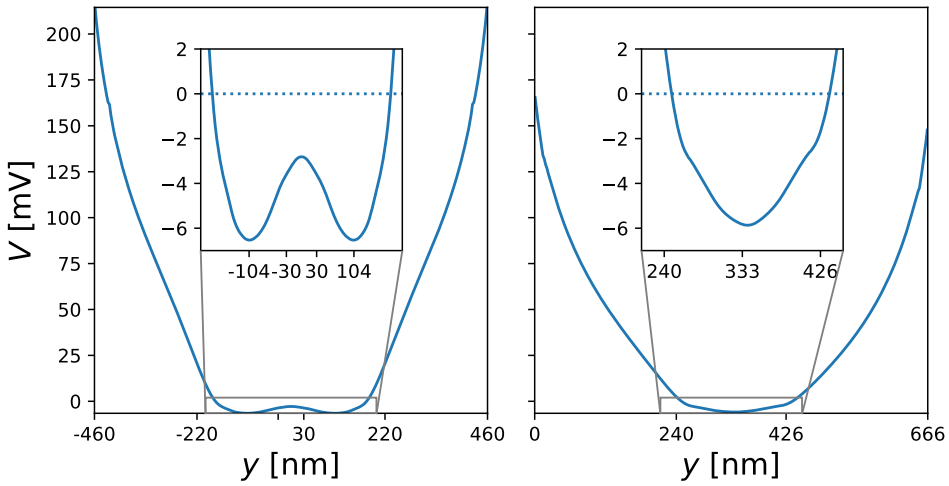

Figure 4.9: Upper panels: side view of the "realistic microscopic model" layout. Lower panels: self-consistent electrostatic potential seen by the electrons as a function of the transverse direction y. The insets show a zoom close to the Fermi level $E_F = 0$. Left panels: cut inside the central region ($x = 0$). Right panels: cut inside the leads ($x > 10\,\mu$m or $x < 10\,\mu$m)

is discretized on a square grid with lattice constant $a = 3\,$nm (approximately $2{\times}10^6 \approx 300 \times 6000$ sites). The Schrödinger equation

$$H\Psi_{\alpha E} = E\Psi_{\alpha E}, \tag{4.15}$$

is solved using the Kwant package [24]. The electrodes are taken to be semi-infinite so that the spectrum is actually continuous and the eigenfunctions labeled by an energy E and a mode index α. The density of electrons $n(x, y)$ is given by the integral over energy of the local density of states,

$$n(x, y) = \sum_\alpha \int \frac{dE}{2\pi} |\Psi_{\alpha E}(x, y)|^2 f(E), \tag{4.16}$$

where $f(E) = 1/(e^{E/k_B T} + 1)$ is the Fermi function at temperature T (and we have set the Fermi energy $E_F = 0$ as our reference energy point). The Poisson equation away from the electron gas reads

$$\Delta V(x, y, z) = 0, \tag{4.17}$$

while close to the gas the discontinuity of the electric field is set by $n(x, y)$:

$$\partial_z V(x, y, 0^+) - \partial_z V(x, y, 0^-) = -\frac{e}{\epsilon}[n(x, y) + n_d], \tag{4.18}$$

where the dopant density n_d sets the actual density of the gas and $\epsilon \approx 12\epsilon_0$ is the dielectric constant. The Poisson equation is solved using the FEniCS package [70].

In order to solve the set of self-consistent equations (4.15, 4.16, 4.17, 4.18), we perform one approximation which considerably lowers the computational effort while retaining good accuracy. In a first step, we solve the self-consistent problem deep in the lead region where the system is invariant by translation along x (hence effectively maps onto a 2D problem for the Poisson equation and 1D for the quantum problem). We obtain $V(|x| \gg 10, y, 0) \equiv V_A(y)$. Secondly, we solve the problem deep inside the central region, assuming that the potential is not affected by the leads (hence also invariant by translation along x). We obtain $V(|x| \ll 10, y, 0) \equiv V_B(y)$. An example of the obtained self-consistent potentials $V_B(y)$ (left) and $V_A(y)$ (right) is shown in Fig. 4.9 for $V_t = -0.43\,\mathrm{V}$, $V_m = -0.495\,\mathrm{V}$ and $V_l = -0.45\,\mathrm{V}$. In the last step, we describe the potential in the transition regions ($x \in [-9.2, -6.9]$ and $x \in [6.9, 9.2]$) by performing an interpolation between $V_A(y)$ and $V_B(y)$. The figure 4.10 shows the interpolated

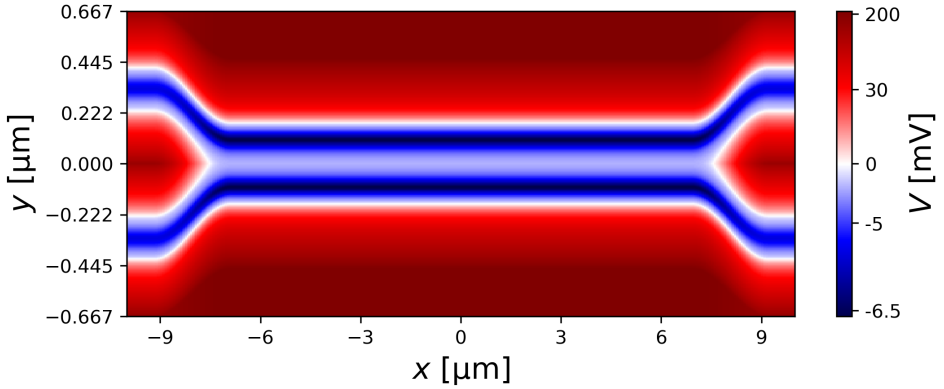

Figure 4.10: Interpolated potential 2D obtained from the extrapolation of the potential 1D at $x = 0$ and $x = \pm\infty$. The color gives us a logarithmic progression to represent the different scales involved from $\propto 100\,\mathrm{nV}$ in the middle to $\propto 100\,\mathrm{mV}$ at the border. The white color corresponds to the Fermi level $E_F = 0$.

potential. From $x > -6.9\,\mu\mathrm{m}$ to $x < 6.9\,\mu\mathrm{m}$ the potential of the central region is used. For $x < 9.2\,\mu\mathrm{m}$ and $x > 9.2\,\mu\mathrm{m}$ the potential of lead is used in the $y > 0$ region and its symmetry is used for $y < 0$. In between, a simple linear interpolation is not suitable due to the large scale of the potential involved, physics applies mainly in the region $V = -6.5$ to 0,mV when most of the potential values are around 200 mV. The interpolated potential is obtained by a weighted sum between the potential of the leads and the potential of the central region. In addition, the potentials are shifted along the

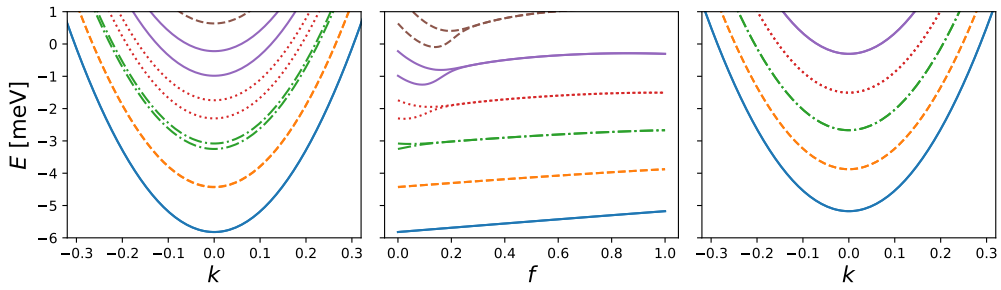

Figure 4.11: In the left panel is the dispersion of the energies of the bands according to their momentum in the central region. The bands are grouped in successive pairs. In the right panel are the energies according to momentum in a pair of lead, all bands are degenerated. In the central panel, the energy at zero momentum according to the interpolation parameter f. The degeneration of the bands is gently suppressed when the interpolation parameters move from the leadss ($f = 1$) to the central region ($f = 0$).

y-axis to match their minima before the weighted sum. We can verify that the potential is gently interpolated by examining the energy-momentum relationship of each step of the interpolation. Fig. 4.11 represents the bands of the central region on the left panel and the bands of the two conductors on the right panel. In the central panel appears the energy of the momentum bands k for different values of the interpolation parameter $f \in [0, 1]$, the energy connects doubly between the leads $f = 1$ and the central region $f = 0$.

The density of the gas is $\sim 3.2 \sim 3.2 \sim 3.2 \times 10^{11}\,\mathrm{cm}^{-2}$ which corresponds to a Fermi wavelength of $\lambda_F \approx 45\,\mathrm{nm}$. Since the transition region is long compared to λ_F, the transition is adiabatic and we observe a very low probability of reflection. We also need to verify that the modes from $L_\uparrow$ are fully transmitted in $R_\uparrow$ and $R_\downarrow$ modes and the absence of leak into $L_\downarrow$. Otherwise, Fabry-Perot interferences appear between the two lead-centrale region transitions, and distrube Mach-Zehnder interferometry. A smooth transition of potential prevent Fabry-Perot interferences. Finally, we verify that the superposition of $L_\uparrow$ and $L_\downarrow$ is transmitted in at most two modes in the central region. During propagation in the central region, a decomposition with three or more modes explores a larger phase space than the phase space of the pair of lead. In this case, part of the pulse is reflected at the lead-centrale interface, also creating unwanted Fabry-Perot interference.

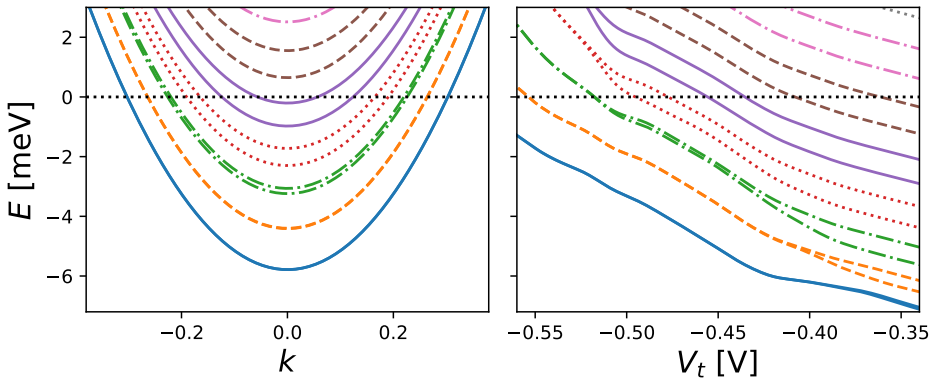

Figure 4.12: Structure of the subbands in the central region. Left panel: Energy dispersion $E(k)$ versus k for $V_t = -0.43\,\mathrm{V}$. The bands that cross the Fermi energy $E = E_F = 0$ correspond to propagating channels. Right panel: Transverse energies $E(k = 0)$ of the different modes as a function of the tunneling voltage V_t. The bands below the Fermi energy are propagating. Parameters: $V_m = -0.495\,\mathrm{V}$ and $V_l = -0.45\,\mathrm{V}$ for both panels. Symmetric/Antisymmetric modes pairs are plotted with similar color and line style.

4.5.3 Dc and ac characterization

Once the electrostatic potential is known, we calculate the transmission probabilities for the various conducting channels. We have used $V_t = -0.43\,\mathrm{V}$, $V_l = -0.45\,\mathrm{V}$ and $V_m = -0.495\,\mathrm{V}$ so that five propagating channels are open in each lead, and ten channels are open in the central region (a typical experimental situation). The left panel of Fig. 4.12 shows an example of band structure of the central region where we have used matching colors to identify the symmetric/antisymmetric pairs. The right panel of Fig. 4.12 shows $E(k = 0)$ for the various modes which allows one to identify the propagating channels ($E(k = 0) < 0$) and evaluate the splitting between the symmetric and antisymmetric components. Fig. 4.13 shows the dc conductance (at zero temperature) as a function of the tunneling voltage V_t (lower panel) obtained with Kwant [24]. The upper panel shows the contributions from the different propagating channels. The strongest oscillating signal is obtained close to the onset of the opening of a new channel where the difference between the momenta of symmetric and anti-symmetric channels is the highest.

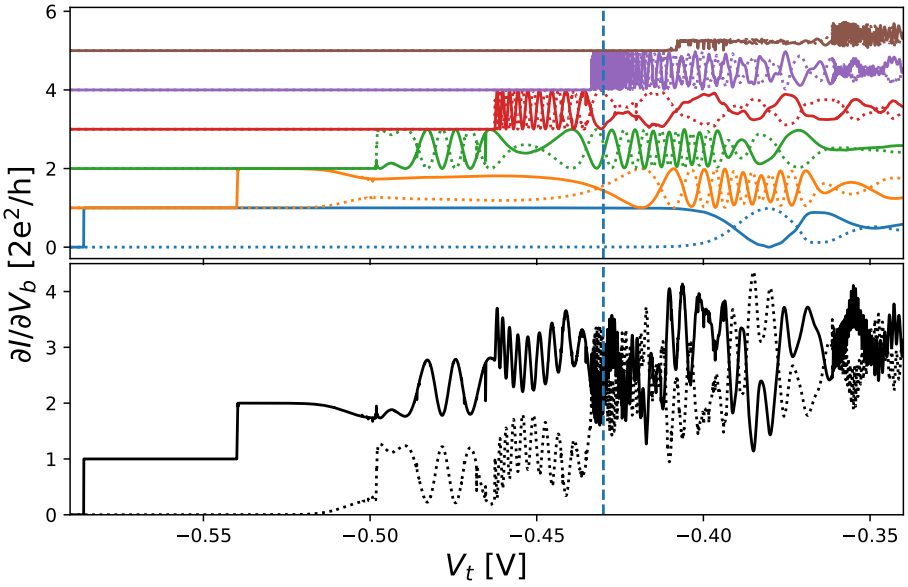

Figure 4.13: Lower panel: dc differential conductance $\partial I/\partial V_b$ as a function of the central gate voltage V_t for $V_l = -0.45\,\mathrm{V}$ and $V_m = -0.495\,\mathrm{V}$. The voltage bias V_b is applied to the upper left contact $L_\uparrow$ while the other three are grounded. The current is measured in the upper right contact $R_\uparrow$ (full lines, $\partial I_\uparrow/\partial V_b$) and in the lower right contact $R_\downarrow$ (dashed line, $\partial I_\downarrow/\partial V_b$). Upper panel: contribution from the individual propagating channels, shifted by multiples of $2e^2/h$ for clarity. Calculations performed at zero temperature

4.5.4 Rectification spectroscopy

The total number of orbitals is now rather large ($\sim 2 \times 10^6$) so that a direct time-dependent calculation is prohibitive. But discussion of section 4.4.3 shows that we can use Eq. 4.7 and get the same results with much less computational time. In order to obtain the rectification current one requires the calculation of the total transmission probability

$$D_{ab}(E) = \sum_{\alpha\in a,\beta\in b} |d_{\alpha\beta}(E)|^2, \tag{4.19}$$

where the sum is taken onto all the propagating channel of the corresponding electrode. An example of such a calculation using Kwant [24] is shown in Fig. 4.14 together with the detailed contributions of the different channels.

The effect of the temperature is taken into account in the integral of Eq. 4.7. The integrate is a convolution of two functions. First is the differential conductance $|d_{ba}(E)|^2$

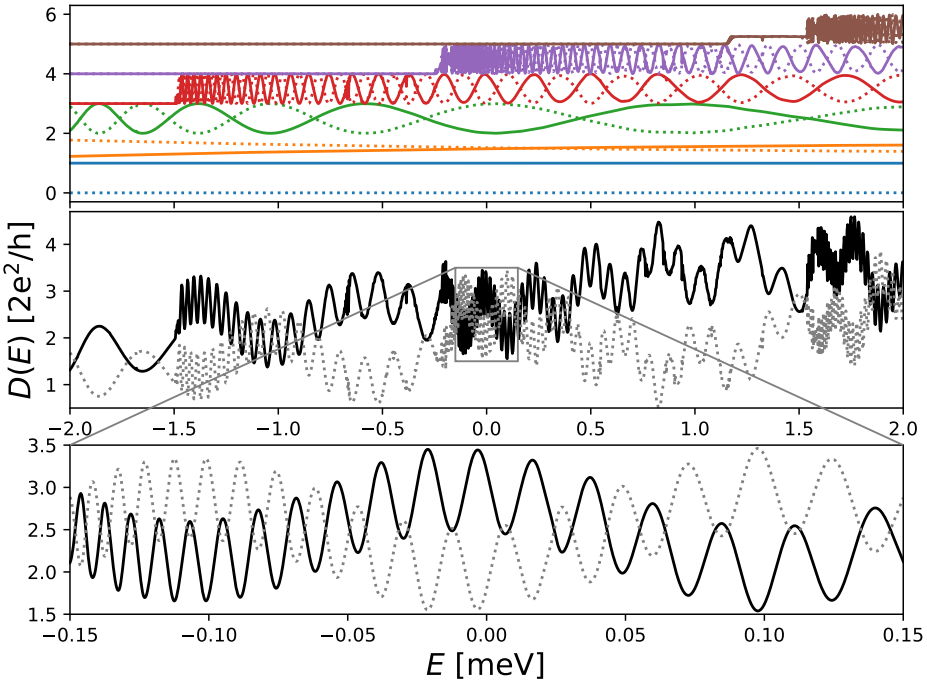

Figure 4.14: Middle panel: Total transmission probability $D(E)$, [full lines, $D_{\uparrow\uparrow}(E)$, dashed line, $D_{\uparrow\downarrow}(E)$] vs. energy E , where E is measured relatively to the Fermi energy E_F. Upper panel: contribution from the individual propagating channels, shifted by multiples of $2e^2/h$ for clarity. Lower Panel: zoom of the middle panel. Parameters: $V_t = -0.43\,\mathrm{V}$, $V_l = -0.45\,\mathrm{V}$ and $V_m = -0.495\,\mathrm{V}$ for all panels.

which oscillates around the Fermi energy with a period in energy $\sim \hbar/\tau$ for each mode. An example is shown at the bottom panel of Fig. 4.14. The second part is a difference of Fermi function $f_a(E + n\hbar\omega) - f_a(E)$, at zero frequency this function has a finite width of $k_B T$. The feature of the conductance start to disappear when the $T \gtrsim \hbar/(\tau k_B)$, with the slowest mode $\tau = 220\,\mathrm{ps}$ this gives $T \gtrsim 35\,\mathrm{mK}$. The following calculation has been performed at 20 mK to avoid thermal broadening.

The resulting rectified current for the realistic model is Fig. 4.15. Fig. 4.15 is qualitatively similar to the idealized model despite the fact that it includes a realistic modeling of the electrostatic potential, multiple opened channel (5) and a finite temperature (20 mK). This is a strong indication of the robustness of this type of spectroscopy.

An important aspect of the multi-channel model is that different channels (with different scales τ) contribute to the rectified current with contributions of order $1/\tau$ so

that the fastest channels have larger contributions. However, this does not prevent one from observing the slowest channels since the scales at which the different contributions vary is also very different [as can be inferred by an inspection of Eq. 4.9a]. In order to bring the different contributions to the same scale, it can be advantageous to plot the derivative of the current $\partial\bar{I}/\partial V_0$ instead of the current itself. This is typically performed experimentally using a lock-in technique. The signal can be furthered amplified by plotting the anti-symmetric signal $\partial\bar{I}_\uparrow/\partial V_0 - \partial\bar{I}_\downarrow/\partial V_0$ with respect to the two outputs in order to subtract any spurious signal coming from other rectification processes. Indeed, the multi-channel realistic model contains another source of rectification current coming from the opening of new channels which give rise to plateaus in the rectification current. These plateaus are very conveniently subtracted by looking at the anti-symmetric signal $\partial\bar{I}_\uparrow/\partial V_0 - \partial\bar{I}_\downarrow/\partial V_0$.

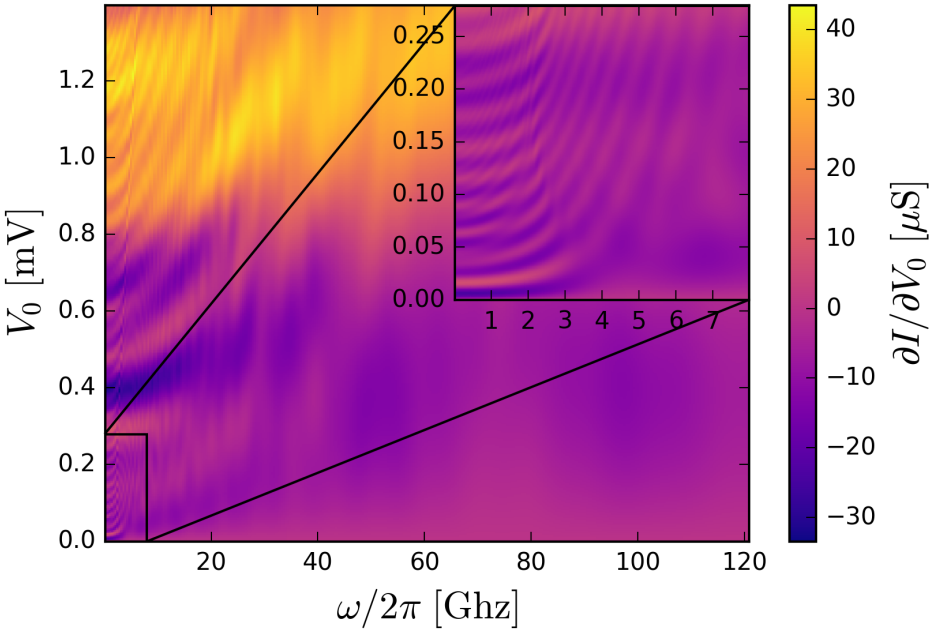

Figure 4.15: Realistic microscopic model. Colormap of $\partial\bar{I}_\uparrow/\partial V_0 - \partial\bar{I}_\downarrow/\partial V_0$ versus voltage amplitude V_0 and frequency $\omega/2\pi$. The inset shows a zoom of the main panel. Two channels with $\tau = 220$ps (oscillations visible in the inset) and $\tau = 19$ps (oscillations visible in the main panel) dominate the signal. Calculations performed at 20 mK.

The data of Fig. 4.15 corresponds to 5 pairs of propagating channels with respectively $\tau = 220\,\text{ps}$, $19\,\text{ps}$, $\tau = 3\,\text{ps}$ and two very fast channels with $\tau \ll 1\,\text{ps}$. With current experimental capabilities, the two interesting pairs that may be used for flying qubits

are the two slowest $\tau = 220\,\text{ps}$ and $19\,\text{ps}$. It is interesting that despite the presence of the three faster pairs, the spectroscopy lines of these two pairs are clearly visible in Fig. 4.15: at these scales, the three fast pairs only contribute to a global background. The two characteristic times $\tau = 220\,\text{ps}$ and $19\,\text{ps}$ can be directly extracted by fitting the low frequency (< 10 GHz) and large frequency (< 100GHz) part of the diagram.

4.6 Discussion and conclusion

The experimental observation of the features shown in Fig. 4.15 would provide the first direct measure of the characteristic times of the device and validate the possibility for the dynamical probing of an interference pattern at high frequency. This is a key step on the route toward further quantum manipulation with voltage pulses and the first full fledged electronic flying qubit [42].

Another important aspect which is at stakes is our ability to make accurate models, and predictive simulations, for high frequency quantum transport. At the experimental level, the electrostatic gates are controlled with voltages of the order of 1 V while the equilibrium electrostatic potential seen by the electrons is of the order of several mV, i.e. 2-3 orders of magnitude smaller (see e.g. Fig. 4.9). Hence, the construction of accurate models must go through a precise understanding of the combined electrostatic-quantum problem in the presence of high frequency dynamics. Conversely, the physics of these systems depends on the precise interplay between these two physics. Being in position to make quantitative predictions for these systems would allow one to design much more optimum geometries and experimental protocols; it would have a decisive impact in the development of the field. This article presents a step in this direction.

Our understanding of high frequency quantum transport, pulse propagation and dynamical interferometry (the ingredients of electronic flying qubit architectures) is mostly based so far on non-interacting models. As the experiments progress toward the exploration of this new physics, the modeling will require new aspects to be treated more accurately. Future work shall include a proper treatment of the electron-electron interactions at the RPA level [37] and beyond as well as a the modelisation of the different channels for decoherence. Indeed, understanding what sets the fundamental limit of coherence in these systems will probably be one of the most interesting challenge of the field in the years to come.

Chapter 5

Josephson junctions in electronic circuits

There is currently a huge effort around the world - both within academia and major industrial partners - to promote the superconducting transmon quantum bit [20; 71; 72] from a laboratory object to a viable technology for building a quantum computer. The central element of this approach is a weak normal link between two pieces of superconductors, the Josephson junction. Although tunneling junctions with an insulating (oxide) barrier are the most mature elements, other types of junctions such as atomic contacts [73] (with very few propagating channels), semiconducting nanowires [74] (with high spin-orbit suitable for stabilizing Majorana bound states) superconducting-ferromagnetic-superconducting [75; 76] (with anomalous current phase relations) or multiterminal devices [77] could provide new functionalities to the superconducting toolbox. While the theoretical description of these objects is rather well understood [78], many relevant regimes lie outside of what may be treated analytically and the development of numerical methods is important. In fact, the complexity of the circuits that are being created is increasing very rapidly and building predictive numerical tools is a key element for the success of any quantum technology.

5.1 Introduction to Superconductivity

Superconductivity is a central element of Josephson junctions. To perform numerical calculations, it is important to understand and model superconductivity correctly. Although superconductivity was discovered a long time ago, the first description dates back to Heike Kamerlingh Onnes in 1911, a correct mathematical interpretation of the phenomenon took a long time. It was only explained by the Bardeen-Cooper-Schrieffer

(BCS) theory in 1957 [79].

The starting point of the BCS theory is to consider electrons within an attractive potential. An attractive potential between electrons can be surprising, the direct interaction of Coulomb between negatively charged electrons can only produce a repellent potential. Inside the condensed matter, there are electrons but also atoms with a positive charge. An electron moving inside matter creates a lattice deformation called a phonon. Phonons induce a potential perceived by other nearby electrons. We consider an effective model of attractive potential, the details of the mechanism are not the purpose of this document. The Hamiltonian of the model correspond to free electrons with an attractive local electron-electron interaction between the opposite spin,

$$\hat{H} = \int d\mathbf{r} \sum_{\sigma} \hat{c}^{\dagger}_{\sigma}(\mathbf{r}) \frac{-\nabla^2}{2m*} \hat{c}_{\sigma}(\mathbf{r}) - V(\mathbf{r}) \hat{c}^{\dagger}_{\uparrow}(\mathbf{r}) \hat{c}_{\uparrow}(\mathbf{r}) \hat{c}^{\dagger}_{\downarrow}(\mathbf{r}) \hat{c}_{\downarrow}(\mathbf{r}), \tag{5.1}$$

where $\mathbf{r}$ is the coordinate vector and $\hat{c}^{\dagger}_{\sigma}(\mathbf{r})$, $\hat{c}_{\sigma}(\mathbf{r})$ are the spin electron creation - annihilation operators σ in position $\mathbf{r}$. The attractive potential is a fourth-order term in the creation - annihilation operator, it is too complex to solve directly. A mean field approximation is used to describe the problem with an effective quadratic Hamiltonian. Applying this approximation gives a quadratic Hamiltonian [80]

$$\begin{aligned} \hat{H} = \int d\mathbf{r} \sum_{\sigma} & \left[\hat{c}^{\dagger}_{\sigma}(\mathbf{r}) \frac{-\nabla^2}{2m*} \hat{c}_{\sigma}(\mathbf{r}) + U(\mathbf{r}) \hat{c}^{\dagger}_{\sigma}(\mathbf{r}) \hat{c}^{\dagger}_{\sigma}(\mathbf{r}) \right] \\ & - \Delta(\mathbf{r}) \hat{c}^{\dagger}_{\uparrow}(\mathbf{r}) \hat{c}^{\dagger}_{\downarrow}(\mathbf{r}) + \Delta^{*}(\mathbf{r}) \hat{c}_{\uparrow}(\mathbf{r}) \hat{c}_{\downarrow}(\mathbf{r}), \end{aligned} \tag{5.2}$$

where

$$\begin{aligned} U(\mathbf{r}) &= -V(\mathbf{r}) \left\langle \hat{c}^{\dagger}_{\uparrow}(\mathbf{r}) \hat{c}_{\uparrow}(\mathbf{r}) \right\rangle, \\ \Delta(\mathbf{r}) &= -V(\mathbf{r}) \left\langle \hat{c}_{\downarrow}(\mathbf{r}) \hat{c}_{\uparrow}(\mathbf{r}) \right\rangle. \end{aligned} \tag{5.3}$$

The parameters $U(\mathbf{r})$ and $\Delta(\mathbf{r})$ can be determined by autoconsistency of the model. We treat them as effective parameters by adjusting them to correspond to the experimental value. For simplicity's sake, the spatial dependencies of the parameter are neglected.

5.1.1 A numerical model of superconductivity

In order to simulate superconductivity, the Hamiltonian is transformed into a tight-bending model. We follow the methods developed in [2]. The space is discretized into small regions, called sites, labeled by the i index. Physical parameter are defined by a unique value on each site. The creation and annihilation operators with spin σ on the

i site are noted $\hat{c}^\dagger_{i\sigma}$ and $\hat{c}_{i\sigma}$. In continuous space, the derivative is given by the Newton difference quotient, the derivation in a direction x takes the form

$$\partial_x^2\psi(x) = \lim_{dx\to 0}\frac{1}{dx^2}\left[\psi(x+dx) - 2\psi(x) + \psi(x-dx)\right]. \tag{5.4}$$

The equivalent in the tight-binding model is obtained by using a, the distance between two sites, the smallest unit of space in the tight-binding model. This gives the approximation

$$\hat{\partial}_x^2 = \frac{1}{a^2}(\hat{c}_i^\dagger\hat{c}_{i+1} - 2\hat{c}_i^\dagger\hat{c}_{i+1} + \hat{c}_i^\dagger\hat{c}_{i-1}). \tag{5.5}$$

To simplify notation, we introduce the matrix $D_{ij} = \gamma(-2\delta_{ij} + \delta_{i,i+1} + \delta_{i,i-1})$ and the parameter $\gamma = \hbar^2/2am^*$. The tight binding version of Eq. 5.2 is

$$\hat{H} = \sum_{ij}\left[\sum_\sigma (D_{ij} - E_F\delta_{ij} + U\delta_{ij})\hat{c}^\dagger_{i\sigma}\hat{c}_{j\sigma} + \Delta_{ij}\hat{c}^\dagger_{i\uparrow}\hat{c}^\dagger_{j\downarrow} + \Delta^*_{ij}\hat{c}_{j\downarrow}\hat{c}_{i\uparrow}\right]. \tag{5.6}$$

where $\Delta_{ij} = \Delta\delta_{ij}$. To apply the wave function formalism of the chapter 3 to this Hamiltonian we need an explicit quadratic form $H = \sum_{ij}\hat{a}_i^\dagger H_{ij}\hat{a}_j$. The equation 5.6 does not make the quadratic nature of the Hamiltonian explicit because of the term in Δ. We use the Bogoliugov transformation, a new operator is defined by

$$\hat{\mathbf{c}}_i = \begin{pmatrix} \hat{c}_{i\uparrow} \\ \hat{c}^\dagger_{i\downarrow} \\ \hat{c}_{i\downarrow} \\ -\hat{c}^\dagger_{i\uparrow} \end{pmatrix}. \tag{5.7}$$

By using this operator, the Hamiltonian simplifies into

$$\hat{H} = \frac{1}{2}\sum_{ij}\hat{\mathbf{c}}_i^\dagger \begin{pmatrix} \mathrm{h}_{ij} & \Delta_{ij} & 0 & 0 \\ \Delta^*_{ij} & -\mathrm{h}_{ij} & 0 & 0 \\ 0 & 0 & \mathrm{h}_{ij} & \Delta_{ij} \\ 0 & 0 & \Delta^*_{ij} & -\mathrm{h}_{ij} \end{pmatrix}\hat{\mathbf{c}}_j, \tag{5.8}$$

where $\mathrm{h}_{ij} = D_{ij} + (U - E_F)\delta_{ij}$. According to Eq. 5.8 it is clear that the Hamiltonian is quadratic. The wave function corresponding to the operator 5.7 has four components,

$$\psi_{\alpha E} = \begin{pmatrix} \psi_{\alpha E\uparrow} \\ \psi^\dagger_{\alpha E\downarrow} \\ \psi_{\alpha E\downarrow} \\ -\psi^\dagger_{\alpha E\uparrow} \end{pmatrix}. \tag{5.9}$$

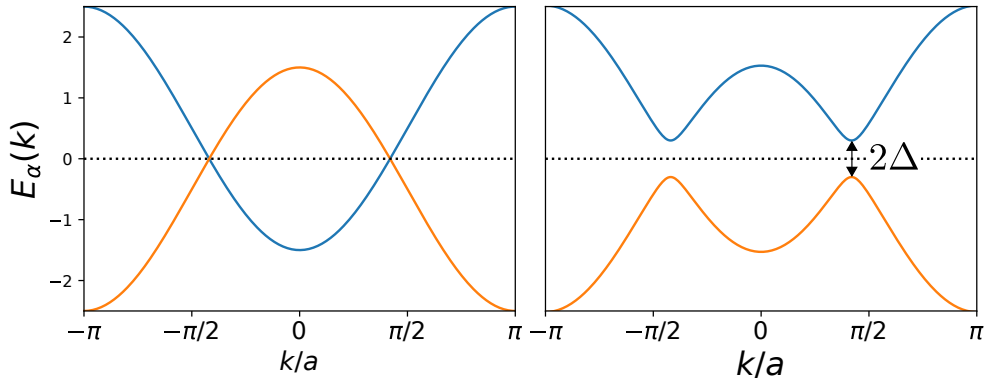

Figure 5.1: Band structure of a superconducting 1D chain. The reference of the Fermi level is set to $E_F = 0$. In the left panel, the dispersion relationship for a free electron (blue) and a hole (orange). In the right panel, the coupling terms in Δ open space around the Fermi level where no propagation mode is present.

Simulating the evolution of this wave function in dimensions N is equivalent to simulating a wave function in dimensions $N+1$ where one of the dimensions has a width of four sites. From the expression of Eq. 5.8 we notice that there are two independent sectors $(\psi_\uparrow, \psi_\downarrow^\dagger)$ and $(\psi_\downarrow, -\psi_\uparrow^\dagger)$. Hamiltonians in each subpart are identical, so the problem can be halved. The reduced Hamiltonian is given by

$$\hat{H}_{\text{eff}} = \frac{1}{2}\sum_{ij} \hat{c}_i^\dagger \begin{pmatrix} \mathrm{h}_{ij} & \Delta_{ij} \\ \Delta_{ij}^* & -\mathrm{h}_{ij} \end{pmatrix} \hat{c}_j. \tag{5.10}$$

5.1.2 Band structure

We are looking for the dispersion relational of our model. In the absence of superconductivity, the parameters Δ and U are equal to zero, but the Bogoliugov transformation of the Hamiltonian's is still valid. From the Hamiltonian 5.10 we extract two stationary equations, at each energy the solution are named u_E and v_E and obey

$$(H - E_F - E)u_E = 0, \tag{5.11a}$$
$$(H - E_F + E)v_E = 0. \tag{5.11b}$$

In the first equation, we recognize the equation for a free electron. The second equation corresponds to a negative energy particle with respect to the Fermi level, it can be identified as a hole. The corresponding bands are represented in the left panel, of Fig. 5.1, they are symmetrical with respect to the Fermi energy.

With the presence of the superconductivity ($\Delta \neq 0$) the two wave functions u_E and v_E are coupled. For each momenta k there are two solutions mixing electrons and holes, one of positive energy, another of negative energy. The two solutions are separated by gap in energy of 2Δ. The right panel of Fig. 5.1 shows an example of superconducting bands.

5.1.3 Andreev reflection

We consider the junction between a normal metal wire and a semi-infinite superconductor. In superconductors, there is no propagation mode in the gap defined by energies between $E_F - \Delta$ and $E_F + \Delta$. In the non-superconducting part mode at open at these energies. A metallic mode with energy inside the gap will be reflected at the interphase with the superconductor, this process is called Andreev's reflection. In the metallic part, the excitation of electrons and holes are independent (cf. Eq. 5.11b). An electron is reflected as a superposition of an outgoing electron and an outgoing hole. The scattering matrix of incoming electron/hole in outgoing electron/hole is obtained by matching the wave function [81], it is written

$$S_{e,h\to e,h} = \exp\left(-i \arccos\left(\frac{E}{\Delta_0}\right)\right) \begin{pmatrix} 0 & e^{i\varphi} \\ e^{-i\varphi} & 0 \end{pmatrix}, \tag{5.12}$$

where $\Delta = \Delta_0 e^{i\varphi}$. We notice that an electron is completely reflected in a hole, and that a hole is completely reflected in an electron. The conservation of the charge during the process implies that charges $2e^-$ is created or destroyed inside the superconductor, these are the Cooper pairs.

5.1.4 Superconducting phase

The phase of the superconducting parameter (φ) is an important parameters for the Andreev's reflection. To understand this phase, we study how its evolution. When a uniform voltage $V(t)$ is apply to a superconductor the Hamiltonian is given by the element

$$\hat{H}_{\text{eff},ij} = \begin{pmatrix} \mathrm{h}_{ij} + V\delta_{ij} & \Delta_{ij} \\ \Delta^*_{ij} & -\mathrm{h}_{ij} - V\delta_{ij} \end{pmatrix}. \tag{5.13}$$

To get rid of the voltage, we use a gauge transformation of the wave function

$$\tilde{\psi} = \begin{pmatrix} e^{i\varphi} & 0 \\ 0 & e^{-i\varphi} \end{pmatrix} \psi, \tag{5.14}$$

where $\varphi = \int^t V(t')dt'$ is the integral of the voltage. The time derivative of the new wave function is given by

$$i\partial_t\tilde{\psi} = \begin{pmatrix} \mathrm{h}_{ij} & \Delta_{ij}e^{2i\varphi} \\ \Delta^*_{ij}e^{-2i\varphi} & -\mathrm{h}_{ij} \end{pmatrix} \tilde{\psi}. \tag{5.15}$$

We get a Shrödinger equation with a Hamiltonian where the voltage has disappeared but the superconducting parameters are gaining a phase $e^{2i\varphi}$. We deduce the equation of motion for the superconducting phase

$$\partial_t\varphi = V. \tag{5.16}$$

5.2 The Josephson junction

5.2.1 Ac properties of Josephson junctions

A Josephson junction is an element consisting of two superconductors connected together by a non-superconductive material. Each superconductor is modeled by the superconductor parameters $\Delta_{1,2}$ and $U_{1,2}$. Here the two superconductors are considered to be of the same type, which implies equality between gaps $|\Delta_1| = |\Delta_2| = \Delta$ and potentials $U_1 = U_2$. Thus each superconductors are defined by theirs superconducting phase φ_1 and φ_2.

A junction is composed of two superconductor/normal interfaces face to face. Excitation with energy inside the gap cannot propagate into the superconductors and is trapped between the two interfaces. When a wave function loops on itself after a finite number of reflections, we obtain a bound state. The condition is satisfied when the phase accumulated by all reflections and propagations is a multiple of 2π. In the case where the propagation phase is negligible in front of the Andreev reflection phase, the condition for a bound state is

$$-\arccos(E/\Delta) + \frac{2E\tau_f}{\hbar} \pm (\varphi_1 - \varphi_2) = 2\pi n,\ n \in \mathbb{Z}. \tag{5.17}$$

This equation allows two solutions depending on the value of the phase difference $\varphi = \varphi_1 - \varphi_2$ between the two superconductors. The solutions have energies

$$E = \pm\Delta\sqrt{1 - T\sin^2(\varphi/2)}. \tag{5.18}$$

The energy-phase relationship is represented Fig 5.2 for a junction of transparency of $D = 0.5$. The energy depends on the phase difference φ and the phase difference

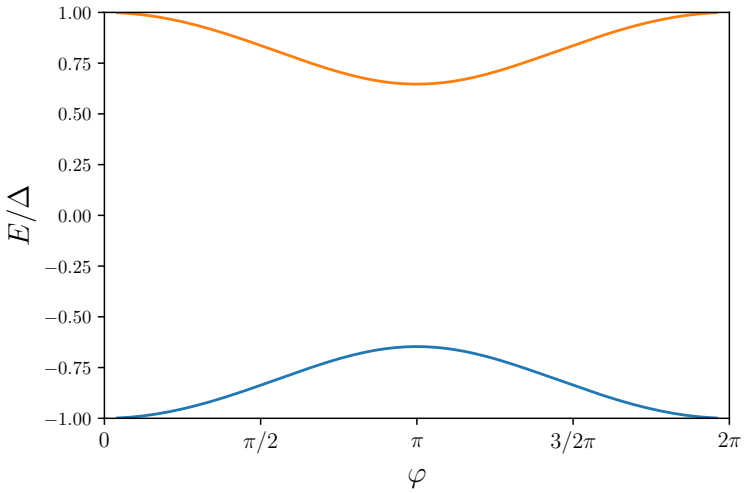

Figure 5.2: Energy phase ratio for a Josephson junction with transparency $D = 0.5$.

depends on the voltage difference between the junction $\partial_t \varphi = 2e(V_1 - V_2)/\hbar$. This implies that a constant voltage polarization induces a periodic variation in the bound state energy within the system as a function of time. This phenomenon is also visible if we look at the junction current given by $I = (2e/\hbar)\partial F/\partial\varphi$. Within the low transparency limit $D \ll 1$ the current reads

$$I = I_c \sin\varphi. \tag{5.19}$$

This is the famous sinusoidal current-phase relationship of a Josephson junction. Under a constant polarization voltage, the junction produces a periodic sinusoidal voltage. From the point of view of classical electronics, a Josephson junction is a highly non-linear component, which makes them very interesting. Within the limit of a small voltage variation $\varphi \ll 1$ the sinusoid can be linearized $I \sim I_c\varphi$. In this regime, the junction is equivalent to a linear inductance $\partial_t I = V/L$ with inductance $L = 1/I_c$.

5.2.2 Dc properties of Josephson junctions

We call quasiparticles the excitations mixing electron and holes inside superconductors. A current is created when a quasi-particulates tunnel through a junction. Because of Pauli exclusion principle, they can only move from an occupied state to an empty state. At low temperature, all the propagation states below the gap interval are occupied ($E < -\Delta$), and all propagation states above the gap ($E > \Delta$) are empty. A conduction process must bring a quasiparticle from below the gap to a state above the gap. The required energy is taken from the bias voltage of the junction. For a voltage above $eV > 2\Delta$, the electrons receive enough energy to jump directly across the gap. The

process depends on the bias voltage and the transparency of the junction D, the current reads

$$I \underset{V\to\infty}{=} DV. \tag{5.20}$$

For bias voltage below $eV < 2\Delta$ conduction channels are possible when quasiparticules accumulate energy after multiple Andreev reflection, gaining each time an energy $+eV$. The channel with n reflections is open when $neV > 2\Delta$, but it is also suppressed by a factor D^n. This process is called multiple Andreev reflexion (MAR).

5.2.3 Numerical model of Josephson junctions

We use the algorithm of chapter 3 to simulate a Josephson junction. The tight-binding model describes a one-dimensional along the x axis. We use a short junction where the two superconductors correspond to the region $x < 0$ and $x > 0$ while the normal region is formed by a single site at $x = 0$. The Hamiltonian is

$$\begin{aligned}\hat{H} = &\sum_{\substack{x=-\infty\\ \sigma=\uparrow,\downarrow}}^{+\infty} e^{i\varphi(t)\delta_{x,-1}}\hat{c}^\dagger_{x\sigma}\hat{c}_{x+1,\sigma} + (U\delta_{x,0} - E_F)\hat{c}^\dagger_{x\sigma}\hat{c}_{x\sigma} \\ &+ \sum_{x=-\infty}^{+\infty} \Delta(1-\delta_{x,0})\hat{c}^\dagger_{x\uparrow}\hat{c}^\dagger_{x\downarrow} + h.c.,\end{aligned} \tag{5.21}$$

where $\varphi(t) = (e/\hbar)\int^t V(t')dt'$, $V(t)$ is the voltage difference across the junction, Δ_0 is the superconducting gap inside the superconductors, U is an effective potential barrier used to regulate the transmission probability D of the junction. We used $\gamma = 1$, $E_F = 2$ and $\Delta = 0.1$ to be in the regime $\Delta \ll E_F$. The potential $U = 2$ is tuned to correspond to a junction with an intermediate transmission $D = 0.5$. We work at zero temperature.

The figure 5.3 shows Josephson junctions with three transparencies subjected to a voltage ramp. The dc component $\bar{I} = I_0$ and the first ac component I_1 of the current are extracted with moving average and Fourier transform. We recover all the expected feature. The current oscillate with a frequency $\omega = 2eV$. At high voltage the average current goes to the asymptote $I = DV$. The characteristics $\bar{I} - V$ relation of the insulated junction have distinct cusps at voltages $eV = \Delta/n$, $n \in \{1, 2, 3\dots\}$ corresponding to multiple Andreev reflexion. All the result are in accordance with the theorical result of [82] computed with wave function matching. The sinusoidal current phase relation $I(\varphi) = 2e\Delta T/h \sin(\varphi)$ is recovered in the tunneling regime $D \ll 1$ and $eV < \Delta$.

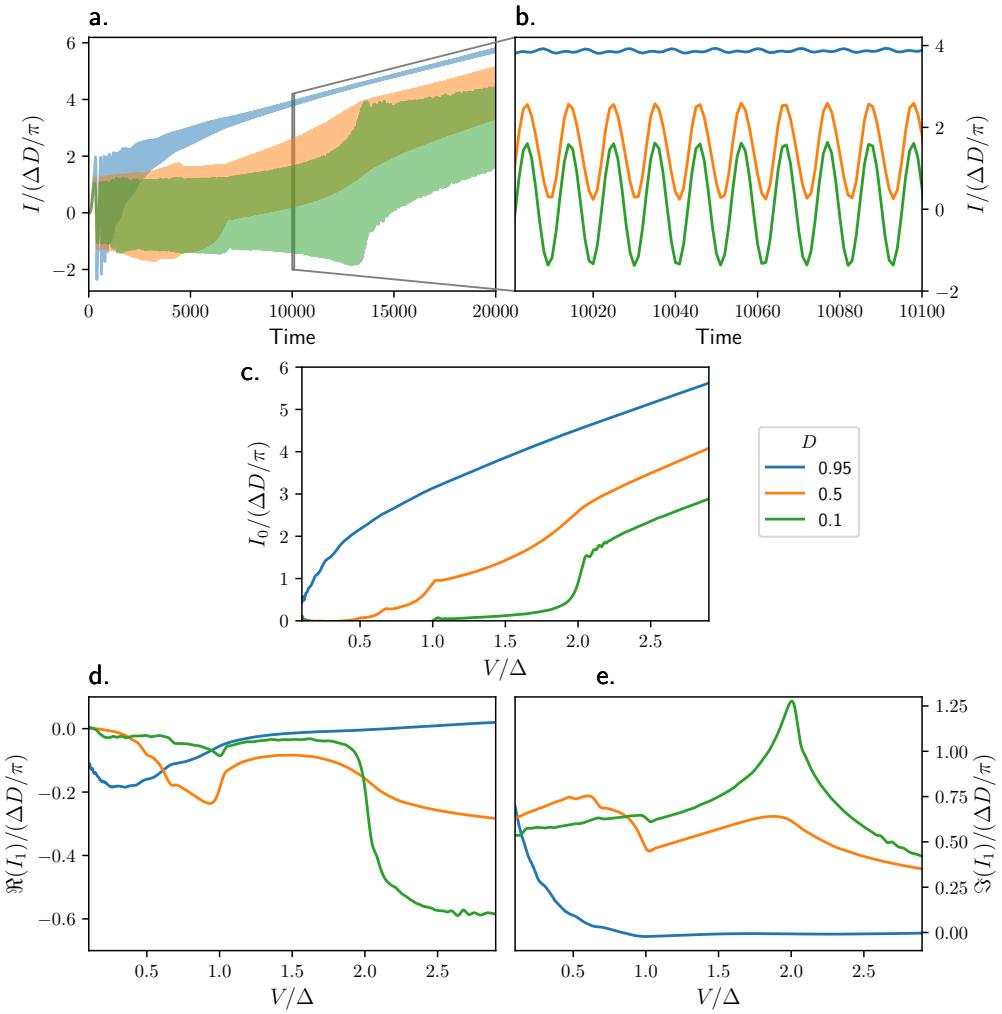

Figure 5.3: Simulations of Josephson junctions with three transparencies $D = 0.1,\ 0.5,\ 0.95$ and gap $\Delta = 0.2$ under a voltage ramp $eV = 0 - 3\Delta$. In the upper panels, the current as a function of time. In the middle panel, the average current as a function of voltage. At the bottom left and right, the real and imaginary part of the first harmonics of the current. All numbers are rescaled with $\Delta T/\pi$.

5.3 Simulation inside electronic environments

5.3.1 The RCJ model

Two very successful complementary viewpoints are commonly used to describe Josephson junctions circuits. The first one is the RCJ model [83; 84] (Resistor-Capacitor-Josephson) that views the Josephson junction as a highly non-linear impedance embedded in an electric circuit. In this model, one considers a classical circuit, such as the ones shown in the insets of Fig. 5.4 or Fig. 5.6 with resistances $V = RI$, capacitances $I = C\partial_t V$, inductances $V = L\partial_t I$ or other classical elements. The Josephson junction is described by its current-phase relation $I = I_c \sin\varphi$ and the Josephson relation $\partial_t \varphi = (2e/\hbar)V$. Such a simple model is surprisingly powerful. It captures the hysteresis loops of the $I - V$ curves. Its simple extension, where one adds a Langevin stochastic term to account for finite temperature, accurately describes the noise properties found experimentally, including the probability for the junction to switch from the superconducting branch [85]. It has also been successfully used for more elaborate circuits that include resonators [86]. Its quantum extension provides the model used to design the various sorts of superconducting qubits [87] and has been shown to describe a large corpus of experimental data accurately [88]. Yet, the model fails dramatically in some very simple limits. For instance, at large voltages, it does not properly reproduce the Ohmic behavior of the circuit, since the latter involves the excitation spectrum of the junction which is not accounted for in the current-phase relation. More importantly, it does not account for some important out-of-equilibrium phenomena such as Multiple Andreev Reflection [89; 82] (MAR) processes.

5.3.2 Results for the RC model

RCJ prediction

The first electromagnetic environment we consider is a simple RC circuit as sketched in Fig. 5.4. The capacitance C typically accounts for the electron-electron interaction in the junction itself while the resistance R accounts for the finite residual resistance in the whole circuit. This RC circuit is the minimum electromagnetic environment that must be considered. The RCJ model for this circuit (where the BdG equation is replaced by the current-phase relation) reads,

$$\frac{d^2\varphi}{dt^2} + \frac{1}{Q}\frac{d\varphi}{dt} + \sin(\varphi) = \frac{I_0}{I_c}, \tag{5.22}$$

where the time t has been rescaled as $t \to \omega_0 t$. $\omega_0 = \sqrt{\hbar I_c/(2eC)}$ is the intrinsic frequency of the circuit for small oscillating amplitudes and $Q = RC\omega_0$ is the corresponding quality factor. The physics of this model is well understood [84]: for $I_0 < I_c$ all the current passes through the junction (super-current branch) while for $I_0 > I_c$ the equilibrium solution is unstable and a voltage develops across the junction. Interestingly, this model is hysteretic for underdamped circuits $Q > 1$ and a dynamical solution with $\dot{\varphi} \neq 0$ exists for some values of $I_0 < I_c$. At high bias current $I_0 \gg I_c$, most of the current is dissipated by the resistor R and the RCJ model predicts $I_0 = R\bar{V}$ (where $\bar{V}$ is the average voltage difference seen by the junction. This prediction misses an important contribution from the junction, its intrinsic resistance $R_J = h/(2e^2 D)$ in the normal state. Indeed, at large bias current, one expects $I_0 = (1/R + 1/R_J)\bar{V}$

5.3.3 Time-dependent RCJ simulation

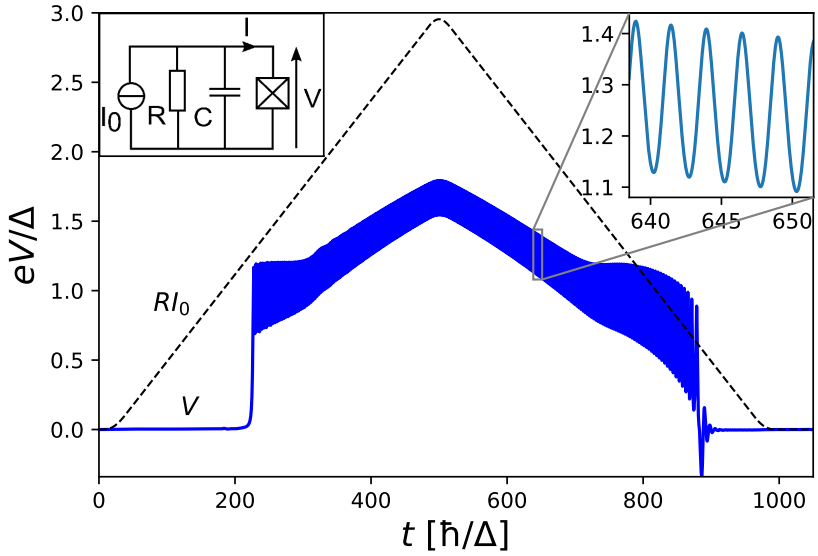

Figure 5.4: Upper left inset the simulated circuit, an RC biased Josephson junction. Main panel result of the RC-BdG simulation. Dashed line: voltage RI_0 applied by the generator versus time t. I_0 is raised and decreased slowly to keep the system quasi-adiabatic. Blue line: voltage $V(t)$ measured across the junction. Upper right inset: zoom of the main curve revealing the oscillations due to the ac Josephson effect.

We now turn to the full simulation of the RC circuit with a Junction model by the time-dependent BdG model (hereafter called RC-BdG model). The bare simulation data is shown in Fig. 5.4 where the dashed line corresponds to a slow (quasi-static)

ramp of I_0 so that the entire $I-V$ characteristics of the device can be extracted from a single simulation. We ramp the current first up and then down to zero in order to capture the hysteresis loop of the junction. The blue line corresponds to the voltage across the junction as a function of time. As shown in the inset, the blue line contains an important oscillating part that corresponds to the ac Josephson effect. From this data, we calculate the voltage $\bar{V}$ across the junction, averaged over a small time window (to get rid of the ac Josephson signal). Fig. 5.5 shows the resulting plot of I_0 versus $\bar{V}$ (blue line). The dotted line corresponds to the various asymptotic of the RCJ model discussed above while the dashed line corresponds to the pure BdG model in the absence of the electromagnetic environment. The pure BdG model displays the usual kinks characteristics of the opening of a new MAR channel [90]. The RC-BdG simulations reconcile the two limits: the pure MAR curve at high bias and the super-current branch of the RCJ model at small bias. In the crossover between these two extreme limits, it provides the minimum model that captures all important physical contributions, hence quantitatively predicts the full hysteresis loop including the retrapping current. The most interesting features of the system show up in its dynamics. Recording the phase difference $\varphi(t)$ across the junction and the current $I(t)$ that flows through it, the dynamics is properly captured by the corresponding out-of-equilibrium current phase $I-\varphi$ relation obtained from the corresponding parametric plot. the result is shown in the upper panel of Fig. 5.5. Such out-of-equilibrium $I-\varphi$ could be reconstructed from a high-frequency measurement of the different harmonics of $V(t)$. As a reference, Fig. 5.5 includes the equilibrium $I-\varphi$ characteristics of the junction (dotted line) obtained by taking all contributions into account (i.e. both Andreev bound states and the small contribution from the continuous part of the spectrum). This equilibrium $I-\varphi$ relation contains small deviations to the sinusoidal form. However, out-of-equilibrium relations can be strongly different from the simple sinusoidal shape. This is true in particular in the returning part of the hysteresis loop (red line, square, visible component of the second harmonic) and close to the MAR cusps (yellow line, triangle, strongly non-sinusoidal). In these regimes, the excursions in voltage across the junction are wide (as can be seen directly from Fig. 5.4) and the junction effectively highly non-linear. The full code used for generating the data of this article can be found in Ref. [91].

5.3.4 Results for the RLC model

RLC-Sinusoidal Junction

We now turn to a second circuit where the junction is put in series with a classical RLC resonator as sketched in the inset of Fig. 5.6. The electromagnetic circuit is slightly more complex than the previous RC model, but in return, the highly non-linear

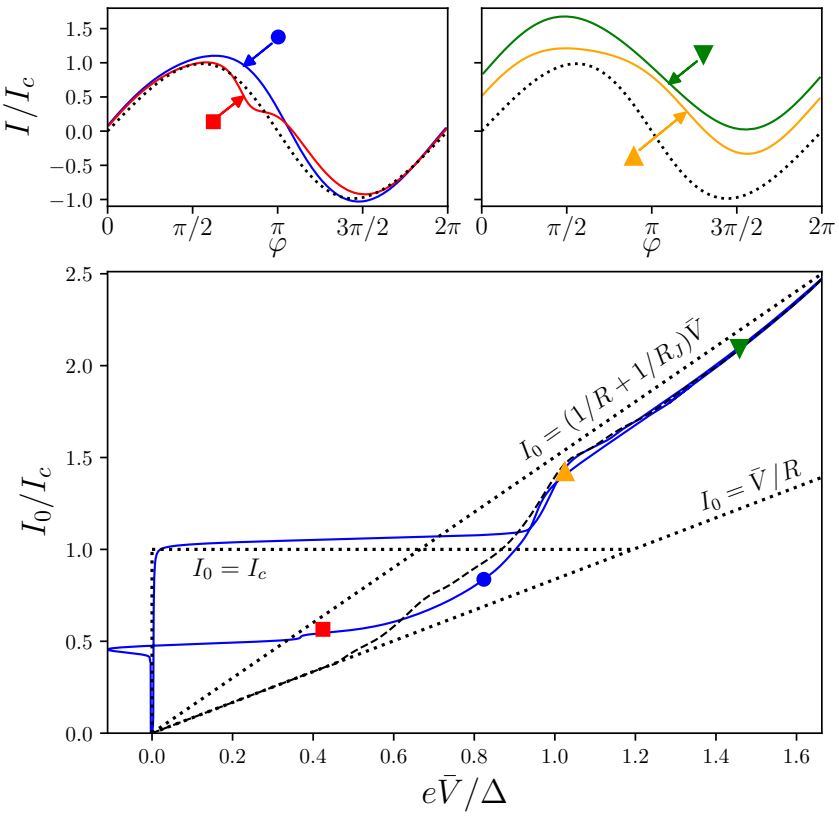

Figure 5.5: RC-BdG model. Bottom panel: bias current I_0 versus the average voltage across the junction $\bar{V}$ for an underdamped oscillator $Q \approx 1.7$. Dotted lines: various asymptotes of the RCJ model, see text. Dashed line: pure BdG model without the environment. Upper panels: out-of-equilibrium current-phase relations at 4 different points of the $I_0 - \bar{V}$ curve. The dotted line corresponds to the equilibrium current-phase relation of the pure junction.

behavior shown in the previous example manifests itself already on dc observables. The resonator has a quality factor $Q = R\sqrt{C/L}$ and a resonance pulsation $\omega_0 = 1/\sqrt{LC}$. The corresponding impedance $Z(\omega)$ takes the form $R/Z(\omega) = 1 + iQ[\omega/\omega_0 - \omega_0/\omega]$ and filters frequency around ω_0. Such an environment has been studied in a series of recent experiments using tunnel junctions [92; 93; 94; 95]. The RLC circuit provides

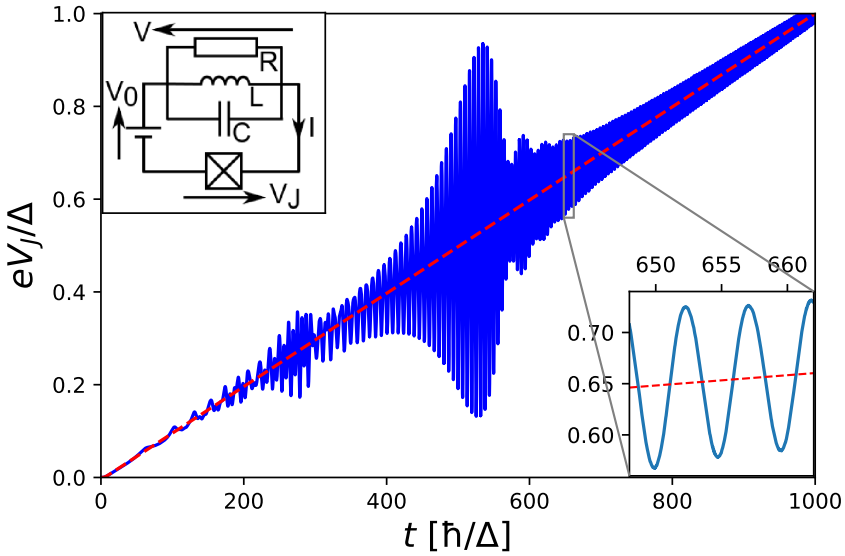

Figure 5.6: RLC-BdG model. Upper inset: schematic of the RLC circuit. Main panel: voltage $V_J(t)$ across the junction (blue line) versus time t for a linear voltage ramp in $V_0(t)$ (red dashed line). $Q = 20$, $\omega_0 = \Delta$ and $R = 3h/2e^2 \simeq 38.7\,\mathrm{k}\Omega$. Bottom inset: zoom of the main curve showing the ac Josephson effect oscillations. The resonance of the RLC circuit is visible for $eV_J = \hbar\omega_0/2$ and $eV_J = \hbar\omega_0/4$

a direct probe of the ac signal present in the system. We expect a main resonance for $2eV_J/\hbar = \omega_0$ when the ac Josephson effect drives the RLC circuit. Due to the non-linear character of the junction, higher harmonics of the ac Josephson effects are generated, so that additional features are expected at $2eV_J/\hbar = \omega_0/n$. Likewise, the non linearities imply that the RLC circuit can also be driven parametrically at $2\omega_0$ leading to features at $eV_J/\hbar = \omega_0/n$.

5.3.5 Time-dependent RLCJ simulation

We compare the RLC with a BdG Josephson junction calculations (named RLC-BdG) with an RLJ model with an effective Josephson junction (named RLCJ). The improved

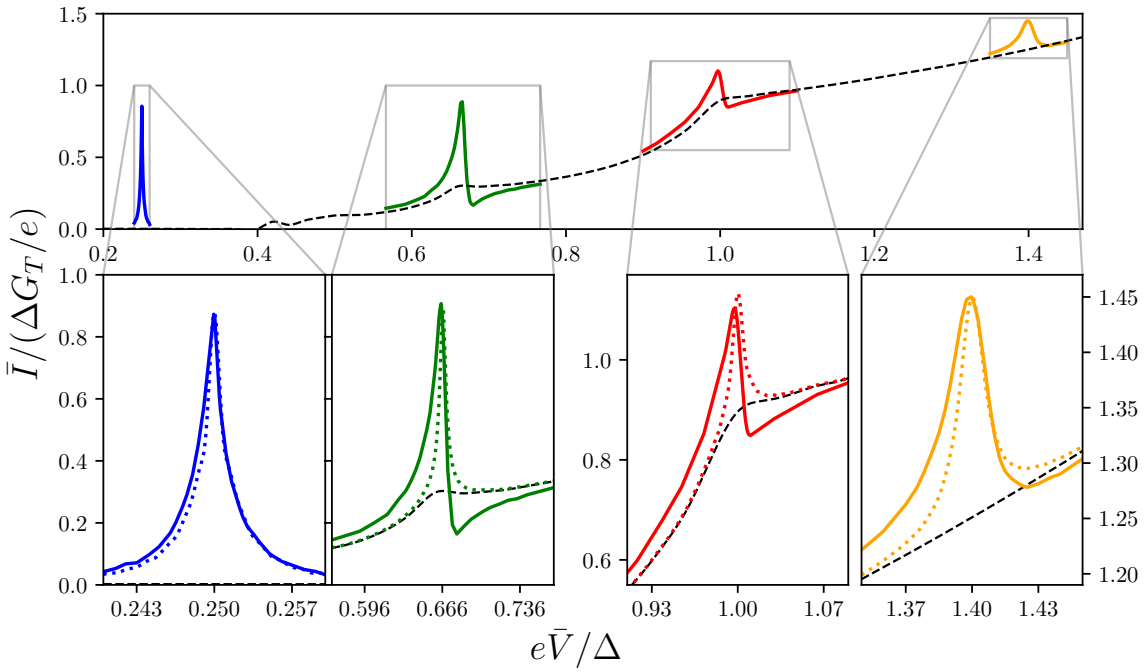

Figure 5.7: Current-voltage relation for four different resonator frequencies $\omega_0/\Delta = 1/4, 2/3, 1$ and 1.4. Dashed line: $I_{\rm MAR}(V)$ in the absence of environment, thin color lines: RLC-BdG simulations, dotted lines: improved RLCJ model. Bottom panels: zoom of the main figure.

RLCJ model captures the super-current branch and the MAR non-linear I-V curve as,

$$I(\varphi) = I_c \sin\varphi + I_{\rm MAR}(2e\dot{\varphi}/\hbar), \tag{5.23}$$

where $I_{\rm MAR}(V)$ is the dc non-linear $I-V$ characteristic of the junction in the absence of electromagnetic environment (dashed line of Fig. 5.7). The numerical results for the average current $\bar{I}$ versus voltage are shown in Fig. 5.7 for four different RLC circuits with different frequencies ω_0. We concentrate on the main features around $2eV_J/\hbar = \omega_0$ and disregard the smaller peaks associated with higher harmonics and/or parametric pumping. The improved RLCJ model (dotted line) presents a Lorentzian like resonance at $2eV_J/\hbar = \omega_0$ for all four RLC circuits. When the resonance lies in the tunneling regime of the junction (blue line), there is a very good agreement between the improved RLCJ model and the full RLC-BdG simulations. The agreement is also qualitatively (but not quantitatively) good when the resonance corresponds to high voltages in the almost "Ohmic" regime of the junction (yellow line). However, for the two circuits where the resonance lies in the vicinity of a kink of the $I_{\rm MAR}(V)$ characteristic, the

two models are strikingly different and the improved RLCJ model no longer applicable (green and red lines): the improved RLCJ model is typically off by ±50% including in the linewidth. In these regimes, we find that for $2eV_J/\hbar > \omega_0$, the current is *reduced* with respect to $I_{\mathrm{MAR}}(V)$ instead of the Lorentzian increase observed in the improved RLCJ model. This reduction of the current is a direct manifestation of the non-linear ac physics happening in the device. This dc prediction is the counterpart of the highly non-sinusoidal non-equilibrium current-phase relations discussed above for the RC-BdG case. However, the fact that the observable is in dc makes this prediction more easily accessible to an experimental test.

5.3.6 Short pulse excitation of Josephson junctions

In the article [25] the authors study the effect of a short voltage pulse on an isolated Josephson junction. The Fourier decomposition of a short pulse is spread in energy, the modes inside the Junction are equally exited at all energies by a short voltage pulse. Excited modes with energies above the gap escape into the superconductors. The modes under the superconducting gap are filled by the thermal bath from the superconductors. But the modes with energy inside the gap are isolated, they can't escape.

In the absence of other time-dependent perturbation after the pulse, the excitations are permanently trapped within the gap. One particularity of superconductors is that fundamental states contain current. If excitations within the gap are in a coherent superposition of a state with positive current and a state with negative current, the current of the junction oscillates over time with the quantum oscillation between the states. This phenomenon only applies to an isolated junction. In an electronic environment, the phase evolves according to the current produced by the junction itself. This allows the dissipation of energy inside the gap.

Short pulse excitation of an isolated junction

The model is a short junction with a tunnel barrier. A Gaussian voltage pulse is sent to the junction. The pulse is characterized by its width over time τ and by the total phase difference induced through the junction $\delta\varphi = \int^t V(t)dt$. Shortly after the impulse, the only remaining modes are within the interval. For the short junction, there are only two modes (named $|\psi_1\rangle$ and $|\psi_2\rangle$) inside the gap corresponding to the Andreev bound states with energies E_1 and E_2 given by Eq. 5.18. Each mode carries a current given by $I_1 = -I_2$. The state of the junction is represented by

$$|\psi\rangle = |\psi_1\rangle\, \alpha e^{-\frac{i}{\hbar}E_1 t} + |\psi_2\rangle\, \beta e^{-\frac{i}{\hbar}E_2 t}, \tag{5.24}$$

where α and β are the amplitudes of occupation of each mode. The junction current is given by the current operator

$$\langle \hat{I} \rangle = |\alpha|^2 \langle \psi_1 | \hat{I} | \psi_1 \rangle + |\beta|^2 \langle \psi_2 | \hat{I} | \psi_2 \rangle + 2\,\mathrm{Re}(e^{-\frac{i}{\hbar}(E_1 - E_2)t} \alpha\beta \langle \psi_1 | \hat{I} | \psi_2 \rangle). \tag{5.25}$$

In the case where only one mode is occupied ($\alpha = 0$ or $\beta = 0$) the current is given by the stationary component $\langle \psi_2 | \hat{I} | \psi_2 \rangle$ or $\langle \psi_1 | \hat{I} | \psi_1 \rangle$ respectively. When both modes are equally occupied $|\alpha| = |\beta|$ the dc component of the current disappears and only a sinusoidal current of frequency $(E_1 - E_2)/\hbar$ and amplitude $2|\langle \psi_1 | \hat{I} | \psi_2 \rangle|$ remains.

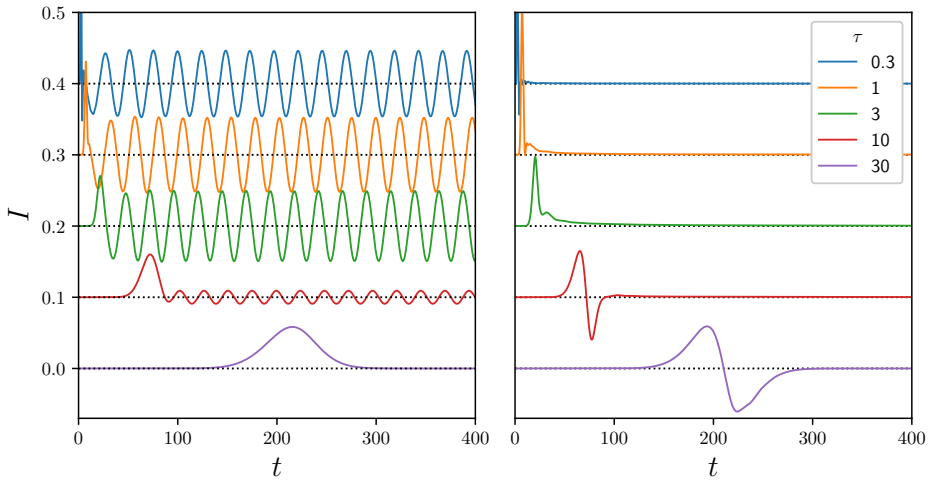

Figure 5.8: Simulation of pulses sent in an isolated Josephson junction. In the left panel, the pulses have a cumulative phase of π and different lengths. The curves are vertically offset for greater clarity. In the right panel, the pulse has a total phase of 2π. The time-dependent periodic current is present for short pulses.

The results of the time-dependent simulation are presented in Fig 5.8. The junction is initially in the state $\varphi = 0$. In the left panel, the pulse has a total phase $\int V(t)dt = \pi$. Each curve corresponds to a different pulse duration τ. A long pulse ($\tau \gg \hbar/\Delta$) is a quasi-adiabatic process and preserves the initial occupation of the system. The current after a long pulse is stationary and given by the initial state current related to $I(\psi) = 0$ (bottom curves of left panel of figure Fig 5.2). A short pulse ($\tau \ll \hbar/\Delta$) contains many harmonics and excites all modes of the system, the current becomes sinusoidal depending on time (top curves of left panel of figure Fig 5.2). The current only depends on the final occupancy of the modes, so a similar result is expected for all short pulses, regardless of their duration.

In the left panel, the pulses have a total phase of $\int V(t)dt = 2\pi$. In this state, Andreev's bound states are located just at the edge of the gap Fig 5.2, they can escape

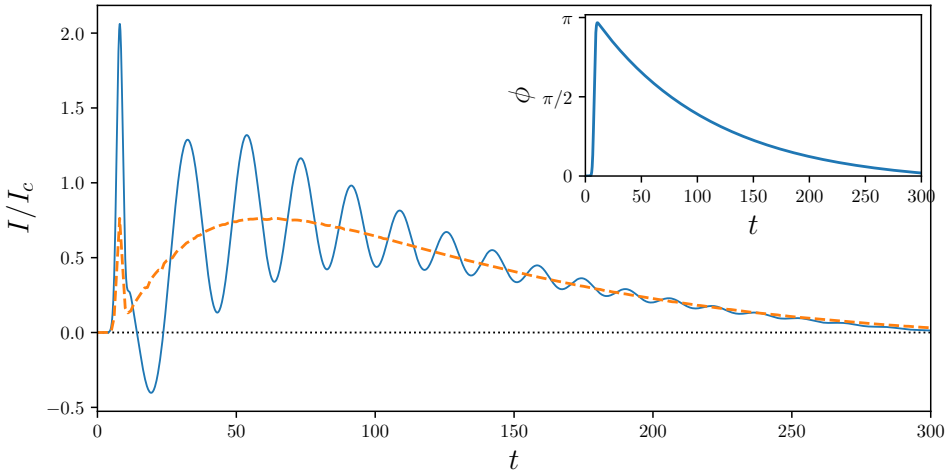

Figure 5.9: Response to a pulse from a Josephson junction in an RC circuit. For a junction with $2\pi/\Delta = 31$ and $D = 0.5$ we chose $R = 0.01$ and $RC = 100$. The blue curve corresponds to the quantum simulation. The dotted line corresponds to a conventional circuit with an effective sinusoidal junction. The zoom shows the phase as a function of time.

to the continuum. After the pulse, no current is visible because no energy can be stored in the gap.

5.3.7 Short pulse excitation in RC environment

The junction is placed inside an RC circuit (see Fig 5.4). A pulse is sent into the circuit to induce a phase difference at the junction terminal of π. An RC circuit admits a single stable equilibrium state at $\varphi = 0$. In this stable state oscillations are not present. To observe oscillations we need to be out of equilibrium $\varphi \neq 0$. To observe proper oscillations we require that the phase moves slowly towards its equilibrium state with respect to the oscillation period $\tau_0 =\sim 2\pi/\Delta$. The decay time of the phase is given by the characteristic time RC, which imposes the value of the capacity $RC \gg \tau$. To reduce the voltage variation due to feedback from the junction current, we need a low resistance of $RI_c \ll 1$.

The result of a simulation is displayed in Fig. 5.9. The dotted curve indicates the expected current for a purely sinusoidal junction. The simulated current oscillates around the reference current. The time of decrease of the oscillation is given by the time $RC = 100$. The oscillation period changes over time, but the order of magnitude is $\sim 0.7\tau_0$, the difference may be explained because the decay time is not negligible

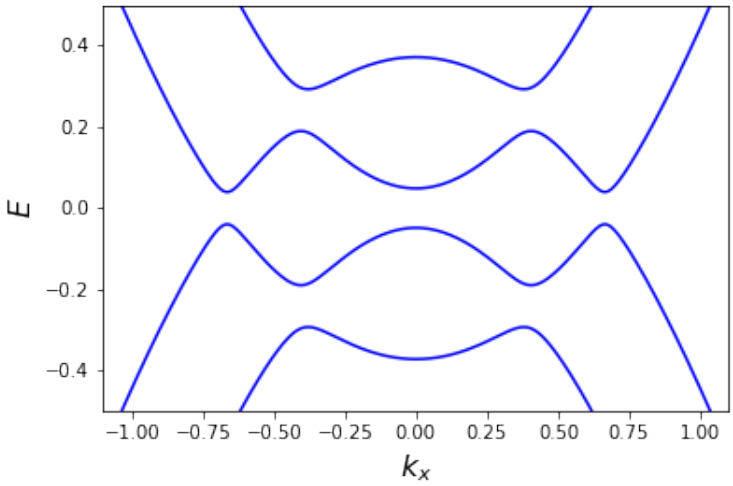

Figure 5.10: Energy-moment dispersion for a superconductor $\Delta = 0.06$ with Rashba spin-orbit coupling $\alpha = 0.15$ and under magnetic field $E_Z = 0.21$. The junction is placed in topological regime $E_Z^2 > E_F^2 + \Delta^2$ with $E_F = 0.15$.

compared to the oscillation time $RC \sim 3\tau$.

5.4 Topological junction

There are multiple recent works on the topological junction [96; 97; 98]. The Andreev's bound states of these junctions has two interesting properties. First of all, the bound state is delocalized in space, the wave function is present in the central region of the junction but also at the boundary of the two superconductors. This protects the Andreev statee from local disruptions, they can make interesting candidates for a qubit. Secondly, bound states have Majorana fermion properties, the switching relationship of creation/annihilation operators is different from that of the boson or Dirac fermions. This interesting property allows Majorana to weave Majorana [99]. So far, Majorana's detection has been difficult. We will concentrate on the detection of the 4π-periodic current-phase relation of as a proof as the presence of Majorana states.

5.4.1 Topological superconductor

A topological superconductor is obtained by adding a spin-orbit coupling and a magnetic field into a superconductor. In practice, superconductors repel all magnetic fields. Topological superconductors are experimentally constructed with a spin-orbit coupled

material placed in a magnetic field and connected to superconductors. The proximity of the superconductors induces a gap inside the non-superconducting material.

The Hamiltonian describing a topological superconductor [100] is obtained from a normal superconductor Eq. 5.2 and adding spin-orbit coupling and a magnetic field. Rashba's spin-orbit coupling is modeled by a first-order derivative in space

$$\hat{H}_{\text{Rashba}} = -i\alpha\hbar \left(\hat{c}_\uparrow(\mathbf{r})^\dagger \vec{\nabla} \hat{c}_\uparrow(\mathbf{r}) - \hat{c}_\downarrow(\mathbf{r})^\dagger \vec{\nabla} \hat{c}_\downarrow(\mathbf{r}) \right). \tag{5.26}$$

The magnetic field is modeled by the Zeeman energy E_z,

$$\hat{H}_{\vec{B}} = E_z \left(\hat{c}_\uparrow(\mathbf{r})^\dagger \hat{c}_\uparrow(\mathbf{r}) - \hat{c}_\downarrow(\mathbf{r})^\dagger \hat{c}_\downarrow(\mathbf{r}) \right). \tag{5.27}$$

We use the same Bogoliugov transformation as for the normal superconductor. Then we move to the tight-binding model to obtain the total Hamiltonian

$$\hat{H} = \frac{1}{2} \sum_{ij} \hat{\mathbf{c}}_i^\dagger \begin{pmatrix} \mathrm{h}_{ij} & \Delta_{ij} & E_z\delta_{ij} & -i\alpha_{ij} \\ \Delta_{ij}^* & -\mathrm{h}_{ij} & -i\alpha_{ij} & -E_z\delta_{ij} \\ E_z\delta_{ij} & -i\alpha_{ij} & \mathrm{h}_{ij} & \Delta_{ij} \\ -i\alpha_{ij} & -E_z\delta_{ij} & \Delta_{ij}^* & -\mathrm{h}_{ij} \end{pmatrix} \hat{\mathbf{c}}_j, \tag{5.28}$$

where $\mathrm{h}_{ij} = D_{ij} - E_F\delta_{ij} + U_{ij}$ and $\alpha_{ij} = \alpha(\delta_{i,j-1} + \delta_{i,j-1})$. The four components are connected, there are no longer two separate sectors as in the case of a normal superconductor. Without gap, magnetic field and Rashba spin-orbit coupling, bands of the system are similar to a normal metal consisting of four bands, two degenerate bands corresponding to the electron with spin up and down, and two other degenerate bands corresponding to the holes of each spin. The effect of the magnetic field is to eliminate degeneracy by splitting in energy the opposite spin bands. The effect of the Rashba spin-orbit is to shift the electron and hole bands in momentum. Finally, the superconducting parameters Δ open a gap around the Fermi energy. Figure 5.10 shows a bands of a topological superconductor.

5.4.2 Majorana bound states

A topological junction consists of two topological superconductors separated by a non-topological material. Once again, Andreev's states are trapped inside the gap. When $E_Z^2 > E_F^2 + \Delta^2$ the bound states become Majorana fermions [101].

The spectrum is actually 2π-periodic (see Fig. 5.11), but if we follow adiabatically a branch, we need a 4π phase to recover the same point, the spectrum is said to be 4π-periodic. This leads to a current phase relationship $i = \partial E/\partial\psi$ also 4π-periodic. We are interested in probing this property. The wave function of the bound state is

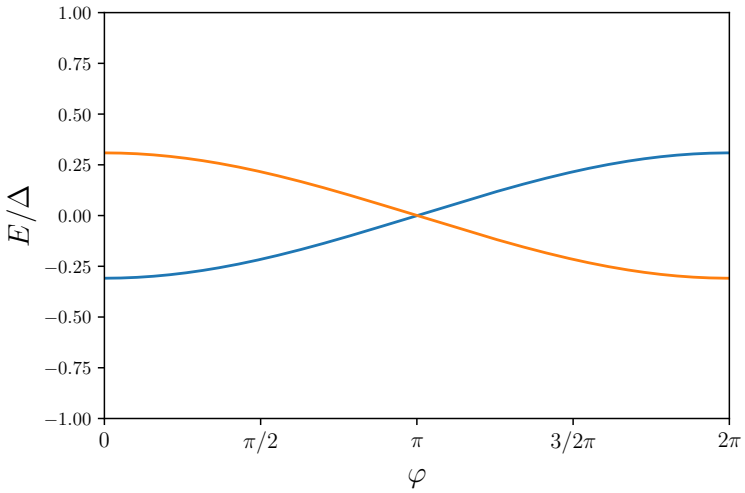

Figure 5.11: Energy-phase relation for the bound states of a topological junction of transparency $D = 0.5$. The relation is 4π periodic in the adiabatic regime.

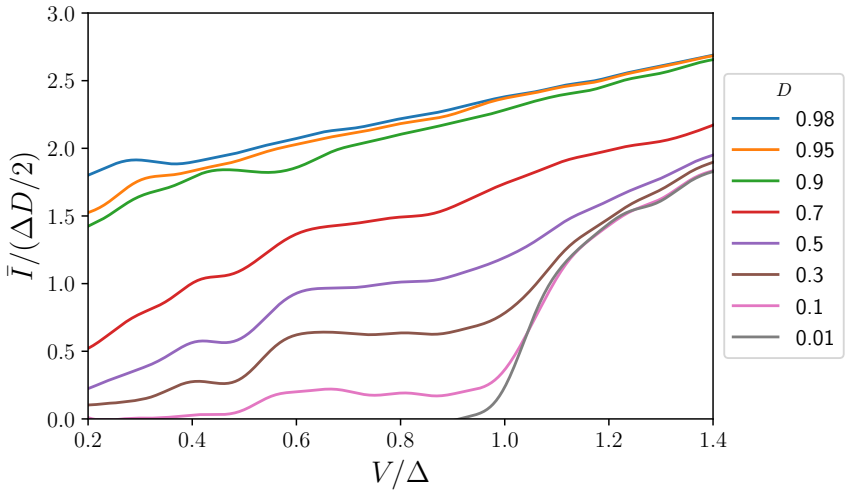

Figure 5.12: Average current of the topological junctions with different transparencies D. For each transparency, a voltage ramp is applied to a junction. The current is obtained by moving average.

delocalized at the boundaries of the two topological superconductors, but we considered the semi-infinite superconducting lead, so the delocalization is pushed to infinity, only the central part of the wave function remains in our model.

We use our time-dependent transport algorithm to simulate a topological junction. Just like a normal junction, at high voltage $eV > 2\Delta$ there is a direct current linked to quasiparticles tunneling, see figure 5.12. At voltage $eV = 2\Delta/n,\ n \in \mathbb{Z}$ the opening of the MAR channel with n reflections are visible.

We remember that phase evolves with the voltage $\hbar\partial_t\varphi = eV$. At the equilibrium state, only one bound state is occupied. In the quasi adiabatic regime $eV \ll \Delta$ the occupation follows the same energy-phase branch and we obtain the 4π-periodic current phase relation $I = I_c \sin(eVt/\hbar)$, see Fig. 5.11. But at $\varphi = \pi$ the two branches cross. There's a chance for bound state to tunnel from one branch to the other. After many cycles, the occupations of the two branches reach a balance where the two branches are equally occupied. The two branches have an opposite contribution to the current, in the equilibrium state the contributions of the two occupations cancel each other out, the current of the junction is only given by the current of the quasiparticles, which is 2π periodic. Fig 5.13 shows a topological junction under low voltage. First, the current-voltage relation follows the stationary relationship corresponding to a single occupied bound state. After a number of cycles, the relationship became periodic and close to the stationary contribution of quasiparticles. The lifetime of the 4π-periodicity has been studied in [102], it depends on the voltage amplitude and the transparency of the junction. We leave the comparison between their theory and life time in our simulations for future work.

5.4.3 Majorana junction inside an RLC resonator

The junction is placed inside an RLC circuit similar to that of the section used 5.3. The circuit enters in resonance when the ac Josephson frequency of the junction corresponds to the frequency of the resonator ω_0. For a normal junction it happens at $eV = \omega_0$, for a 4π-periodic junction it happens at $eV = 2\omega_0$.

The results of two simulations are presented in Fig 5.14. In the left panel, the resonator frequency is tuned to the same order of magnitude as the gap of the junction $\omega = \Delta$. The junction has a high transparency $D = 0.5$. In this regime, the 4π-periodicity disappears quickly, cf Ref. [102]. The resonance appears at $eV = \omega$. In the right panel, the transparency of the junction is small $D = 0.044$, and the resonator frequency is set to be well below Δ. In this regime, the 4π-periodicity survives long enough to be probed, the resonance appears at $eV = 2\omega_0$.

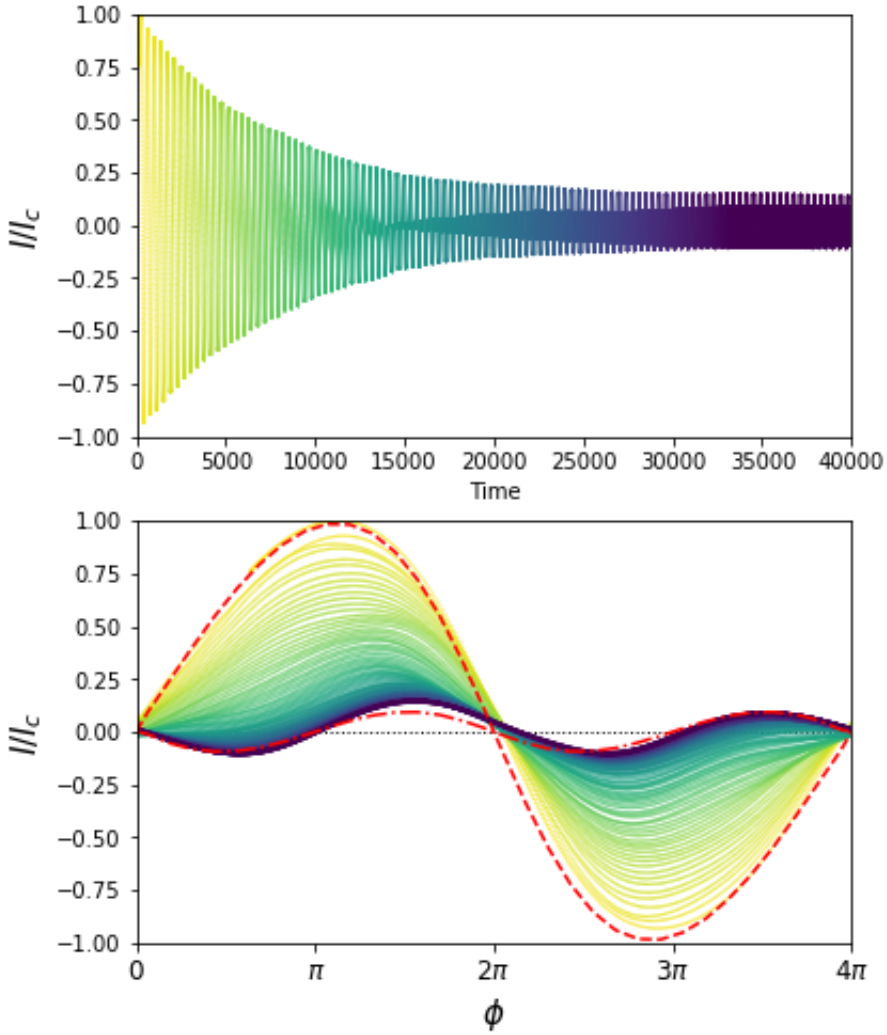

Figure 5.13: Simulation of an isolated topological junction under voltage bias. The upper panel shows the current as a function of time. In the lower panel, the current-phase relationship extracted from the simulation. The dashed line corresponds to the stationary direct current, 4π-periodic. The dot-dash line corresponds to the stationary current with the contribution of the bound states removed, 2π-periodic. The color indicates the progress in time with the same progression in both panels.

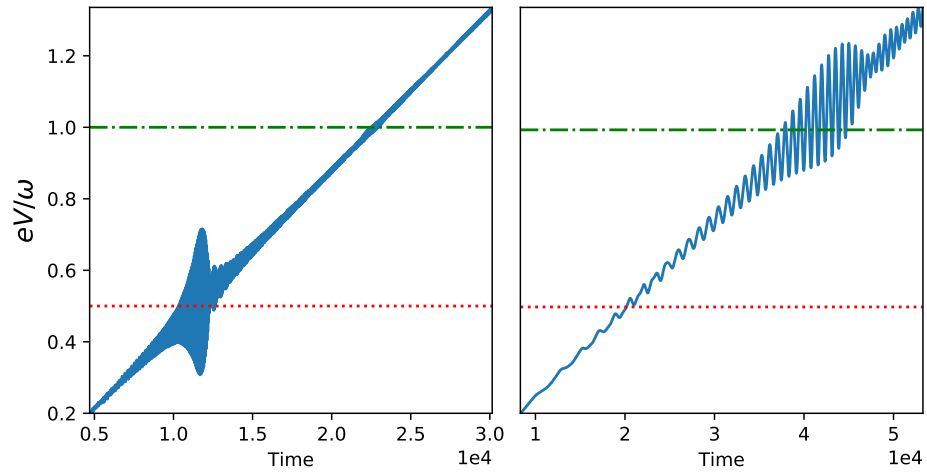

Figure 5.14: Voltage as a function of the time of a topological junction in a RLC circuit. In the left panel a junction with transparency $D = 0.5$, the resonator frequency is equal to $\omega_0 = 3\Delta$. In the right panel, a junction with transparency $D = 0.044$ and a resonator frequency $\omega = 0.2\Delta$. The dotted line is located at $2eV = \omega_0$ corresponding to the resonances of a periodic junction of 2π. The dotted line is located at $eV = \omega$ corresponding to a 4π-periodic junction.

5.4.4 Conclusion

The models presented in this chapter combine the environment with a BdG models that include the quasiparticle spectrum of the junctions as well as its dynamics out-of-equilibrium. We have shown that the interplay between the two physics strongly modifies the behavior of the system and lead to new phenomena such as the voltage induced non-sinusoidal current phase relations and oscillating current in the absence of bias voltage. Our approach provides a practical route to study the engineering of electromagnetic environments in the presence of junctions that go beyond simple tunneling devices. Besides the example studied in this letter (a single channel junction with arbitrary transparency), other systems such as Josephson FETs [103], multiterminal devices [104] that are being developed by the community could be studied with the same technique [105].

Chapter 6

On the simulation of decoherence

So far in this thesis, the observables considered have been limited to the expectation value of the operator at a given time $\langle O(t) \rangle$. The output variables of the circuit are processed in a classic way. This allows for many applications as we have seen in the previous chapters, however, a wide range of experiments requires taking into account the quantum nature of the observables. Coulomb's blockage is a major phenomenon that requires quantum processing of the output. In general, all shot noise measurements also require considering quantum fluctuations beyond the average value of the operators.

In the first part of this chapter, we consider the quantum fluctuations of operators, also called quantum noise. Quantum noise can be related to the quantum correlation of electrons notably thanks to the work of Blanter and Büttiker [106], it carries useful information not contained in the average values. Quantum noise can be calculated in the formalism of the wave function as done in Ref. [107].

The method of the first part allows to calculate the statistical properties of quantum noise, the probability distribution of the observed values. However, it is not able to produce a realization of this noise, i.e. a series of fluctuating observable values that correspond to a possible output of the system. This comes from the impossibility of the method to apply a non-unitary transformation induced by a projective measurement. In the second part of this chapter, we explore different ways to add the projective measure, i.e. the decoherence, to a time-dependent simulation.

6.1 Simulating shot noise

6.1.1 Definition of shot noise

The noise is related to the different possible results of a measure. In the context of time-dependent quantum transport, we are interested in the temporal fluctuations of the operators. The properties of quantum fluctifications of an operator $\mathcal{O}$ are contained in the two-times correlator called S. It is defined as follows

$$S(t,t') = \langle \hat{O}(t)\hat{O}(t')\rangle - \langle \hat{O}(t)\rangle \langle \hat{O}(t')\rangle . \tag{6.1}$$

Time-dependent quantities are difficult to measure experimentally, a better approach is to move to the frequency domain. Using a Fourier double transform, the frequency noise is given by

$$S(\omega,\nu) = \iint dtdt' \; e^{-i\omega t} e^{-i\nu t'} S(t,t'). \tag{6.2}$$

When the noise is invariant by time translation, only quantities dependent on $t-t'$ are relevant. This is captured by frequency noise or diagonal noise $S(t-t')$. Its Fourier transform is sometimes called noise power

$$S(\omega) = \iint dtdt' \; e^{-i\omega(t-t')} S(t-t'). \tag{6.3}$$

It is linked to two-frequency noise by the relationship $S(\omega) = S(\omega,-\omega)$.

6.1.2 Model for current noise

In the following, we focus on the noise of the current operator. In the context of a tight-binding model the current operator is defined by

$$\hat{I}_\mu(t) = \sum_{ij\in\mu} a_{ij}\hat{c}_i^\dagger(t)\hat{c}_j(t), \tag{6.4}$$

where the matrix a is defined by the Hamiltonian of the system as $a_{ij} = H_{ij} - H_{ji}$. The μ index run over all hoppings between sites in the diffusion region and sites of a lead. We define the correlator between the current operators of two leads μ,ν

$$S_{\mu\nu}(t,t') = \langle \hat{I}_\mu(t)\hat{I}_\nu(t')\rangle - \langle \hat{I}_\mu(t)\rangle \langle \hat{I}_\nu(t')\rangle . \tag{6.5}$$

Using Wick's theorem, we obtain the following equation, $\forall i,j$

$$S_{ij}(t,t') = \sum_{ijkl} a_{ij}a_{kl}G^<_{il}(t,t')G^>_{jk}(t,t'). \tag{6.6}$$

This formula is developed using the wave function formalism of chapter 3. The two-time correlator is expressed in terms of wave functions

$$S_{\mu\nu}(t,t') = \sum_{\alpha\beta} \iint \frac{dE}{2\pi}\frac{dE'}{2\pi} f_\alpha(E)(1-f_\beta(E'))I_{\mu,\alpha E,\beta E'}(t)I^*_{\nu,\alpha E,\beta E'}(t'), \tag{6.7}$$

where the current-correlator is define as

$$I_{\mu,\alpha E,\beta E'}(t) = \sum_{ij\in\mu} \psi^*_{\beta E'}(i,t)H_{ij}(t)\psi_{\alpha E}(j,t) - \psi^*_{\beta E'}(j,t)H_{ji}(t)\psi_{\alpha E}(i,t). \tag{6.8}$$

The index α and β indicate the lead modes. Bound states are neglected to simplify the equation Eq 6.7 but they can be easily added. The main difference with the computation of the lesser Green's function comes from the double integral mixing wave functions at different energies. The contribution of each wave function depends on the values of all other wave functions, this broke the parallelization of the calculation of the result. This makes noise calculation more demanding than averaging.

6.1.3 The stationary case

In the absence of time-dependent perturbations, wave functions are eigenvalues of the Hamiltonian, they obey to

$$\psi_{\alpha E}(t) = \psi_{\alpha E}(0)e^{iEt}. \tag{6.9}$$

This simplifies the correlation of the current into

$$I_{\mu,\alpha E,\beta E'}(t) = I_{\mu,\alpha E,\beta E'}(0)e^{i(E-E')t}. \tag{6.10}$$

Without time-dependent perturbation, the noise is invariant by translation over time. The two-times correlator only depends on the time difference $\tau = t - t'$

$$S_{\mu\nu}(\tau) = \sum_{\alpha,\beta} \iint \frac{dE}{2\pi}\frac{dE'}{2\pi} e^{i(E-E')\tau} f_\alpha(E)(1-f_\beta(E')) \left|I_{\mu,\alpha E,\beta E'}(0)I_{\nu,\alpha E,\beta E'}(0)\right|. \tag{6.11}$$

The frequency noise is obtained by the Fourier transform

$$S_{\mu\nu}(\omega) = \frac{1}{2\pi}\sum_{\alpha,\beta} \int \frac{dE}{2\pi} f_\alpha(E+\omega)(1-f_\beta(E)) \left|I_{\mu,\alpha E,\beta E'}(0)I_{\nu,\alpha E,\beta E'}(0)\right|. \tag{6.12}$$

In the limit of low temperature compared to Fermi energy $k_BT \ll E_F$ the Fermi factor $f_\alpha(E+\omega)(1-f_\beta(E))$ is only significant for energy between E_F and $E_F+\omega$ and is almost

zero everywhere else. For low frequencies $\omega \ll E_F$, only energies around E_f contribute to the noise. We have

$$I_{\nu,\alpha E,\beta(E+\omega)}(0) = \langle \psi_{\beta,(E+\omega)} | \hat{I}_\nu | \psi_{\alpha,E} \rangle = d_\alpha(E)\delta_{\alpha,\beta} + o(\omega), \tag{6.13}$$

where d_n is the transmission coefficient through the interface μ. To finally obtain the formula

$$S_{\mu\mu}(\omega) = \frac{1}{2\pi} \sum_\alpha \int \frac{dE}{2\pi} f_\alpha(E+\omega)(1 - f_\alpha(E)) D_\alpha(E), \tag{6.14}$$

where $D_\alpha = |d_\alpha|^2$ is the differential conductance of the mode α around the Fermi energy, it is a standard output of quantum transport software. Equation 6.14 gives a simple formula to compute numerically the noise, in stationary regime and in the limit $k_B T \ll E_F$ and $\omega \ll E_F$.

6.1.4 The time-dependent case

In the presence of a time-dependent perturbation, there is no simplification for Eq 6.7, calculating the double integral is the only way. Also the factor $f_\alpha(E)(1 - f_\beta(E'))$ is positive for energies $E < E < E_F^\alpha$ and for energies $E' > E_F^\beta$ so all energies from $-\infty$ to ∞ contribute to the noise. In this case, the key point is to achieve the double integral running through all energies. There is no technical difficulty, it is rather a calculation that requires a lot of resources.

As a proof of concept, we perform a simulation in the time-dependent case with noise calculation. We perform a simulation in the simple case of a tunnel barrier with transmission $D = 0.8$ under voltage bias. The voltage is branched to $t = 0$, the measurement of the noise is done after the system has reached a new equilibrium. The energy scale is set by the hopping term $1/2m^*a^2 = 1$. The noise calculation is performed by saving the value of the wave functions on the interface site $i, j \in \mu$. Integration is done once all wave functions have evolved. This method allows calculating for several values of the Fermi level and temperature with the simulation.

The results are presented in figure 6.1 for different temperatures. Within the limits of low frequencies and low temperatures, the simulation corresponds to the analytical prediction of Blanter and Büttiker [106] represented by dots in the right panel of Fig. 6.1. The simulation gives results for a wide range of frequency and temperature, shown in the left panel of Fig. The limits of the tight-binding model are visible at $\omega = \pm 4/2m^*a^2 = \pm 4$.

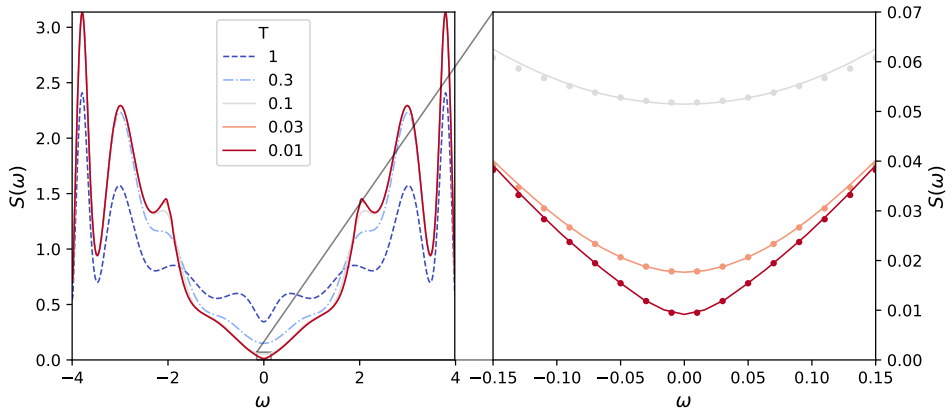

Figure 6.1: Normal tunnel barrier with transmission 0.8 under a voltage bias $V = 0.1$. The straight line is the time-dependent simulation with wave functions. The right panel is a zoom of the first low-frequency panel. The points are low-frequency analysis results from [108]

6.2 Simulating decoherence

So far, we've been able to measure the mean $\langle \hat{O} \rangle$ and the statistical properties $S(t, t')$ of a quantum system. However, these are weak measurements in the sense that the quantum system is not affected by the measurements. In particular, we are not able to simulate the collapse of the wave function necessary to produce a stochastic realization of the quantum noise, or to simply include the influence of a continuous measurement, the decoherence. To include these effects, we need to return to the formalism of the density matrix to derive the equations of motion of a system under a measurement.

6.2.1 Density matrix formalism

Let's consider a quantum system in the state represented by the vector $|\psi\rangle$ of Hilbert space $\mathcal{H}$ of this system. $\hat{O}$ is an observable, an endomorphism of $\mathcal{H}$. The expectation values are given by the product $\langle \psi | \hat{O} | \psi \rangle$. Using the property of the trace we have

$$\langle \psi | \hat{O} | \psi \rangle = \mathrm{tr}\Big(\langle \psi | \hat{O} | \psi \rangle \Big) = \mathrm{tr}\Big(\hat{O} \, |\psi\rangle\langle\psi| \Big). \tag{6.15}$$

The density matrix $\hat{\rho}_\psi = |\psi\rangle\langle\psi|$ is an object containing the same information that the wave function of the system. But now consider a quantum system in a statistical superposition of state, $|\psi_0\rangle$ with probability p_0, $|\psi_1\rangle$ with probability p_1, $|\psi_i\rangle$ with

probability p_i, etc. The expectation value of an observable is given by

$$\langle \hat{O} \rangle = \sum_i p_i \langle \psi_i | \hat{O} | \psi_i \rangle = \mathrm{tr}\left(\hat{O} \sum_i p_i \hat{\rho}_{\psi_i} \right). \tag{6.16}$$

The density matrix $\hat{\rho} = \sum_i p_i \hat{\rho}_{\psi_i}$ is a single object that contains both information on all wave functions and the statistical composition of the system. Density matrices were introduced a long time ago by John von Neumann, but they are still particularly useful for dealing with statistical fluctuations in decoherence.

The equation of motion derives from their definition

$$\partial_t \hat{\rho} = -\frac{i}{\hbar}[\hat{H}\hat{\rho} - \hat{\rho}\hat{H}] = -\frac{i}{\hbar}[\hat{H}, \hat{\rho}]. \tag{6.17}$$

In addition, they have properties of unitarity $\mathrm{tr}(\hat{\rho}) = 1$ and hermiticity $\hat{\rho}^\dagger = \hat{\rho}$.

6.2.2 Definition of decoherence

Measurement or decoherence are effects of the external environment (measuring instrument, coupled element) on the quantum system. We consider a large quantum system encompassing all the elements, we note S the sub-part of the system whose properties we want to measure (the quantum System) and by E all the rest (the Environment). The evolution of the complete system is given by the density matrix $\rho_{S\cup E}$ and the equation of motion

$$\frac{d}{dt}\hat{\rho}_{S\cup E} = -\frac{i}{\hbar}[\hat{H}_{S\cup E}, \hat{\rho}_{S\cup E}], \tag{6.18}$$

where $H_{S\cup E}$ is the Hamiltonian of the complete system.

We are only interested in the density matrix of sub-part ρ_S. If the evolutions of the two parts, S and E, are highly correlated to each other, then there is no simple solution for the evolution of a single sub-part. Here we assume that the environment is large enough so that its dynamic is not influenced by the state of the S part. Since the environment has no memory of the state of S, this is called the Markov approximation. Under this approximation, we can use the trace on the unwanted part $\hat{\rho}_S = \mathrm{tr}_E(\hat{\rho}_{S\cup E})$ to obtain the equation of motion for $\hat{\rho}_S$

$$\frac{\partial \hat{\rho}_S}{\partial t} = -\frac{i}{\hbar}[\hat{H}_S, \hat{\rho}_S] + \sum_\mu \left(\hat{L}_\mu \hat{\rho}_S \hat{L}_\mu^\dagger - \frac{1}{2}\{\hat{L}_\mu^\dagger \hat{L}_\mu, \hat{\rho}_S\} \right), \tag{6.19}$$

where is the Hamiltonian of the S part alone. $\hat{L}_\mu$ are Lindblad operators, they are defined by coupling elements of the Hamiltonian between the system and the environment. Its is also possible to use effective Lindblad operators without having to explicit

the coupling Hamiltonian. The details of the calculation can be found in Ref. [109]. The second term of the left side $\hat{K} = -1/2 \sum_\mu \hat{L}_\mu^\dagger \hat{L}_\mu$ can be seen as a non-Hermitian Hamiltonian. It is regrouped with the Hermitian part to form the effective non-Hermitian Hamiltonian $\hat{H}_{\text{eff}} = \hat{H}/\hbar + i\hat{K}$ and simplify the equation of motion into

$$\frac{\partial \hat{\rho}}{\partial t} = -i[\hat{H}_{\text{eff}}, \hat{\rho}] + \sum_\mu \hat{L}_\mu \hat{\rho} \hat{L}_\mu^\dagger. \tag{6.20}$$

6.2.3 From Lindblad to Monte-Carlo

For a system with N degrees of freedom, the density matrix has a size 4^N. It is far too big for numerical simulation once the system size is larger than ~ 30 degrees of freedom.

A first step of simplification is to go back a the level of wave function. The approach is proposed in Ref. [110]. Starting from a system defined by a unique wave function $|\psi\rangle$, a pure state, the density of the system is $\hat{\rho} = |\psi\rangle\langle\psi|$. Using the equation of motion 6.20 we have after a small step of time dt

$$\hat{\rho}(t + dt) = \hat{\rho}(t) + dt(-i[\hat{H}_{\text{eff}}, \hat{\rho}] + \sum_\mu \hat{L}_\mu \hat{\rho} \hat{L}_\mu^\dagger). \tag{6.21}$$

The new density matrix is no longer in a pure state but in a sum of pure states

$$\hat{\rho}(t + dt) = p_0 \, |\phi_0\rangle\langle\phi_0| + \sum_\mu p_\mu \, |\phi_\mu\rangle\langle\phi_\mu| \,, \tag{6.22}$$

where we introduce the wave functions

$$|\phi_0\rangle = \frac{(\mathbb{1} - idt\hat{H}_{\text{eff}}) \, |\psi\rangle}{\sqrt{\langle\psi|\mathbb{1} - idt\hat{H}_{\text{eff}}|\psi\rangle}}, \quad |\phi_\mu\rangle = \frac{\hat{L}_\mu \, |\psi\rangle}{\sqrt{\langle\psi|\hat{L}_\mu|\psi\rangle}}, \tag{6.23}$$

and the amplitudes

$$\begin{aligned} p_\mu &= dt\sqrt{\langle\psi|\hat{L}_\mu|\psi\rangle}, \\ p_0 &= \langle\psi|\mathbb{1} - idt\hat{H}_{\text{eff}}|\psi\rangle = 1 - \sum_\mu p_\mu. \end{aligned} \tag{6.24}$$

The essential point here is to note that the amplitudes are real positive values with a total sum of 1, they form a set of probabilities. Thus, we can use a simple stochastic algorithm to calculate the evolution of the density matrix. At each time step, we randomly select a wave function among $|\phi_0\rangle$, $|\phi_\mu\rangle$ according to the probability p_0,

p_μ to become the new pure state of the system. We call trajectory a realization of this algorithm, i.e. a series of randomly chosen wave functions. The density matrix is obtained by averaging over all trajectories $\hat{\rho}(t) = \sum_{\text{traj}} |\phi_{\text{traj}}(t)\rangle\langle\phi_{\text{traj}}(t)|$. The main advantage of this algorithm is that it only considers wave functions, reducing the size of the problem to 2^N. It is an improvement over 4^N but still too expensive for a numerical simulation.

We note that the probability of applying a Lindblad operator is proportional to the size of the time steps dt, when the time step tends towards zero the number of applied Lindblad operator remains finite for a trajectory of finite duration.

6.2.4 Expectation value of observables

A second simplification comes from the fact that we are generally only interested in the expectation values of the operators and not in the explicit knowledge of the complete density matrix. The expectation value of an operator $\hat{O}$ is given by the average of the expectation value on each trajectory

$$\langle\hat{O}(t)\rangle = \sum_{\text{traj}} \langle\phi_{\text{traj}}(t)|\hat{O}|\phi_{\text{traj}}(t)\rangle \,. \tag{6.25}$$

A trajectory is produced by a series of random processes described by Eq. 6.23. After n time steps, a trajectory takes the form

$$|\phi(t)\rangle = \frac{1}{N}\hat{S}_n \ldots \hat{S}_1\hat{S}_0 \,|\phi(0)\rangle \,, \tag{6.26}$$

where N is a normalization factor and each $\hat{S}_i$ is either a $\hat{L}_\mu$ or $1 - idtH_{\text{eff}}$. A series of Hamiltonian steps can be grouped together using the exponential notation

$$\hat{U}(t,t') = \prod(1 - idt\hat{H}_{\text{eff}}) = Te^{-i\int_t^{t'}\hat{H}_{\text{eff}}(u)du}, \tag{6.27}$$

with T the time ordering operator. We note t_i the time where the operator $\hat{L}_{\mu_i}$ is applied to obtain

$$|\phi(t)\rangle = \hat{U}(t,t_n)\hat{L}_{\mu_n}U(t_n,t_{n-1})\hat{L}_{\mu_{n-1}} \ldots \hat{L}_{\mu_1}\hat{U}(t_1,0) \,|\phi(0)\rangle \,. \tag{6.28}$$

Using this expression the expectation value of the observable $\langle\phi(t)|\hat{O}|\phi(t)\rangle$ is expressed by the average value of a product of operator. This sounds like an application of Wick's theorem, except in our case because of the non-Hermitian Hamiltonian we have to be more careful. To continue with Wick's theorem we need a quadratic effective

Hamiltonian. On the one hand the Hermitian part of the Hermitian Hamiltonian must be quadratic, this corresponds to a quadratic normal Hamiltonian of the system. On the other hand, the non-Hermitian $\hat{K}$ part must be quadratic, this imposes conditions on the operators of Lindblad possible. We identify four types of Lindblad operators that give a quadratic non-Hermitian part

$$\hat{L}_\mu = \begin{cases} \hat{a}_i^\dagger \hat{a}_i \\ \hat{a}_i \hat{a}_i^\dagger \\ \sum_i \hat{a}_i \\ \sum_i \hat{a}_i^\dagger \end{cases}, \tag{6.29}$$

where $a_i^\dagger$ and a_i are any operator verifying $\{a_i^\dagger, a_j\} = \delta_{ij}$. We note that the first two cases describe the same physics, indeed equation 6.20 is invariant under the swap between $\hat{L} = \hat{a}_i^\dagger \hat{a}_i$ and $\hat{L} = \hat{a}_i \hat{a}_i^\dagger$. This is interesting to note because both cases describe the same physics but have different non-Hermitian parts and therefore different trajectories.

6.2.5 Non-Hermitian Wick's theorem

In this section, we explain the calculation in cases where the observable and Lindblad operators can be written as a product of two operators $\hat{c}_i^\dagger \hat{c}_j$ where $\forall i, j \ \{\hat{c}_i^\dagger, \hat{c}_j\} = \delta_{i,j}$. First we explicit the commutation relation between $\hat{c}_j$ and the operators $\hat{U}(t, t')$ and $\hat{\rho}_0 = |\psi_0\rangle\langle\psi_0|$. We use the property $i\partial_t \hat{U} = \hat{H}_{\text{eff}} \hat{U}$ and the expression $\hat{H}_{\text{eff}} = \sum_{ij} h_{\text{eff}}(i,j) \hat{c}_i^\dagger \hat{c}_j$ to obtain

$$\begin{aligned} i\frac{d}{dt} \begin{pmatrix} \hat{U}^{-1}\hat{c}_0\hat{U} \\ \vdots \\ \hat{U}^{-1}\hat{c}_n\hat{U} \end{pmatrix} &= \begin{pmatrix} \hat{U}^{-1}(\hat{c}_0\hat{H}_{\text{eff}} - \hat{H}_{\text{eff}}\hat{c}_0)\hat{U} \\ \vdots \\ \hat{U}^{-1}(\hat{c}_n\hat{H}_{\text{eff}} - \hat{H}_{\text{eff}}\hat{c}_n)\hat{U} \end{pmatrix} = \begin{pmatrix} \hat{U}^{-1}\sum_j h_{\text{eff}}(0,j)\hat{c}_j\hat{U} \\ \vdots \\ \hat{U}^{-1}\sum_j h_{\text{eff}}(n,j)\hat{c}_j\hat{U} \end{pmatrix} \\ &= h_{\text{eff}} \begin{pmatrix} \hat{U}^{-1}\hat{c}_0\hat{U} \\ \vdots \\ \hat{U}^{-1}\hat{c}_n\hat{U} \end{pmatrix}. \end{aligned} \tag{6.30}$$

The integration of this differential equation gives the commutation relation

$$\begin{pmatrix} \hat{c}_0\hat{U} \\ \vdots \\ \hat{c}_n\hat{U} \end{pmatrix} = T e^{-i\int h_{\text{eff}}(t)dt} \begin{pmatrix} \hat{U}\hat{c}_0 \\ \vdots \\ \hat{U}\hat{c}_n \end{pmatrix}. \tag{6.31}$$

Each element $\hat{c}_i\hat{U}$ is expressed as a sum of elements $\hat{U}\hat{c}_j$. We have a similar expression for the commutation relation with $\hat{U}^\dagger$. Similarly for ρ_0 we suppose that the initial density matrix is at thermodynamic equilibrium $\hat{\rho}_0 = \exp(\beta(\Omega + \mu\hat{N} - \hat{H}_0))$ with $\beta = 1/kT$. We use $\partial_\beta\hat{\rho}_0 = (\Omega + \mu\hat{N} - \hat{H}_0)\hat{\rho}_0$ to obtain

$$\begin{pmatrix} \hat{c}_0\hat{\rho} \\ \vdots \\ \hat{c}_n\hat{\rho} \end{pmatrix} = e^{\beta(\Omega+\mu-h_0)} \begin{pmatrix} \hat{\rho}\hat{c}_0 \\ \vdots \\ \hat{\rho}\hat{c}_n \end{pmatrix}, \tag{6.32}$$

with $\hat{H}_0 = \sum_{ij} h_0(i,j)\hat{c}_i^\dagger\hat{c}_j$. With this commutation relations we can express the expectation value of two operators. For exampe with the case $\langle\phi_0|\hat{U}^\dagger\hat{c}_i^\dagger\hat{c}_j\hat{U}|\phi_0\rangle = \mathrm{tr}\Big(\hat{c}_i^\dagger\hat{c}_j\hat{U}\rho_0\hat{U}^\dagger\Big)$ we write

$$\begin{pmatrix} \mathrm{tr}\Big(\hat{c}_i^\dagger\hat{c}_0\hat{U}\rho_0\hat{U}^\dagger\Big) \\ \vdots \\ \mathrm{tr}\Big(\hat{c}_i^\dagger\hat{c}_n\hat{U}\rho_0\hat{U}^\dagger\Big) \end{pmatrix} = -upu_\dagger \begin{pmatrix} \mathrm{tr}\Big(\hat{c}_i^\dagger\hat{c}_0\hat{U}\rho_0\hat{U}^\dagger\Big) \\ \vdots \\ \mathrm{tr}\Big(\hat{c}_i^\dagger\hat{c}_n\hat{U}\rho_0\hat{U}^\dagger\Big) \end{pmatrix} + upu_\dagger \begin{pmatrix} \delta_{0i}\,\mathrm{tr}\Big(\hat{U}\rho_0\hat{U}^\dagger\Big) \\ \vdots \\ \delta_{ni}\,\mathrm{tr}\Big(\hat{U}\rho_0\hat{U}^\dagger\Big) \end{pmatrix}, \tag{6.33}$$

with the notation $u = T\exp(-i\int h dt)$, $u_\dagger = T\exp(i\int h^\dagger dt)$ and $p = \exp(\beta(\Omega+\mu-h_0))$. We remember that $\hat{H}_{\text{eff}}$ is non-Hermitian at thus $u^{-1} \neq u_\dagger \neq u^\dagger$. We obtain the expectation value as

$$\begin{pmatrix} \mathrm{tr}\Big(\hat{c}_i^\dagger\hat{c}_0\hat{U}\rho_0\hat{U}^\dagger\Big) \\ \vdots \\ \mathrm{tr}\Big(\hat{c}_i^\dagger\hat{c}_n\hat{U}\rho_0\hat{U}^\dagger\Big) \end{pmatrix} = (1+upu_\dagger)^{-1}upu_\dagger\,\mathrm{tr}\Big(\hat{U}\rho_0\hat{U}^\dagger\Big) \begin{pmatrix} \delta_{0i} \\ \vdots \\ \delta_{ni} \end{pmatrix}. \tag{6.34}$$

In the absence of the environment, the effective Hamiltonian is Hermitian and we have $u^\dagger = u_\dagger = u^{-1}$ so simplifications happen

$$(1+upu_\dagger)^{-1}upu_\dagger\,\mathrm{tr}\Big(\hat{U}\rho_0\hat{U}^\dagger\Big) = \frac{1}{1+e^{\beta(\Omega+\mu-h_0)}}, \tag{6.35}$$

we recover the a Fermi distribution. In the non-Hermitian case, there is no simplification possible and we have to compute the matrix $(1+upu_\dagger)^{-1}upu_\dagger$ explicitly[1].

With a similar demonstration, we get the non-Hermitian Wick's Theorem in the form of

$$\mathrm{tr}\Big(\hat{c}_{i_0}^\dagger\hat{c}_{j_0}\hat{U}_0\ldots\hat{c}_{i_m}^\dagger\hat{c}_{j_m}\hat{U}_m\hat{\rho}_0\hat{U}_{m+1}^\dagger\hat{c}_{i_{m+1}}^\dagger\hat{c}_{j_{m+1}}\ldots\hat{U}_n\Big) = \begin{vmatrix} \langle\hat{c}_{i_0}^\dagger,\hat{c}_{j_0}\rangle & \ldots & \langle\hat{c}_{i_0}^\dagger,\hat{c}_{j_n}\rangle \\ \vdots & \ddots & \vdots \\ \langle\hat{c}_{i_n}^\dagger,\hat{c}_{j_0}\rangle & \ldots & \langle\hat{c}_{i_n}^\dagger,\hat{c}_{j_n}\rangle \end{vmatrix}, \tag{6.36}$$

[1]Binomial inversion formula is usefull to avoid divergences when $T \to 0$.

where two-point correlators are defined by

$$\langle \hat{c}^\dagger_{i_k}, \hat{c}_{j_l} \rangle = \mathrm{tr}\Big(\hat{U}_0 \dots \hat{U}_i \hat{c}^\dagger_{i_k} \hat{U}_{i+1} \dots \hat{U}_m \hat{\rho}_0 \hat{U}^\dagger_{m+1} \dots \hat{U}_j \hat{c}_{j_l} \hat{U}_{j+1} \dots \hat{U}_n\Big), \tag{6.37}$$

and can be calculated with the switching relations to get an expression similar to Eq. 6.34. The non-Hermitian Wick's Theorem apply directly to compute the expectation value of an operator along a trajectory. The result is expressed in terms of the matrices

$$\begin{aligned} u(t,t') &= Te^{-i\int h_{\mathrm{eff}}(t)dt}, \\ u_\dagger(t,t') &= Te^{i\int h^\dagger_{\mathrm{eff}}(t)dt}, \\ p &= e^{\beta(\Omega+\mu-h_0)}. \end{aligned} \tag{6.38}$$

For a system with N degree of freedom this matrices have a size N^2, thus we gain an exponential speed up against the 2^N wave function method. This acceleration is made possible because we only calculate the expected value of the observables of interest and do not explicitly calculate the complete density matrix. All together, for an open system, the cost of the simulation is in the order of $\sim T^5$ with the time of the simulation. This is much more than the algorithm in chapter 3 so we can't simulate the same systems as in previous chapters with decoherence. Our best simulations have gone to as many as 500 sites.

6.3 Application to a toy model

To illustrate the algorithm, we use a simple three-level system. This model does not illustrate any particular physics. We have chosen this small system in order to be able to compare our algorithm with an exact resolution method based on the density matrix. We note $\hat{c}_i$ the creation operator on the degree of freedom i. The Hamiltonian is constructed by adding a kinetic part and a time-dependent perturbation on a site

$$\hat{H} = \sum_i 2\hat{c}^\dagger_i \hat{c}_i + \sum_{i>j} -e^{-it\delta_{i2}\delta_{j3}} \hat{c}^\dagger_i \hat{c}_j + h.c.. \tag{6.39}$$

We introduce an effective Lindblad operator

$$\hat{L}_0 = \gamma \hat{c}^\dagger_0 \hat{c}_0, \tag{6.40}$$

where the parameter γ tune the strength of the decoherence. The density matrix is represented by a $(2^3)^2 = 64$ parameters. We solve the Lindblad equation 6.19 numerically with Runge-Kutta methods. We measure the average number of particles at each

site as a function of time. The results for an exact integration are represented by the dotted line in figure 6.2. The algorithm of the previous section is used to calculate the average number of particle along multiple random trajectories. In figure 6.2 we have the average of the results on 1, 10, 100, and 4800 trajectories.

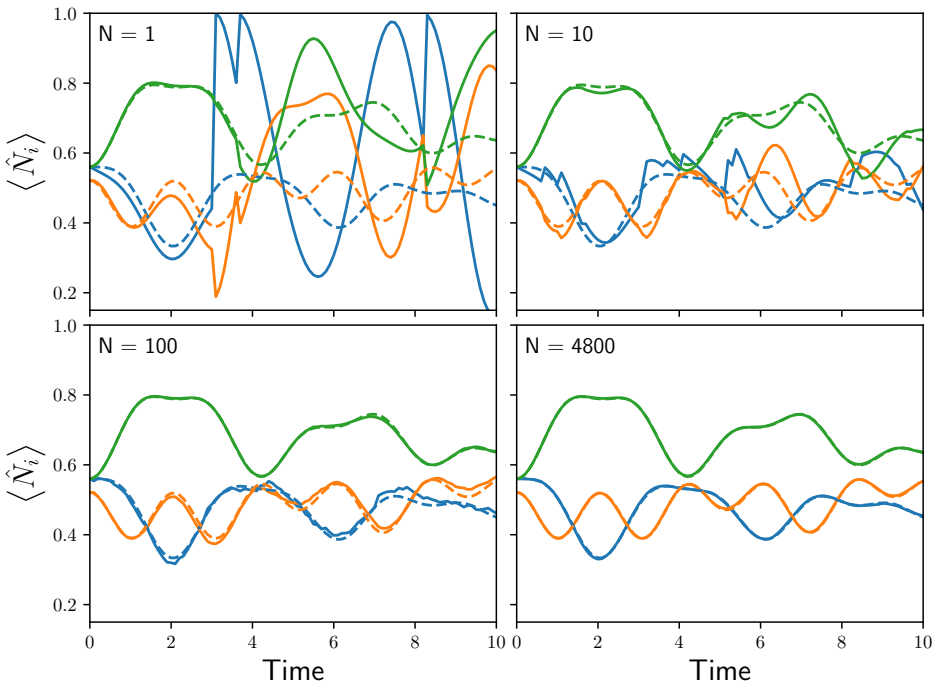

Figure 6.2: Density of the three sites at different times. The dotted lines are obtained by solving 6.19. The straight line is the sum of N trajectories. Each color corresponds to a site. Jumps in a trajectory produce discontinuities in the result. Our algorithm converges to the exact result for a large number of trajectories.

The average number of particles at each site shows multiple discontinuities. These are jumps caused by the application of a Lindblad operator $\hat{L}_0$ in the trajectory. The average over the trajectories converge to the exact result as the number of trajectories increases. As each trajectory is random, the convergence is of the order of $1/\sqrt{n}$ with n the number of trajectories.

6.4 Diagrammatic approachs

The model developed in the first section has similarities with the methods used to solve electron-electron interaction problems. A major technique to solve these interaction problems is the Feynman diagram decomposition. In this section, we study alternative method to develop the Lindblade equation with diagrams.

All the objects considered in this section are operators, so we drop the hat for simplicity. The evolution operator corresponding to the effective Hamiltonian operator is noted U with $\partial_t U(t,t') = -iH_{\text{eff}}\hat{U}(t,t')$. We introduce the density matrix in the interaction picture $\tilde{\rho}(t)^\dagger = \hat{U}^\dagger(t,0)\rho(t)U(t,0)$. The equation of motion for the density matrix is given by

$$\begin{aligned}\partial_t\tilde{\rho} =&(\partial_t U^\dagger)\rho U + U^\dagger\rho(\partial_t U) + U^\dagger(\partial_t\rho)U \\ =&iU^\dagger H_{\text{eff}}\rho U - iU^\dagger\rho H_{\text{eff}}U + U^\dagger\left(-i[\hat{H}_{\text{eff}},\hat{\rho}] + \sum_\mu \hat{L}_\mu\hat{\rho}\hat{L}_\mu^\dagger\right)U \\ =&\sum_\mu L_\mu(t)\tilde{\rho}(t)L_\mu^\dagger(t),\end{aligned} \tag{6.41}$$

where $L_\mu(t) = U^\dagger L_\mu U^{-1\dagger}$ are the jump operator in interaction picture. We introduce the linear quantum maps defined by $\mathcal{L}_\mu(t)(\rho) = L_\mu(t)\rho L_\mu^\dagger(t)$. The solution of the differential equation is given by

$$\tilde{\rho}(t) = T\exp\left(\int_0^t \sum_\mu \mathcal{L}_\mu(t')dt'\right)\rho_0 = T\sum_n \frac{1}{n!}\left(\int_0^t \sum_\mu \mathcal{L}_\mu(t')dt'\right)^n, \tag{6.42}$$

where T is the time-ordering operator. Indeed, the n-th term of the exponential series, noted G_n reads

$$TG_n(\rho_0) = T\int_0^t\cdots\int_0^t dt_1\ldots dt_n\left[\prod_{i=1}^n\sum_\mu L_\mu(t_i)\right]\rho_0\left[\prod_{i=n}^1\sum_\mu L_\mu^\dagger(t_i)\right], \tag{6.43}$$

where the time-ordering operator is used to order the operators $L_\mu(t_i)$ and $L_\mu(t_i)^\dagger$ by ascending time. By deriving with respect to time we obtain $\forall n \geq 1$,

$$\partial_t TG_n(\rho_0) = nT\sum_\mu L_\mu(t)G_{n-1}(\rho_0)L_\mu^\dagger(t) = \mathcal{L}_\mu(t)(TG_{n-1}(\rho_0)). \tag{6.44}$$

By summing all the terms of the exponential series, we obtain that the expression 6.42 is a solution of the differential equation 6.41 with the initial condition $\tilde{\rho}_0 = \rho_0$. Each order of the exponential serie corresponds to all trajectories with exactly n Lindblad

operators applied. The Monte-Carlo diagrammatic technique can be used to sample the n-dimensional integrals over time. This is a different way of summing all trajectories, however the non-Hermitian Wick's theorem is still needed to calculate the contribution of each trajectory. To get rid of the non-Hermitian Wick's theorem we move into the Hermitian interaction picture $\partial_t U = HU$ where H is the Hamiltonian of the system without environment. The result is identical to 6.42 except that there are two new types of operators in the quantum map

$$\mathcal{L}_\mu(t)(\rho) = L_\mu(t)\rho L_\mu^\dagger(t) - \frac{1}{2}L_\mu(t)L_\mu(t)^\dagger\rho - \frac{1}{2}\rho L_\mu(t)L_\mu(t)^\dagger. \tag{6.45}$$

The usual Wick's theorem is sufficient to calculate each trajectory. We note that with this same methodology, we can include non-quadratic interactions in the Hamiltonian, they will act as another type of operator in the quantum map. These diagrammatic methods have not been implemented in an algorithm but remain promising for future developments in decoherence simulation.

6.5 Conclusion

When measuring the output of a quantum system, the values of the observables vary around their mean value due to quantum statistics. The statistical properties of these variations can be calculated using the wave function formalism presented in chapter 3. However, this formalism cannot model the effects of the measurement on the wave function. We have two interesting ways to include the effect of the measurement on the wave function, or in other words to model the decoherence induced by the environment. The first method decomposes the problem into stochastic trajectories, where each trajectory is like a normal simulation with a finite number of quantum jumps. Averaging over several trajectories allows to recover the physics of the system. A prototype algorithm has been developed and tested to implement this method. However, the resulting algorithm is slow due to the non-Hermitian nature of the simulation and the intrinsic problems of Monte Carlo methods. The second method consists in decomposing the problem into pseudo Feynman diagrams. This method is close to the usual Monte Carlo methods, and the two can be combined for simulations taking into account both the interaction between electrons and decoherence. This is an ongoing work.

Chapter 7

Conclusion

The quest for the quantum computer has recently attracted much effort in the field of time-dependent quantum transport. The increasing complexity of experiments makes it necessary to use powerful numerical tools to analyze and understand experiments. The initial objective of this thesis was the inclusion of decoherence in quantum transport simulations. To reach this goal, three important steps have been taken: understanding the quantum transport, improving the quantum transport algorithms, and including environmental feedback at the classical level.

The first step was to understand the existing methods for numerically calculating time-dependent quantum transport. We studied purely analytical computation methods, Floquet theory and time-dependent simulations. We were able to compare the methods by applying them to the Mack-Zehnder interferometer problem. The combination of the different approaches allowed us to model and understand a realistic state-of-the-art interferometer model described by 2 million sites, including temperature effects. Thus we developed a concept experiment to characterize the interferometers in a robust way.

We have easily included the effects of electronic environments in the simulations by dynamically modifying the Hamiltonian of the system in functions of the observable measured on the classical system. However, the physics of the environment takes place on longer time scales and at higher levels of precision than the physics of isolated quantum systems. The second step of the thesis was to improve the numerical methods to adapt the quantum simulations to these new scales. The parallelism of the algorithms was improved to decrease the duration of the simulations and we used adaptive integration methods to increase the accuracy. In the same spirit as Kwant, we hope to quickly develop a freely accessible and easy-to-use version of this algorithm so that everyone can perform the simulations they need.

In the third step we have been able to study a wide variety of systems that have been inaccessible until now thanks to improvements in simulation algorithms and the inclusion of the environment. The Josephson junction model in an RC circuit and the Josephson junction model in an RLC environment have already been studied extensively, yet we have been able to highlight new and significant effects accessible to experiments coming from the contribution of quasiparticles. We have studied a model of pulse in Josephson junctions in order to propose a new concept of experiment where a junction produces a periodic train of pulses in the absence of current. We have studied topological junction models in an RLC resonator used to detect Majorana fermions, and we have characterized the intrinsic difficulties of this detection method.

Once all these steps were completed we were able to study the effects of decoherence. In a first step we used time-dependent simulations to calculate the statistical properties of the shot noise. In a second step we studied a more general model of decoherence in time-dependent systems based on the Lindblad equation. We demonstrated several methods to numerically solve this problem. One of them has been developed into a functional algorithm. However, the resulting simulations are still too slow. Nevertheless we hope to have opened interesting avenues for future research in the field of decoherence simulation.

Funding This work was supported by the ANR Full Quantum, the ANR QTERA, the French-Japon ANR QCONTROL and the US Office of Naval Research.

Chapter 8

Conclusion en français

La quête de l'ordinateur quantique a récemment attiré beaucoup d'efforts dans le domaine du transport quantique dépendant du temps. La complexité croissante des expériences rend nécessaire l'utilisation d'outils numériques puissants pour analyser et comprendre les expériences. L'objectif initial de cette thèse était l'inclusion de la décohérence dans les simulations de transport quantique. Pour atteindre cet objectif, trois étapes importantes ont été franchies : la compréhension du transport quantique, l'amélioration des algorithmes de transport quantique et l'inclusion d'une rétroaction de l'environnement au niveau classique.

La première étape a consisté à comprendre les méthodes existantes de calcul numérique du transport quantique en fonction du temps. Nous avons étudié les méthodes de calcul purement analytiques, la théorie de Floquet et les simulations en fonction du temps. Nous avons pu comparer les méthodes en les appliquant au problème de l'interféromètre de Mack-Zehnder. La combinaison des différentes approches nous a permis de modéliser et de comprendre un modèle d'interféromètre réaliste de pointe décrit par 2 millions de sites, incluant les effets de la température. Nous avons développé un concept expérimental pour caractériser les interféromètres de manière robuste.

Nous avons facilement inclus les effets des environnements électroniques dans les simulations en modifiant dynamiquement l'Hamiltonien du système en fonction d'observable mesuré sur le système classique. Cependant, la physique de l'environnement se déroule sur des échelles de temps plus longues et à des niveaux de précision plus élevés que la physique des systèmes quantiques isolés. La deuxième étape de la thèse consistait à améliorer les méthodes numériques pour adapter les simulations quantiques à ces nouvelles échelles. Le parallélisme des algorithmes a été amélioré pour diminuer la durée des simulations et nous avons utilisé des méthodes d'intégration adaptative pour augmenter la précision. Dans le même esprit que Kwant, nous espérons développer

rapidement une version librement accessible et facile à utiliser de cet algorithme afin que chacun puisse effectuer les simulations dont il a besoin.

Dans la troisième étape, nous avons pu étudier une grande variété de systèmes qui étaient jusqu'à présent inaccessibles grâce à l'amélioration des algorithmes de simulation et à l'inclusion de l'environnement. Le modèle de jonction Josephson dans un circuit RC et le modèle de jonction Josephson dans un environnement RLC ont déjà été largement étudiés, cependnat nous avons peu mettre en evidence des effets nouveaux et significatifs accessibles aux expériences provenant de la contribution des quasi-particules. Nous avons étudié un modèle de pulse dans les jonctions Josephson afin de proposer un nouveau concept d'expérience où une jonction produit un train périodique d'impulsions en l'absence de courant. Nous avons étudié des modèles de jonctions topologiques dans un résonateur RLC utilisé pour détecter les fermions de Majorana, et nous avons caractérisé les difficultés intrinsèques de cette méthode de détection.

Une fois toutes ces étapes terminées, nous avons pu étudier les effets de la décohérence. Dans une première étape, nous avons utilisé des simulations en fonction du temps pour calculer les propriétés statistiques du bruit de grenaille. Dans une deuxième étape, nous avons étudié un modèle plus général de décohérence dans les systèmes dépendant du temps, basé sur l'équation de Lindblad. Nous avons fait la démonstration de plusieurs méthodes pour résoudre numériquement ce problème. L'une d'entre elles a été développée en un algorithme fonctionnel. Cependant, les simulations qui en résultent sont encore trop lentes. Néanmoins nous espérons avoir ouvert des pistes intéressantes pour de futures recherches dans le domaine de la simulation de la décohérence.

Financement Ces travaux ont été financés par l'ANR Full Quantum, l'ANR QTERA, l'ANR QCONTROL France-Japon et le US Office of Naval Research.

Bibliography

[1] B. Gaury, J. Weston, M. Santin, M. Houzet, C. Groth, and X. Waintal, *"Numerical simulations of time-resolved quantum electronics,"* Phys. Rep **534**, 1 (2014).

[2] J. Weston, *Numerical Methods for Time-Resolved Quantum Nanoelectronics* (Springer International Publishing, 2017).

[3] L. Saminadayar, C. Bäuerle, and D. Mailly, *"Equilibrium properties of mesoscopic quantum conductors,"* arXiv preprint arXiv:0706.3369 (2007).

[4] T. Bautze, C. Süssmeier, S. Takada, C. Groth, T. Meunier, M. Yamamoto, S. Tarucha, X. Waintal, and C. Bäuerle, *"Theoretical, numerical, and experimental study of a flying qubit electronic interferometer,"* Phys. Rev. B **89**, 125432 (2014).

[5] D. Ferry and S. M. Goodnick, *Transport in nanostructures*, 6 (Cambridge university press, 1999).

[6] P. Tien and J. Gordon, *"Multiphoton process observed in the interaction of microwave fields with the tunneling between superconductor films,"* Physical Review **129**, 647 (1963).

[7] L. S. Levitov, H. Lee, and G. B. Lesovik, *"Electron counting statistics and coherent states of electric current,"* Journal of Mathematical Physics **37**, 4845 (1996).

[8] G. Fève, A. Mahé, J.-M. Berroir, T. Kontos, B. Plaçais, D. Glattli, A. Cavanna, B. Etienne, and Y. Jin, *"An on-demand coherent single-electron source,"* Science **316**, 1169 (2007).

[9] E. Bocquillon, F. Parmentier, C. Grenier, J.-M. Berroir, P. Degiovanni, D. Glattli, B. Plaçais, A. Cavanna, Y. Jin, and G. Fève, *"Electron quantum optics: partitioning electrons one by one,"* Physical Review Letters **108**, 196803 (2012).

[10] J. Dubois, T. Jullien, F. Portier, P. Roche, A. Cavanna, Y. Jin, W. Wegscheider, P. Roulleau, and D. Glattli, *"Minimal-excitation states for electron quantum optics using levitons,"* Nature **502**, 659 (2013).

[11] S. Hermelin, S. Takada, M. Yamamoto, S. Tarucha, A. D. Wieck, L. Saminadayar, C. Bäuerle, and T. Meunier, *"Electrons surfing on a sound wave as a platform for quantum optics with flying electrons,"* Nature **477**, 435 (2011).

[12] R. McNeil, M. Kataoka, C. Ford, C. Barnes, D. Anderson, G. Jones, I. Farrer, and D. Ritchie, *"On-demand single-electron transfer between distant quantum dots,"* Nature **477**, 439 (2011).

[13] I. for Quantum Computing, "https://angstromengineering.com," .

[14] B. D. Josephson, *"Possible new effects in superconductive tunnelling,"* Physics letters **1**, 251 (1962).

[15] R. Jaklevic, J. Lambe, A. Silver, and J. Mercereau, *"Quantum interference effects in josephson tunneling,"* Physical Review Letters **12**, 159 (1964).

[16] A. Steane, *"Quantum computing,"* Reports on Progress in Physics **61**, 117 (1998).

[17] V. E. Manucharyan, J. Koch, L. I. Glazman, and M. H. Devoret, *"Fluxonium: Single cooper-pair circuit free of charge offsets,"* Science **326**, 113 (2009).

[18] R. Barends, J. Kelly, A. Megrant, D. Sank, E. Jeffrey, Y. Chen, Y. Yin, B. Chiaro, J. Mutus, C. Neill, *et al.*, *"Coherent josephson qubit suitable for scalable quantum integrated circuits,"* Physical review letters **111**, 080502 (2013).

[19] M. Metcalfe, E. Boaknin, V. Manucharyan, R. Vijay, I. Siddiqi, C. Rigetti, L. Frunzio, R. Schoelkopf, and M. Devoret, *"Measuring the decoherence of a quantronium qubit with the cavity bifurcation amplifier,"* Physical Review B **76**, 174516 (2007).

[20] J. Koch, T. M. Yu, J. Gambetta, A. A. Houck, D. I. Schuster, J. Majer, A. Blais, M. H. Devoret, S. M. Girvin, and R. J. Schoelkopf, *"Charge-insensitive qubit design derived from the cooper pair box,"* Physical Review A **76**, 042319 (2007).

[21] J. M. Gambetta, J. M. Chow, and M. Steffen, *"Building logical qubits in a superconducting quantum computing system,"* npj Quantum Information **3**, 1 (2017).

[22] F. Arute, K. Arya, R. Babbush, D. Bacon, J. C. Bardin, R. Barends, R. Biswas, S. Boixo, F. G. Brandao, D. A. Buell, *et al.*, *"Quantum supremacy using a programmable superconducting processor,"* Nature **574**, 505 (2019).

[23] D. A. Ryndyk *et al.*, *"Theory of quantum transport at nanoscale,"* Springer Series in Solid-State Sciences **184** (2016).

[24] C. W. Groth, M. Wimmer, A. R. Akhmerov, and X. Waintal, *"Kwant: a software package for quantum transport,"* New J. Phys. **16**, 063065 (2014).

[25] J. Weston and X. Waintal, *"Linear-scaling source-sink algorithm for simulating time-resolved quantum transport and superconductivity,"* Physical Review B **93**, 134506 (2016).

[26] P. Armagnat, A. Lacerda, B. Rossignol, C. Groth, and X. Waintal, *"The self-consistent quantum-electrostatic problem in strongly non-linear regime,"* arXiv preprint arXiv:1905.01271 (2019).

[27] J. Rammer, *Quantum field theory of non-equilibrium states* (Cambridge University Press, Cambridge New York, 2007).

[28] C. Caroli, R. Combescot, P. Nozieres, and D. Saint-James, *"Direct calculation of the tunneling current,"* Journal of Physics C: Solid State Physics **4**, 916 (1971).

[29] Y. Meir and N. S. Wingreen, *"Landauer formula for the current through an interacting electron region,"* Physical Review Letters **68**, 2512 (1992).

[30] J. Rammer and H. Smith, *"Quantum field-theoretical methods in transport theory of metals,"* Reviews of modern physics **58**, 323 (1986).

[31] M. Wimmer, *Quantum transport in nanostructures: From computational concepts to spintronics in graphene and magnetic tunnel junctions*, Ph.D. thesis (2009).

[32] C. Groth and al., "https://kwant-project.org," .

[33] M. Istas, C. Groth, A. Akhmerov, M. Wimmer, and X. Waintal, *"A general algorithm for computing bound states in infinite tight-binding systems,"* SciPost Physics **4**, 026 (2018).

[34] E. Hairer, S. Norsett, and G. Wanner, *Solving Ordinary, Differential Equations I, Nonstiff problems/E. Hairer, SP Norsett, G. Wanner*, Tech. Rep. (2Ed. Springer-Verlag, 2000, 2000).

[35] P. Gonnet, *Adaptive quadrature re-revisited* (ETH, Zürich, 2009).

[36] B. Rossignol and C. Groth, "Vectorized parallel numeric integrator and interpolator (code)," (2019).

[37] T. Kloss, J. Weston, and X. Waintal, *"Transient and sharvin resistances of luttinger liquids,"* Physical Review B **97**, 165134 (2018).

[38] D. Loss and D. P. DiVincenzo, *"Quantum computation with quantum dots,"* Phys. Rev. A **57**, 120 (1998).

[39] Zavoisky, J Phys USSR **9**, 211, 245 (1945).

[40] E. Knill, R. Laflamme, and G. J. Milburn, *"A scheme for efficient quantum computation with linear optics,"* Nature **409**, 46 (2001).

[41] D. Maxein and J. Laurat, *"Trapped ion to flying qubit,"* Nat. Photonics **7**, 169 (2013).

[42] C. Bäuerle, D. C. Glattli, T. Meunier, F. Portier, P. Roche, P. Roulleau, S. Takada, and X. Waintal, *"Coherent control of single electrons: a review of current progress,"* Rep. Prog. Phys **81**, 056503 (2018).

[43] G. Haack, M. Moskalets, J. Splettstoesser, and M. Büttiker, *"Coherence of single-electron sources from Mach-Zehnder interferometry,"* Phys. Rev. B **84**, 081303 (2011).

[44] G. Fève, P. Degiovanni, and T. Jolicoeur, *"Quantum detection of electronic flying qubits in the integer quantum Hall regime,"* Phys. Rev. B **77**, 035308 (2008).

[45] Y. Ji, Y. Chung, D. Sprinzak, M. Heiblum, D. Mahalu, and H. Shtrikman, *"An electronic Mach–Zehnder interferometer,"* Nature **422**, 415 (2003).

[46] P. Roulleau, F. Portier, P. Roche, A. Cavanna, G. Faini, U. Gennser, and D. Mailly, *"Direct Measurement of the Coherence Length of Edge States in the Integer Quantum Hall Regime,"* Phys. Rev. Lett. **100** (2008).

[47] M. Yamamoto, S. Takada, C. Bäuerle, K. Watanabe, A. D. Wieck, and S. Tarucha, *"Electrical control of a solid-state flying qubit,"* Nat. Nanotechnol. **7**, 247 (2012).

[48] D. S. Wei, T. van der Sar, J. D. Sanchez-Yamagishi, K. Watanabe, T. Taniguchi, P. Jarillo-Herrero, B. I. Halperin, and A. Yacoby, *"Mach-Zehnder interferometry using spin- and valley-polarized quantum Hall edge states in graphene,"* Sci. Adv. **3**, e1700600 (2017).

[49] J. Dubois, T. Jullien, F. Portier, P. Roche, A. Cavanna, Y. Jin, W. Wegscheider, P. Roulleau, and D. C. Glattli, *"Minimal-excitation states for electron quantum optics using levitons,"* Nature **502**, 659 (2013).

[50] E. Bocquillon, V. Freulon, J.-M. Berroir, P. Degiovanni, B. Plaçais, A. Cavanna, Y. Jin, and G. Fève, *"Coherence and Indistinguishability of Single Electrons Emitted by Independent Sources,"* Science **339**, 1054 (2013).

[51] R. P. G. McNeil, M. Kataoka, C. J. B. Ford, C. H. W. Barnes, D. Anderson, G. A. C. Jones, I. Farrer, and D. A. Ritchie, *"On-demand single-electron transfer between distant quantum dots,"* Nature **477**, 439 (2011).

[52] G. Fève, A. Mahé, J.-M. Berroir, T. Kontos, B. Plaçais, D. C. Glattli, A. Cavanna, B. Etienne, and Y. Jin, *"An On-Demand Coherent Single-Electron Source,"* Science **316**, 1169 (2007).

[53] B. Gaury and X. Waintal, *"Dynamical control of interference using voltage pulses in the quantum regime,"* Nat. Commun. **5**, 3844 (2014).

[54] P. P. Hofer and C. Flindt, *"Mach-Zehnder interferometry with periodic voltage pulses,"* Phys. Rev. B **90**, 235416 (2014).

[55] B. Gaury, J. Weston, and X. Waintal, *"The a.c. Josephson effect without superconductivity,"* Nat. Commun. **6**, 6524 (2015).

[56] M. L. Polianski and P. W. Brouwer, *"Pumped current and voltage for an adiabatic quantum pump,"* Phys. Rev. B **64**, 075304 (2001).

[57] P. W. Brouwer, *"Rectification of displacement currents in an adiabatic electron pump,"* Phys. Rev. B **63**, 121303 (2001).

[58] M. G. Vavilov, L. DiCarlo, and C. M. Marcus, *"Photovoltaic and rectification currents in quantum dots,"* Phys. Rev. B **71**, 241309 (2005).

[59] L. Arrachea and M. Moskalets, *"Relation between scattering-matrix and Keldysh formalisms for quantum transport driven by time-periodic fields,"* Phys. Rev. B **74**, 245322 (2006).

[60] S. P. Giblin, M. Kataoka, J. D. Fletcher, P. See, T. J. B. M. Janssen, J. P. Griffiths, G. A. C. Jones, I. Farrer, and D. A. Ritchie, *"Rectification in mesoscopic alternating current-gated semiconductor devices,"* J. Appl. Phys **114**, 164505 (2013).

[61] M. Martínez-Mares, C. H. Lewenkopf, and E. R. Mucciolo, *"Statistical fluctuations of pumping and rectification currents in quantum dots,"* Phys. Rev. B **69**, 085301 (2004).

[62] S. Takada, C. Bäuerle, M. Yamamoto, K. Watanabe, S. Hermelin, T. Meunier, A. Alex, A. Weichselbaum, J. von Delft, A. Ludwig, A. D. Wieck, and S. Tarucha, *"Transmission Phase in the Kondo Regime Revealed in a Two-Path Interferometer,"* Phys. Rev. Lett. **113**, 126601 (2014).

[63] S. Takada, M. Yamamoto, C. Bäuerle, K. Watanabe, A. Ludwig, A. D. Wieck, and S. Tarucha, *"Measurement of the transmission phase of an electron in a quantum two-path interferometer,"* Appl. Phys. Lett **107**, 063101 (2015).

[64] J. Weston and X. Waintal, *"Towards realistic time-resolved simulations of quantum devices,"* J Comput Electron. **15**, 1148 (2016).

[65] M. V. Moskalets, *Scattering Matrix Approach to Non-Stationary Quantum Transport* (Imperial College Press, 2011).

[66] O. Shevtsov and X. Waintal, *"Numerical toolkit for electronic quantum transport at finite frequency,"* Phys. Rev. B **87**, 085304 (2013).

[67] G. Roussely, E. Arrighi, G. Georgiou, S. Takada, M. Schalk, M. Urdampilleta, A. Ludwig, A. D. Wieck, P. Armagnat, T. Kloss, X. Waintal, T. Meunier, and C. Bäuerle, *"Unveiling the bosonic nature of an ultrashort few-electron pulse,"* Nature Communications **9**, 2811 (2018).

[68] M. Büttiker, H. Thomas, and A. Prêtre, *"Mesoscopic capacitors,"* Phys. Lett. A **180**, 364 (1993).

[69] C. Bäuerle, Private Communication.

[70] A. Logg, K.-A. Mardal, G. N. Wells, *et al.*, *Automated Solution of Differential Equations by the Finite Element Method* (Springer, 2012).

[71] R. Barends, J. Kelly, A. Megrant, D. Sank, E. Jeffrey, Y. Chen, Y. Yin, B. Chiaro, J. Mutus, C. Neill, P. O'Malley, P. Roushan, J. Wenner, T. C. White, A. N. Cleland, and J. M. Martinis, *"Coherent josephson qubit suitable for scalable quantum integrated circuits,"* Physical Review Letters **111**, 080502 (2013).

[72] H. Paik, D. I. Schuster, L. S. Bishop, G. Kirchmair, G. Catelani, A. P. Sears, B. R. Johnson, M. J. Reagor, L. Frunzio, L. I. Glazman, S. M. Girvin, M. H. Devoret, and R. J. Schoelkopf, *"Observation of high coherence in josephson junction qubits measured in a three-dimensional circuit QED architecture,"* Physical Review Letters **107**, 240501 (2011).

[73] M. F. Goffman, R. Cron, A. L. Yeyati, P. Joyez, M. H. Devoret, D. Esteve, and C. Urbina, *"Supercurrent in atomic point contacts and andreev states,"* Physical Review Letters **85**, 170 (2000).

[74] V. Mourik, K. Zuo, S. M. Frolov, S. R. Plissard, E. P. A. M. Bakkers, and L. P. Kouwenhoven, *"Signatures of majorana fermions in hybrid superconductor-semiconductor nanowire devices,"* Science **336**, 1003 (2012).

[75] Y. A. Izyumov, Y. N. Proshin, and M. G. Khusainov, *"Competition between superconductivity and magnetism in ferromagnet-superconductor heterostructures,"* Uspekhi Fizicheskih Nauk **172**, 113 (2002).

[76] A. I. Buzdin, *"Proximity effects in superconductor-ferromagnet heterostructures,"* Reviews of Modern Physics **77**, 935 (2005).

[77] R.-P. Riwar, M. Houzet, J. S. Meyer, and Y. V. Nazarov, *"Multi-terminal josephson junctions as topological matter,"* Nature Communications **7**, 11167 (2016).

[78] A. A. Golubov, M. Y. Kupriyanov, and E. Il'ichev, *"The current-phase relation in josephson junctions,"* Reviews of Modern Physics **76**, 411 (2004).

[79] J. Bardeen, L. N. Cooper, and J. R. Schrieffer, *"Microscopic theory of superconductivity,"* Physical Review **106**, 162 (1957).

[80] P. G. de Gennes, *Superconductivity of Metals and Alloys* (1966).

[81] C. Beenakker, *"Universal limit of critical-current fluctuations in mesoscopic josephson junctions,"* Physical review letters **67**, 3836 (1991).

[82] D. Averin and A. Bardas, *"ac josephson effect in a single quantum channel,"* Physical Review Letters **75**, 1831 (1995).

[83] K. K. Likharev, *"Superconducting weak links,"* Reviews of Modern Physics **51**, 101 (1979).

[84] W. C. Stewart, *"Current-voltage characteristics of josephson junctions,"* Applied Physics Letters **12**, 277 (1968).

[85] E. Ben-Jacob, D. J. Bergman, B. J. Matkowsky, and Z. Schuss, *"Lifetime of oscillatory steady states,"* Physical Review A **26**, 2805 (1982).

[86] M. C. Cassidy, A. Bruno, S. Rubbert, M. Irfan, J. Kammhuber, R. N. Schouten, A. R. Akhmerov, and L. P. Kouwenhoven, *"Demonstration of an ac josephson junction laser,"* Science **355**, 939 (2017).

[87] Z.-L. Xiang, S. Ashhab, J. Q. You, and F. Nori, *"Hybrid quantum circuits: Superconducting circuits interacting with other quantum systems,"* Reviews of Modern Physics **85**, 623 (2013).

[88] M. H. Devoret, D. Esteve, H. Grabert, G.-L. Ingold, H. Pothier, and C. Urbina, *"Effect of the electromagnetic environment on the coulomb blockade in ultrasmall tunnel junctions,"* Physical Review Letters **64**, 1824 (1990).

[89] T. Klapwijk, G. Blonder, and M. Tinkham, *"Explanation of subharmonic energy gap structure in superconducting contacts,"* Physica B+C **109-110**, 1657 (1982).

[90] J. C. Cuevas, J. Heurich, A. Martín-Rodero, A. L. Yeyati, and G. Schön, *"Subharmonic shapiro steps and assisted tunneling in superconducting point contacts,"* Physical Review Letters **88**, 157001 (2002).

[91] B. Rossignol, K. Thomas, J. Weston, B. Gaury, C. Groth, and X. Waintal, "Role of the quasi-particles in an electric circuit with josephson junctions (code and data)," (2019).

[92] M. Westig, B. Kubala, O. Parlavecchio, Y. Mukharsky, C. Altimiras, P. Joyez, D. Vion, P. Roche, D. Esteve, M. Hofheinz, M. Trif, P. Simon, J. Ankerhold, and F. Portier, *"Emission of nonclassical radiation by inelastic cooper pair tunneling,"* Physical Review Letters **119**, 137001 (2017).

[93] R. Simmonds, K. Lang, D. Hite, S. Nam, D. Pappas, and J. Martinis, *"Decoherence in josephson phase qubits from junction resonators,"* Physical Review Letters **93**, 077003 (2004).

[94] M. Reagor, W. Pfaff, C. Axline, R. W. Heeres, N. Ofek, K. Sliwa, E. Holland, C. Wang, J. Blumoff, K. Chou, M. J. Hatridge, L. Frunzio, M. H. Devoret, L. Jiang, and R. J. Schoelkopf, *"Quantum memory with millisecond coherence in circuit QED,"* Physical Review B **94**, 014506 (2016).

[95] V. Zaretskey, B. Suri, S. Novikov, F. C. Wellstood, and B. S. Palmer, *"Spectroscopy of a cooper-pair box coupled to a two-level system via charge and critical current,"* Physical Review B **87**, 174522 (2013).

[96] A. Das, Y. Ronen, Y. Most, Y. Oreg, M. Heiblum, and H. Shtrikman, *"Zero-bias peaks and splitting in an al–inas nanowire topological superconductor as a signature of majorana fermions,"* Nature Physics **8**, 887 (2012).

[97] V. Mourik, K. Zuo, S. M. Frolov, S. Plissard, E. P. Bakkers, and L. P. Kouwenhoven, *"Signatures of majorana fermions in hybrid superconductor-semiconductor nanowire devices,"* Science **336**, 1003 (2012).

[98] S. D. Sarma, M. Freedman, and C. Nayak, *"Majorana zero modes and topological quantum computation,"* npj Quantum Information **1**, 15001 (2015).

[99] C. Nayak, S. H. Simon, A. Stern, M. Freedman, and S. D. Sarma, *"Non-abelian anyons and topological quantum computation,"* Reviews of Modern Physics **80**, 1083 (2008).

[100] J. Weston, B. Gaury, and X. Waintal, *"Manipulating andreev and majorana bound states with microwaves,"* Physical Review B **92**, 020513 (2015).

[101] A. Y. Kitaev, *"Unpaired majorana fermions in quantum wires,"* Physics-Uspekhi **44**, 131 (2001).

[102] D. M. Badiane, L. I. Glazman, M. Houzet, and J. S. Meyer, *"Ac josephson effect in topological josephson junctions,"* Comptes Rendus Physique **14**, 840 (2013).

[103] T. Akazaki, H. Takayanagi, J. Nitta, and T. Enoki, *"A josephson field effect transistor using an InAs-inserted-channel $In_{0.52}Al_{0.48}As/In_{0.53}Ga_{0.47}As$ inverted modulation-doped structure,"* Applied Physics Letters **68**, 418 (1996).

[104] A. N. McCaughan and K. K. Berggren, *"A superconducting-nanowire three-terminal electrothermal device,"* Nano Letters **14**, 5748 (2014).

[105] J. Weston, B. Gaury, and X. Waintal, *"Manipulating andreev and majorana bound states with microwaves,"* Physical Review B **92**, 020513 (2015).

[106] Y. M. Blanter and M. Büttiker, *"Shot noise in mesoscopic conductors,"* Physics reports **336**, 1 (2000).

[107] B. Gaury and X. Waintal, *"A computational approach to quantum noise in time-dependent nanoelectronic devices,"* Physica E: Low-dimensional Systems and Nanostructures **75**, 72 (2016).

[108] Y. Blanter and M. Büttiker, *"Shot noise in mesoscopic conductors,"* Physics Reports **336**, 1 (2000).

[109] S. Haroche and J.-M. Raimond, *Exploring the Quantum* (Oxford University Press, 2006).

[110] G. Benenti and G. Casati, *"Quantum chaos, decoherence and quantum computation,"* Rivista del Nuovo Cimento **30** (2007).

List of publications

- Pacome Armagnat, A. Lacerda-Santos, Benoit Rossignol, Christoph Groth, Xavier Waintal. "The self-consistent quantum-electrostatic problem in strongly non-linear regime." SciPost Phys. 7, 031 (2019)
- Benoît Rossignol, Thomas Kloss, and Xavier Waintal. "Role of Quasiparticles in an Electric Circuit with Josephson Junctions." Physical review letters 122.20 (2019): 207702.
- Benoît Rossignol, Thomas Kloss, Pacôme Armagnat, and Xavier Waintal. "Toward flying qubit spectroscopy." Physical Review B 98.20 (2018): 205302.